Fracture Healing and Regeneration in the Context of an Altered Collagenous Extracellular Matrix

by

Jeffrey Albert Meganck

A dissertation submitted in partial fulfillment
of the requirements for the degree of
Doctor of Philosophy
(Biomedical Engineering)
in The University of Michigan
2010

Doctoral Committee:

Professor Steven A. Goldstein, Chair
Professor David H. Kohn
Assistant Professor Michelle S. Caird
Assistant Professor Kenneth M. Kozloff
Research Investigator Andrea I. Alford

2010

DEDICATION

To my parents Ray and Noreen and

to my wife April, who supported me all along the way

ACKNOWLEDGEMENTS

While this dissertation only has my name on the cover, I certainly do not deserve all of the credit. This work represents a tremendous effort on the part of countless individuals. None of this would have been possible without them. Chapter 2, the first major experiment, has already been published.[Meganck et al., BONE 2009] I tremendously thank my co-authors for their help, two of whom are also on my dissertation committee. I specifically thank them and my other committee members for all of their support and feedback. Dr. Andrea Alford provided invaluable input and was always available for questions. Dr. Michelle Caird was a tremendously supportive, taught me about clinical approaches, continuously provided supporting and positive feedback, and was always available despite her demanding clinical schedule. Dr. Dave Kohn always asked insightful questions which helped frame perspectives and thoughts. Dr. Ken Kozloff taught me a tremendous amount over the years both in his time as a student and later as a faculty member. This interaction helped frame some of the experiments in this dissertation using both μCT and the Brtl/+ mouse model. And, of course, I owe a tremendous debt of gratitude to Dr. Steve Goldstein for all of the guidance, support, assistance and advice that he has given me in graduate

school. Without Steve's guidance, I may never have had even half of the opportunities to learn that I did.

There are also a tremendous number of collaborators who I need to thank. Dr. Kurt Hankenson initially gave me an opportunity to learn about fracture healing and has always been supportive and helpful. Dr. Doug Taylor and Dr. Raj Rajani also taught me about fracture healing, histology, and provided fantastic friendship. Dr. Joan Marini at the NIH provided the Brtl/+ mouse model and invaluable experimental feedback. Dr. Tom Uveges, formerly in Dr. Marini's group, was also tremendously helpful and some early interactions with him helped provide knowledge into phenotypic aspects of the Brtl/+ mouse. Dr. Jim Dennis at Case Western Reserve University, Dr. Charles Meyer and Dr. Peyton Bland gave me an opportunity to learn how μCT with image registration can be useful in tissue engineering studies. Dr. Glenda Pettway and Dr. Laurie McCauley gave me an opportunity to learn about PTH and tissue engineering early on, guiding some of my future work. Dr. Paul Picot, Dr. Tim Morgan and Mike Thornton taught me a tremendous amount about μCT, and the knowledge they passed on to me has been unbelievably insightful in designing and executing the experiments in this dissertation. Dr. Rachel Caspari has given me invaluable advice and guidance on life, science, as well as a fun opportunity to learn about Neandertals.

There are also a tremendous number of people in the lab who I need to thank. Dennis Kayner always helped with repairs when something was broken, and his electronics expertise was critical in building the torsion tester used for

these studies. Charles Roehm helped fabricate the parts for this torsion tester, the phantoms used to understand μCT artifacts, and the mouse internal fixators used in this dissertation. None of this work would have been possible without these crucial contributions from Charles (not to mention the gamey nourishment he provided which fueled many days in the lab). Ed Sihler provided tremendous IT support and fascinating conversations. Peggy Piech and Sharon Vaassen provided administrative support, kept me organized, and just generally made sure that my head was always screwed on. Dr. Josh Miller helped read radiographs, provided clinical insight, and always asked inquisitive and challenging questions. John Baker and Rochelle Taylor were incredibly helpful with the histological processing and staining. Jason Combs, Xixi Wang and Sharon Reske all helped with mouse colony management and injections. Kathy Sweet was patient as I learned sterile surgical techniques and was always there to ensure that surgeries went smoothly. Bonnie Nolan also provided tremendous help with surgeries, and was always there to keep me grounded when the stress levels started to rise. I also need to thank many past and current students including (but certainly not limited to!) Aaron Weaver, Connie Pagedas, Jaclynn Kreider, Sylva Krizan, Tom Vanasse, Joey Wallace, Nadder Sahar, Sharon Segvich, Jason Long, Neil Halonen, Ben Sinder, Mathieu Davis, Grant Goulet, Grant Reeves, Erik Waldorff, Mike Friedman, Danese Joiner, Ed Hoffler, and Mike Ominsky. If I've forgotten any others, please know that it's only my absentmindedness and not a lack of appreciation for the camaraderie.

There are a few who I need to single out for their tremendous contributions. Dana Begun provided unbelievable help with the fracture healing study, all while staying grounded and always providing a laugh. Aaron Swick made incredible contributions to the statistical analysis of the fracture healing experiments and, along with Lingling Zhang at CSCAR, helped figure out how to handle those ANCOVA analyses. Arjun Khullar helped build the torsion tester. John-David McElderry, Kate Dooley, Francis Esmonde-White, Karen Esmonde-White, Jacque Cole, and everyone else in Dr. Mike Morris's lab were tremendously helpful with the Raman microspectroscopy work. I was also lucky to work with Dr. Steve Broski and Dr. Amy Sewick when they were med students and their contributions helped along the way.

Last, I need to thank a number of friends and family. It simply isn't possible to thank everyone. Dr. Feng Li for encouraged me to go back to graduate school. My sister and brother-in-law, Colleen and Tim, and my mother-in-law Kathryne were always there when I needed motivation. I need to thank gramps for passing on his knowledge of random skills and generally teaching me the value of hard work and how to get through life. I miss you gramps. I also need to thank my parents, Ray and Noreen, for providing all of the opportunities I've had and for always being supportive of my decisions. Last, and most importantly, I need to thank my wife April. None of this work ever could have happened without the love, support, encouragement, laughter and companionship that she has provided. I love you babe.

TABLE OF CONTENTS

LIST OF FIGURES

LIST OF TABLES

CHAPTER 1: INTRODUCTION

This dissertation represents three distinct studies that provide insights into bone imaging, fracture healing, and graft healing. The first study represents an investigation into image artifacts that impact the ability to interpret and measure bone density. The next study builds on this knowledge in a translational study of bone fracture healing using a mouse model with a genetic bone disease and, furthermore, studies this healing process using antiresorptives. The last study investigates healing of structural bone allograft using grafts from this same mouse model. While these three studies appear disjoint on the surface, they were all done with the common goal of advancing our understanding of the influence of matrix properties on bone repair using quantitative imaging tools.

Bone healing is well understood, although there are many circumstances that need to be investigated and could impact clinical treatment. As one example, the genetic bone disease investigated in the second study of this dissertation is osteogenesis imperfecta (OI). This disease is normally attributed to mutations in type I collagen. The afflicted pediatric OI patients have a high incidence of bone fractures and, currently, many are treated with bisphosphonates to reduce this

risk. However, even patients taking bisphosphonates may still have fractures. As a result, the healing takes place in the context of both a genetic and pharmacological alteration in the matrix. Bisphosphonates bind to bone mineral and have a long resonance time, so it is unclear how to treat these patients. This decision making process is even more complex in light of the underlying collagenous abnormalities. Type I collagen is not upregulated in fracture healing until the bone forms several weeks after the fracture. Once this is upregulated, and bone forms, remodeling begins to occur quite quickly. It is critical to understand this OI healing process in general and, furthermore, how the healing process is affected by bisphosphonate treatments.

The third study presented in this dissertation also explores the affect of matrix properties on healing by using bone grafts from OI mice. Bone grafts are the most commonly used bone substitute, although bone autografts, the current "gold standard" therapy, are not ideal. As a result, there is a tremendous interest in developing biomaterials, cell based therapies, and tissue engineering solutions that can replace the need for these grafts. However, despite tremendous research efforts, there is a lack of fundamental design criteria for these substitutes. Many substitutes are based on biomimetic design principles that attempt to leverage the natural healing process that occurs in autografts. Studying bone allografts with collagenous alterations, such as OI mice, are ideal for this purpose and, when demineralized and implanted, can provide direct insight into this question.

The fracture healing study and bone allograft studies mentioned above represent the main body of orthopedic basic science in this dissertation. However, to fully understand bone structure and density, these experiments employ imaging techniques that also have fundamental physical limits. It is essential to understand these limits, and how to avoid them, to obtain accurate images and meaningfully study these healing processes. An experiment investigating this, in conjunction with the experiments outlined above, addressed the hypotheses and aims outlined below.

The goal of the first study is to understand how to use a micro-computed tomography (μCT) system for accurate mineral density measurements. The aims are to use beam filtration to understand when beam hardening artifacts occur as a function of bone density and thickness and, furthermore, to understand how these artifacts impact bone density measurements in different scan setups.

The second study, fracture healing in a mouse model of OI with bisphosphonate treatment, tests the hypotheses that a pharmacologically induced delay in the rate of resorption will delay the restoration of full biomechanical function and normal bone structure. Furthermore, the presence of a disorganized collagenous ECM in the fracture callus will impact biomechanical function.

The third study, bone allograft healing using demineralized and undemineralized OI grafts, tests the hypothesis that alterations in the collagenous ECM of a bone graft impact the restoration of biomechanical function and remodeling of that graft.

Biological Processes and Biomechanics of Bone Healing and Regeneration

Skeletal fracture healing is a significant clinical problem. Most fractures are still treated with closed reduction and non-rigid fixation and heal normally. There are, however, risk factors such as avascularity, instability, large fracture gaps or concomitant infections that lead to poor fracture healing.[1] In fractures which do heal, intramembranous and endochondral ossification occur. These same ossification processes occur during bone growth and development and, therefore, the healing process may recapitulate initial bone formation.[2] In fact, many of the molecular markers present during growth and development are also upregulated during healing. The specifics of temporal regulation are highly dependent on the phase of healing. For a long bone fracture with only moderate inherent stability, the process involves an inflammatory phase, a reparative phase and then a final remodeling phase.[3] The inflammatory phase consists of a hematoma formation, immune response and progenitor cell recruitment to the fracture. The reparative phase consists of revascularization and bone formation by both intramembranous and endochondral pathways,[4] preceding remodeling to restore the normal bone structure. Sites that are more mechanically stable and naturally in compression may predominantly heal with primary bone in an intramembranous pathway.[3]

Irrespective of differences in site specificity and pathway, the ultimate goal is a healed bone with normal biomechanical function. For a reduced fracture stabilized with nonrigid fixation, function will not be restored until there is a

bridged bony callus. In a mid-diaphyseal fracture, for instance, the initial soft tissue callus does not have any substantial mechanical integrity. The healing callus, even through the period of endochondral ossification, will have poor biomechanical function. Once the callus is bridged, the biomechanical properties will improve until the bone structure may not even fail within the healing tissue.[5] This implies that, late in healing, the callus may not be the weakest point of the structure.

When rigid fixation is used, there is mechanical stability in the regenerating bone during every healing phase. Therefore, the biomechanical properties of the structure depend on the fixation and the healing tissue. Load sharing between the fixator and bone can result in stress shielding, and prevent the transmission of biomechanical stresses and strains that are conducive to bone formation. Therefore, optimizing future fixation system designs and materials to provide a mechanical incentive for bone healing while simultaneously providing adequate structural stability have been studied.[6,7]

Imaging Modalities for Assessing Bone Structure and Density

Bone structure and function depend on the macroscopic and microscopic tissue architecture, as well as the tissue material properties. As a result, numerous imaging modalities are used in clinical and research settings to understand these hierarchical alterations. For calcified bone structure, magnetic resonance imaging (MRI) has been used to study bone structure and, more recently, water content.[8,9] These results are promising and may be utilized in

many future studies. However, the technical complexities of obtaining accurate MR images, the length of time for a particular study, and the high equipment cost are significant drawbacks. Furthermore, bone biomechanical properties are a function of structure and density, but MRI is not capable of measuring bone density. As a result, several investigators have used ultrasound based metrics to estimate bone mechanical properties.[10] These measurements are useful in assessing fracture risk but are not capable of assessing bone structure and density simultaneously. As a result, the primary imaging modalities used to study bone structure and density are X-ray based.

Several X-ray based methods have been used. These include single photon absorptimetry, dual photon absorptimetry, dual energy x-ray absorptimetry (DXA), peripheral quantitative computed tomography (pQCT) and micro-computed tomography (μCT).[8,11] DXA measurements have been an invaluable tool for screening in bone diseases such as osteoporosis and are probably still the most widely used clinical tool for BMD measurements. However DXA measurements may not be accurate enough for many needs due, in part, to the inherent two dimensional limitations of DXA that preclude assessment of tissue architecture.[11,12] Because of this limitation, quantitative CT is being utilized in clinical research settings for accurate bone structure and mineral density measurements. pQCT has the ability to separate trabecular bone from cortical bone, and has also been used to estimate mechanical strength.[13,14] pQCT has also been used in small animal pre-clinical studies.[15] However, μCT images have better resolution than pQCT and, as a result, μCT has become the

standard for accurate morphological and mineral density measurements in most research studies.[15]

Beam Hardening Artifacts in CT Imaging

The use of μCT images to assess bone density is not trivial because of the inherent artifacts related to the physics of the CT imaging process. These include partial volume artifacts, photon starvation, photon scatter, undersampling and beam hardening.[16] While all of these artifacts will impair the ability to accurately measure BMD, beam hardening is arguably the most problematic. Beam hardening is a physical phenomenon resulting from preferential attenuation of low energy photons in the X-ray spectrum. This preferential attenuation is dependent on the beam path length and the linear attenuation coefficient. The linear attenuation coefficient, in turn, is dependent on the absorption coefficient (roughly correlated with Z number) and physical density.[17] Changes in the path length or linear attenuation coefficient can potentially alter the spectrum of the x-ray beam, resulting in beam hardening artifacts that can show up as cupping, streaks, dark bands, or flare artifacts.[16,18,19]

Corrections for beam hardening artifacts can be applied during the image acquisition process, during image reconstruction or post-reconstruction as empirical corrections. Procedures that are applied during acquisition require dual energy imaging and can be utilized to remove cupping, streak and flare artifacts.[18,20,21] Although most dual energy approaches require two separate scans, it is possible to use to use characteristic x-rays of the source and/or

detector to get two separate monochromatic energies.[22] Reconstruction approaches can also be used to correct beam hardening artifacts in both dual-energy and single-energy imaging if the input spectrum is known.[23] Other correction approaches require a thresholding step to estimate the path lengths and use lookup tables based on known properties during implementation.[19,24] This approach has been extended into a dual-reconstruction approach where the initial reconstructed image is segmented. Using these segmented images, forward projections in a tilted parallel beam geometry are used to locate the beam hardening artifact and subtract it from the original reconstruction.[25] Statistical reconstruction approaches based on Poisson distributions have also been proposed for both monoenergetic and polyenergetic spectra, with and without the need for a preliminary image segmentation procedure.[26,27]

Perhaps the easiest, and most widely used, class of beam hardening corrections is empirical in nature. These can be applied before image reconstruction to estimate the line integral of a monochromatic spectrum by applying a function to the line integral of a polychromatic spectrum,[28] or applying a correction to the sinogram.[29] Empirical corrections can also be applied to the images after reconstruction using polynomial basis functions, linearization procedures, calibration curves or conversion tables.[30-34] These empirical approaches have been used to in laboratory desktop μCT systems with some success, but the polynomial corrections could not completely remove beam hardening artifacts for all cases.[35,36] Perhaps the simplest and most common method to address beam hardening artifacts is beam filtration. Crystal

monochromators and band-pass filters have been utilized to achieve monochromatic and quasi-monochromatic spectra, respectively, for this purpose.[37,38]

Osteogenesis Imperfecta

Osteogenesis Imperfecta (OI) is one of the most common heritable musculoskeletal diseases.[39] OI typically results from splice site mutations or point mutations that result in a substitution for glycine in the genes encoding type I collagen, and can result in changes in the quantity of collagen or structural abnormalities in the collagen trimer.[40,41] As a result, the study of OI has been very useful in understanding the links between collagen alterations and bone strength.[42] OI studies are normally performed within a particular clinical subset of patients due to the range of disease severities. This is usually assessed using the system developed by Sillence that mild (type I), moderate (type IV), severe (type III) or lethal (type II) cases.[39] This classification system has recently been expanded to include types V, VI, VII based on histological features.[41,43,44] Types VII and VIII have been attributed to autosomal recessive mutations in the *CRTAP* and *LEPRE1* genes, both of which play a role in posttranslational modifications within the endoplasmic reticulum.[45]

Now that several hundred patients have been identified and the genetic alterations in their type I collagen genes have been decoded, there has been tremendous interest in relating particular genetic mutations with the disease severity. It was initially hypothesized that the position of the mutation within the

gene would predict disease severity, but analyses investigating that possibility were not insightful. As a result, subsequent analyses studied the relationships in more detail and revealed that the most problematic mutations may affect the major ligand binding regions.[41] This finding certainly provides insight into the disease, although a mechanistic relationship between the mutation and the disease ramifications remains elusive.

Irrespective of the particular mutation, OI patients may have a short stature, variations in scleral hue and occasionally dentinogenesis imperfecta. However, the largest problem in OI patients is the high incidence of bone fractures during childhood and adolescence. Therefore, OI therapies have focused on reducing this fracture risk. Growth hormone and cell transplantation therapies have been proposed,[46,47] but bisphosphonates are the most common treatment. Bisphosphonate treatments may increase BMD and, in many cases, reduce the fracture rate.[48] Whether or not a patient is on bisphosphonates, fractures will still occur. The fractures generally heal normally. However, there are case reports of OI patients with hyperplastic callus formation,[49,50] although the etiology of these hyperplastic calluses remains elusive.

Animal Models of Osteogenesis Imperfecta

Some of the most insightful studies into the relationships between type I collagen and bone biomechanical function come from studies using OI animal models. OI has been reported in dogs, zebrafish, cattle, sheep, cats and tigers,

but most studies have utilized mouse models.[51] Mouse models exist for both the recessive and dominant forms of OI. One of the early recessive mice, termed fragilitas ossium (*fro/fro*), shows radiographic limb deformities and short size, a slight change in collagen fibril size in the tendon and a decrease in osteonectin and sialoprotein content.[52,53] Another mouse with a recessively inherited version of the *CRTAP* gene is smaller, has kyphosis, is osteopenic and has a decrease in bone volume; these features correlate well with the clinical findings for OI type VII.[54] While these models help, they are not ideal due to the rare nature of the recessive variations and the difference in mutation between these models and classical OI collagen mutations.

There are, however, several mouse models with genetic mutations in the *COL1A1* and *COL1A2* genes that are similar to classical OI. In one model with 41 missing exons from the middle of the *COL1A1* gene, mice were smaller with dental abnormalities and had spontaneous fractures. A more detailed characterization revealed smaller bones that had inferior structural biomechanical properties at failure and decreased calcium to phosphate ratio in the bone mineral.[55-58] However, there is no clear clinical correlate to this particular mutation. A more recent mouse model with direct translational implications is a knock-in mutation in *COL1A2* created to mimic OI in an Amish population. While the magnitude of the differences depends on the genetic background, decreases in size and alterations in collagen biochemistry are consistent with the patient presentation. A detailed analysis showed loss of trabecular bone, smaller cortical

bones, and decreased failure loads for cortical bone that are all consistent with OI.[59]

Another mouse with an alteration in *COL1A2* is the *oim/oim* mouse, and was the first mouse reported with spontaneous bone fractures. Genetic analysis of these mice revealed that the collagen I trimer only contained α1 chains instead of the normal collagen trimer with two α1 chains and one α2 chain.[60] This may be similar to a patient,[61] although a mutation resulting in a homotrimer is not common. *oim/oim* mice have bowed long bones with spontaneous fractures, are smaller, have thinner and disorganized cortical bone, less trabecular bone, reduced structural biomechanical properties, BMD decreases and altered mineral chemistry and crystallinity.[60,62-66] The heterozygous form of this mouse (*oim/+*) also displays OI,[62] although the phenotype is much milder. These *oim/+* mice are smaller late in growth and have areas of disorganized bone, a decreased energy to failure, an altered mineral crystallinity, and changes in mineral alignment.[62-66] In the only known fracture healing study in OI animals, fracture calluses in *oim/oim* mice treated with RANK-Fc had larger calluses with a higher radiographic intensity and increased work to failure after 6 weeks of healing in comparison to saline treated *oim/oim* mice. However, the callus morphology and radiographic intensity did not change with Rank-Fc treatment in their WT counterparts and the work to failure decreased after 6 weeks of healing.[67]

There are also two mouse models of OI which have genetic alterations in *COL1A1*. In the *Mov13* mouse, a Moloney murine leukemia virus was used to

create a mutation in the first intron of the collagen I gene, preventing full gene transcription.[68,69] Mice homozygous for this mutation (*Mov13/Mov13*) do not survive, while the heterozygous form of this mutation causes a mild to moderate form of OI.[69,70] Examination of the bones revealed a decreased load to failure, less collagen, disorganized collagen, a change in tissue porosity, and an increased susceptibility to damage accumulation.[70-73] These mice do not survive well as a result of the leukemia virus. Furthermore, it would be preferable to have a model which mimics the qualitative defects in OI patients.

To fit this need, the Brtl mouse was developed as a knock-in model to mimic the G349C amino acid substitution in one *COL1A1* allele of a particular clinical case.[74] Breeding schemes with these much could result in a lethal phenotype (termed the BrtlII mouse as a mimics type II OI) or result in a phenotype where mice survive (termed the BrtlIV mice as a model for type IV OI). BrtlIV mice, hereafter termed Brtl/+ mice, weigh less, have smaller, hypermineralized cortical bones with decreased structural biomechanical properties, and have an increase in the osteoclast surface per bone surface during growth and development.[75-77]

Animal Models of Bone Healing

Research is constantly ongoing to understand and improve skeletal healing. As a result, there is a need for models to study these healing processes. Bone grafts and substitutes are commonly used in current clinical practice for spinal fusion and, as a result, models of interbody fusion, interprocess fusion and

spontaneous fusion following intervertebral disc degeneration have been reported in nonhuman primates, dogs, rabbits, guinea pigs and rats.[78-81] These models are useful but don't always provide basic insight into the mechanisms of bone healing. As a result, drill hole defects have been used in the cortex of long bones and calvariae of rabbits and rodents.[82-86]

Several other model systems have been developed to investigate long bone fracture healing. These models have been implemented for a wide range of animal sizes including rodent, rabbit, cat, dog, sheep, goat, horse and nonhuman primates, and have been extensively reviewed elsewhere.[87-92] This breadth of model systems allows study of fixation utilizing intramedullary nails, internal fixation systems, and external fixation systems comparable to clinical treatment paradigms. Rodents are particularly attractive models because of their low cost, short gestation times and the availability of transgenic animals. Customized external fixator systems to apply controlled loads have been essential in elucidating mechanobiological influences on tissue differentiation in healing fractures.[93,94] Furthermore, largely due to the diversity of transgenic mice available, many rodent fracture healing studies have been useful to understand the molecular biology of these healing processes.[91]

Within rodent fracture healing, the most widely used model uses a guillotine type device and was originally reported for rat femoral fractures.[95] This model attempts to create a closed, transverse fracture by inserting an intramedullary pin into the marrow cavity and inducing an impact load in 3 point bending. The success of this system has led to its expansion into murine femurs,

rat tibias and mouse tibias.[96-98] This model successfully recapitulates closed fractures, although it is quite rare that they will not heal. However, fracture non-unions are relatively uncommon but extremely problematic and may represent the most important fractures to study. As a result, similar models have developed to study more challenging fracture healing scenarios. One of these models cauterizes the lateral periosteum (the medial periosteum is left intact), resulting in delayed healing.[99] Another recent adaptation mimics an open fracture with concomitant infection by injecting Staphylococcus aureus bacteria into a reduced fracture.[100]

These models all represent relevant healing paradigms, but still do not encompass all clinical treatment approaches. Clinical methods for fracture stabilization include intramedullary nails, internal fixation, locking plates, and external fixation. As a result, models for these mechanisms of fixation have also been developed. One group from the AO foundation has developed murine models of a locking plate, a locking nail, an intramedullary compression screw, a pin-clip device and a nail with locking pins and characterized the biomechanical stability in these models.[89,101] These models may be useful in the future, but are still not well suited to study bone graft healing. Fortunately, bone graft healing has been studied in a mouse femur using intramedullary fixation.[102] All of these model systems, taken together, provide a broad toolkit to understand bone healing biology and biomechanics for regenerative bone research.

Therapeutics and Methods to Enhance Bone Healing

Because bone fractures are a significant clinical problem, particularly in osteoporosis and other diseases of skeletal fragility, there has been a tremendous interest in developing therapeutics to prevent bone fractures. Several therapies have been tested including calcium, vitamin D, calcitonin, raloxifene, hormone replacement therapy, fluoride, a variety of bisphosphonates and, more recently, denosumab (a monoclonal antibody against RANKL) and odanacatib (a Cathepsin K inhibitor).[103-105] Alendronate, etidronate and denosumab may be effective in preventing vertebral and non-vertebral fractures.[103,104] However, there is still a need for therapeutics to enhance bone healing.

Noninvasive technologies utilizing electromagnetic and/or ultrasound stimulation have been proposed,[106] although these may not always provide therapeutic benefit.[107,108] As a result, pharmaceutical therapeutics have been investigated. Simvastatin was not promising for minimally displaced distal radius fractures.[109] Similarly, vitamin D supplementation may improve BMD during healing,[110] although it is unclear if this represents a faster rate of healing with improved function. PTH induces anabolic bone formation at low intermittent doses,[111] so the use of PTH has been investigated pre-clinically and increases both callus and bone volume earlier in healing.[112] Growth hormone treatments resulted in more consolidation and an improvement in structural biomechanical properties in a small animal model,[113] and an initial clinical study did not improve healing of open fractures but was efficacious for closed fractures.[114]

Open fractures are more problematic than closed fractures, so therapeutics are also needed to treat those situations. BMP2 and BMP7/OP-1 have shown some efficacy in spine fusion, fracture healing and may also improve graft healing both clinically and preclinically.[80,115-121]

Most of these therapeutics aim to be anabolic and facilitate early bone formation. However, normal biomechanical function is not restored until the remodeling phase of fracture healing and, therefore, antiresorptives like bisphosphonates have been investigated. In one clinical trial using bisphosphonates to prevent fracture risk, there was no reported adverse affect of healing in subsequent fractures.[122] Bisphosphonates have also been used in OI patients to reduce fracture risk with some efficacy,[48] although some patients still present with subsequent fractures. Therefore, studies on how bisphosphonates affect fracture healing in OI have been performed and indicate no noticeable effect on fracture healing in some patients although they may affect bone healing in an osteotomy.[123,124] Many animal studies have also attempted to elucidate the effects of bisphosphonate treatment on fracture healing.[125-133] These effects do not occur during the initial endochondral repair process,[134] and depend on the dosage and treatment timing. For example, treatment with a high dose of incadronate before and after fracture (in comparison to a low dose or high dose only before fracture) resulted in a trend towards more bone and a higher ultimate load in a rat model.[130,131] However, these increases did not correspond to any change in the stiffness of the fracture,[131] so it is unclear whether or not this treatment was beneficial. Other

data suggest that bisphosphonate treatment, either before the fracture, after the fracture, or both, did not significantly affect the structural biomechanical properties.[128,129,132] Some of these interactions may be caused by a delay in removal of cartilage within the callus.[133] Because of this, one study investigated how to optimize bisphosphonate treatment protocols and found that delaying the injection of a potent bisphosphonate until after the fracture resulted in a larger callus with higher peak loads and higher stiffness but no change in work to failure.[126]

Substitutes to Augment Healing of a Segmental Bone Defect

While many reduced and closed fractures heal naturally, bone substitutes are still needed for spinal fusion, cases of segmental bone loss, and other conditions where healing has been shown to be poor. Bone grafts, in conjunction with fixators and instruments to facilitate fixation, have been used to achieve this goal for decades. Autografts are commonly taken from the iliac crest and can be extremely viable, but require a second surgical site and may not provide enough bone for some needs. In some of these cases, free vascularized fibula grafts can be viable, [135] although this is technically demanding, costly, and still requires multiple procedures. As a result, bone allografts can be obtained from tissue banks or commercial vendors and have been extensively used. Proper sterilization and devitalization can minimize the risk of disease transmission with bone grafts.[136] However, vascular invasion is required to facilitate the graft resorption and remodeling processes that result in incorporation.[137] Even when

this revascularization does occur, allografts are susceptible to microdamage and may decrease in strength over time.[138] Recent research developments have indicated that revascularization and revitalization using factors such as RANKL to stimulate remodeling, or factors such as VEGF, COX2 and BMP2 like signaling molecules, can all improve revitalization and healing of structural undemineralized allografts.[139-143] In fact, BMP2 in conjunction with allograft bone chips has shown clinical efficacy as a bone substitute.[118]

Because of these limitations, there has been a tremendous interest in developing bone substitutes using biomaterials, cells, biological factors, and/or a combination of all of these. Bioceramics, bioglasses, synthetic polymers, natural polymers and composite materials have all been studied.[144-148] A variety of designs and structures have been examined to obtain scaffolds which are osteoinductive and have sufficient mechanical properties, porosity, degradation rates, and surface chemistries to support new bone formation. Despite the wealth of studies, the criteria that will result in successful scaffold design is still poorly understood and, as a result, many investigators have turned to biologically inspired designs.[149] These approaches attempt to mimic the structure of the organic and inorganic constituents of bone. One example of this approach combines powdered mineralized type I collagen fibrils with poly-lactic acid, and was successfully integrated into host bone when combined with rhBMP-2 and implanted into a rabbit radial defect.[150,151]

Scaffolds like these will be undoubtedly be used to restore mechanical function in the future. Efforts to maintain this mechanical function in the long term

may depend on the fixation and, in a more biological sense, assurance that remodeling of the new bone and scaffold does not result in a loss of properties.[152] Remodeling rates in synthetic scaffolds may differ from normal bone if the synthetic scaffolds do not naturally induce resorption. However, some materials utilize manufactured and/or demineralized bones to generate type I collagen substitutes.[153,154] Materials like this, as well as electrospun scaffolds which have the capability to alter cell function,[155] must be carefully studied to ensure that they maintain mechanical function during the late phase incorporation and remodeling. To this end, some investigators have begun investigating how to induce osteoclast formation on mineralized polymers.[156] Others studied biomaterial resorbability and found that osteoclasts could resorb calcium phosphate cement (for example) at a similar rate to dentine.[157] Although there is a clear need to understand how remodeling affects graft biomechanics, there is no consensus about how substitute ultrastructure contributes to remodeling and the restoration of biomechanical function.

References

1. Lynch, J.R., Taitsman, L.A., Barei, D.P., and Nork, S.E. 2008. Femoral nonunion: risk factors and treatment options. *J Am Acad Orthop Surg* 16:88-97.
2. Miclau, T., Schneider, R.A., Eames, B.F., and Helms, J.A. 2005. Common Molecular Mechanisms Regulating Fetal Bone Formation and Adult Fracture Repair. In *Bone regeneration and repair: biology and clinical applications*. J.R. Lieberman, and G.E. Friedlaender, editors. Totowa, NJ: Humana Press. 45-55.
3. Sfeir, C., Ho, L., Doll, B.A., Azari, K., and Hollinger, J.O. 2005. Fracture Repair. In *Bone regeneration and repair: biology and clinical applications*. J.R. Lieberman, and G.E. Friedlaender, editors. Totowa, NJ: Humana Press. 21-44.

4. Gerstenfeld, L.C., Cullinane, D.M., Barnes, G.L., Graves, D.T., and Einhorn, T.A. 2003. Fracture healing as a post-natal developmental process: molecular, spatial, and temporal aspects of its regulation. *J Cell Biochem* 88:873-884.
5. White, A.A., 3rd, Panjabi, M.M., and Southwick, W.O. 1977. The four biomechanical stages of fracture repair. *J Bone Joint Surg Am* 59:188-192.
6. Perren, S.M. 2002. Evolution of the internal fixation of long bone fractures. The scientific basis of biological internal fixation: choosing a new balance between stability and biology. *J Bone Joint Surg Br* 84:1093-1110.
7. Woo, S.L., Lothringer, K.S., Akeson, W.H., Coutts, R.D., Woo, Y.K., Simon, B.R., and Gomez, M.A. 1984. Less rigid internal fixation plates: historical perspectives and new concepts. *J Orthop Res* 1:431-449.
8. Jiang, Y., Zhao, J., and Genant, H. 2002. Macro- and Microimaging of Bone Architecture. In *Principles of Bone Biology, 2nd ed.* J.P. Bilezikian, L.G. Raisz, and G.A. Rodan, editors. San Diego: Academic Press. 1573-1585.
9. Techawiboonwong, A., Song, H.K., Leonard, M.B., and Wehrli, F.W. 2008. Cortical bone water: in vivo quantification with ultrashort echo-time MR imaging. *Radiology* 248:824-833.
10. Blake, G.M., and Fogelman, I. 2002. Methods and Clinical Issues in Bone Densitometry and Quantitative Ultrasonometry. In *Principles of Bone Biology, 2nd ed.* J.P. Bilezikian, L.G. Raisz, and G.A. Rodan, editors. San Diego: Academic Press. 1573-1585.
11. Genant, H.K., Faulkner, K.G., Gluer, C.C., and Engelke, K. 1993. Bone densitometry: current assessment. *Osteoporos Int* 3 Suppl 1:91-97.
12. Bolotin, H.H. 2007. DXA in vivo BMD methodology: An erroneous and misleading research and clinical gauge of bone mineral status, bone fragility, and bone remodelling. *Bone* 41:138-154.
13. Lochmuller, E.M., Lill, C.A., Kuhn, V., Schneider, E., and Eckstein, F. 2002. Radius bone strength in bending, compression, and falling and its correlation with clinical densitometry at multiple sites. *J Bone Miner Res* 17:1629-1638.
14. Martin, D.E., Severns, A.E., and Kabo, J.M. 2004. Determination of mechanical stiffness of bone by pQCT measurements: correlation with non-destructive mechanical four-point bending test data. *J Biomech* 37:1289-1293.
15. Schmidt, C., Priemel, M., Kohler, T., Weusten, A., Muller, R., Amling, M., and Eckstein, F. 2003. Precision and accuracy of peripheral quantitative computed tomography (pQCT) in the mouse skeleton compared with histology and microcomputed tomography (microCT). *J Bone Miner Res* 18:1486-1496.
16. Barrett, J.F., and Keat, N. 2004. Artifacts in CT: recognition and avoidance. *Radiographics* 24:1679-1691.
17. Webb, A.R. 2003. *Introduction to biomedical imaging*. Hoboken, New Jersey: Wiley. xiii, 252 p. pp.

18. Duerinckx, A.J., and Macovski, A. 1978. Polychromatic Streak Artifacts in Computed Tomography Images. *Journal of Computer Assisted Tomography* 2:481-487.
19. Joseph, P.M., and Spital, R.D. 1978. Method for Correcting Bone Induced Artifacts in Computed Tomography Scanners. *Journal of Computer Assisted Tomography* 2:100-108.
20. Alvarez, R.E., and Macovski, A. 1976. Energy-Selective Reconstructions in X-Ray Computerized Tomography. *Physics in Medicine and Biology* 21:733-744.
21. Remeysen, K., and Swennen, R. 2006. Beam hardening artifact reduction in microfocus computed tomography for improved quantitative coal characterization. *International Journal of Coal Geology* 67:101-111.
22. Van de Casteele, E., Van Dyck, D., Sijbers, J., and Raman, E. 2002. An energy-based beam hardening model in tomography. *Physics in Medicine and Biology* 47:4181-4190.
23. Yan, C.H., Whalen, R.T., Beaupre, G.S., Yen, S.Y., and Napel, S. 2000. Reconstruction algorithm for polychromatic CT imaging: Application to beam hardening correction. *Ieee Transactions on Medical Imaging* 19:1-11.
24. Kijewski, P.K., and Bjarngard, B.E. 1978. Correction for beam hardening in computed tomography. *Medical Physics* 5:209-214.
25. Hsieh, J., Molthen, R.C., Dawson, C.A., and Johnson, R.H. 2000. An iterative approach to the beam hardening correction in cone beam CT. *Medical Physics* 27:23-29.
26. Elbakri, I.A., and Fessler, J.A. 2002. Statistical image reconstruction for polyenergetic X-ray computed tomography. *Ieee Transactions on Medical Imaging* 21:89-99.
27. Elbakri, I.A., and Fessler, J.A. 2003. Segmentation-free statistical image reconstruction for polyenergetic x-ray computed tomography with experimental validation. *Physics in Medicine and Biology* 48:2453-2477.
28. La Riviere, P.J., Bian, J., and Vargas, P.A. 2006. Penalized-likelihood sinogram restoration for computed tomography. *IEEE Trans Med Imaging* 25:1022-1036.
29. Fu, J., and Lu, H.N. 2006. Beam-hardening correction method based on original sinogram for X-CT. *Nuclear Instruments & Methods in Physics Research Section a-Accelerators Spectrometers Detectors and Associated Equipment* 556:379-385.
30. Burch, S.F. 2001. X-ray computerised tomography for quantitative measurement of density variations in materials. *Insight* 43:29-31.
31. Chen, C.Y., Chuang, K.S., Wu, J., Lin, H.R., and Li, M.J. 2001. Beam hardening correction for computed tomography images using a postreconstruction method and equivalent tissue concept. *Journal of Digital Imaging* 14:54-61.
32. de Paiva, R.F., Lynch, J., Rosenberg, E., and Bisiaux, M. 1998. A beam hardening correction for X-ray microtomography. *Ndt & E International* 31:17-22.

33. Kachelriess, M., Sourbelle, K., and Kalender, W.A. 2006. Empirical cupping correction: A first-order raw data precorrection for cone-beam computed tomography. *Medical Physics* 33:1269-1274.
34. Meagher, J.M., Mote, C.D., and Skinner, H.B. 1990. Ct Image Correction for Beam Hardening Using Simulated Projection Data. *Ieee Transactions on Nuclear Science* 37:1520-1524.
35. Mulder, L., Koolstra, J.H., and Van Eijden, T.M. 2004. Accuracy of microCT in the quantitative determination of the degree and distribution of mineralization in developing bone. *Acta Radiol* 45:769-777.
36. Postnov, A.A., Vinogradov, A.V., Van Dyck, D., Saveliev, S.V., and De Clerck, N.M. 2003. Quantitative analysis of bone mineral content by x-ray microtomography. *Physiological Measurement* 24:165-178.
37. Kirby, B.J., Davis, J.R., Grant, J.A., and Morgan, M.J. 1997. Monochromatic microtomographic imaging of osteoporotic bone. *Physics in Medicine and Biology* 42:1375-1385.
38. Lopes, R.T., Costa, E.B., and de Jesus, E.F.O. 2000. Computed tomography with monochromatic bremsstrahlung radiation. *Applied Radiation and Isotopes* 53:665-671.
39. Byers, P.H., and Cole, W.G. 2002. Osteogenesis Imperfecta. In *Connective tissue and its heritable disorders : molecular, genetic, and medical aspects*. P.M. Royce, and B.U. Steinmann, editors. New York: Wiley-Liss. xvii, 1201 p.
40. Dalgleish, R. 1997. The human type I collagen mutation database. *Nucleic Acids Res* 25:181-187.
41. Marini, J.C., Forlino, A., Cabral, W.A., Barnes, A.M., San Antonio, J.D., Milgrom, S., Hyland, J.C., Korkko, J., Prockop, D.J., De Paepe, A., et al. 2007. Consortium for osteogenesis imperfecta mutations in the helical domain of type I collagen: regions rich in lethal mutations align with collagen binding sites for integrins and proteoglycans. *Hum Mutat* 28:209-221.
42. Boskey, A.L., Wright, T.M., and Blank, R.D. 1999. Collagen and bone strength. *Journal of Bone and Mineral Research* 14:330-335.
43. Van Dijk, F.S., Pals, G., Van Rijn, R.R., Nikkels, P.G., and Cobben, J.M. 2009. Classification of Osteogenesis Imperfecta revisited. *Eur J Med Genet*.
44. Glorieux, F.H., Rauch, F., Plotkin, H., Ward, L., Travers, R., Roughley, P., Lalic, L., Glorieux, D.F., Fassier, F., and Bishop, N.J. 2000. Type V osteogenesis imperfecta: a new form of brittle bone disease. *J Bone Miner Res* 15:1650-1658.
45. Chang, W., Barnes, A.M., Cabral, W.A., Bodurtha, J.N., and Marini, J.C. 2009. Prolyl 3-Hydroxylase 1 and CRTAP are Mutually Stabilizing in the Endoplasmic Reticulum Collagen Prolyl 3-Hydroxylation Complex. *Hum Mol Genet*.
46. Horwitz, E.M., Prockop, D.J., Fitzpatrick, L.A., Koo, W.W., Gordon, P.L., Neel, M., Sussman, M., Orchard, P., Marx, J.C., Pyeritz, R.E., et al. 1999. Transplantability and therapeutic effects of bone marrow-derived

mesenchymal cells in children with osteogenesis imperfecta. *Nat Med* 5:309-313.
47. Marini, J.C., Hopkins, E., Glorieux, F.H., Chrousos, G.P., Reynolds, J.C., Gundberg, C.M., and Reing, C.M. 2003. Positive linear growth and bone responses to growth hormone treatment in children with types III and IV osteogenesis imperfecta: high predictive value of the carboxyterminal propeptide of type I procollagen. *J Bone Miner Res* 18:237-243.
48. Castillo, H., Samson-Fang, L., American Academy for Cerebral, P., and Developmental Medicine Treatment Outcomes Committee Review, P. 2009. Effects of bisphosphonates in children with osteogenesis imperfecta: an AACPDM systematic review. *Dev Med Child Neurol* 51:17-29.
49. Cheung, M.S., Glorieux, F.H., and Rauch, F. 2007. Natural history of hyperplastic callus formation in osteogenesis imperfecta type V. *Journal of Bone and Mineral Research* 22:1181-1186.
50. Ramirez, N., Vilella, F.E., Colon, M., and Flynn, J.M. 2003. Osteogenesis imperfecta and hyperplastic callus formation in a family: a report of three cases and a review of the literature. *J Pediatr Orthop B* 12:88-96.
51. Kamoun-Goldrat, A.S., and Le Merrer, M.F. 2007. Animal models of osteogenesis imperfecta and related syndromes. *J Bone Miner Metab* 25:211-218.
52. Muriel, M.P., Bonaventure, J., Stanescu, R., Maroteaux, P., Guenet, J.L., and Stanescu, V. 1991. Morphological and biochemical studies of a mouse mutant (fro/fro) with bone fragility. *Bone* 12:241-248.
53. Sillence, D.O., Ritchie, H.E., Dibbayawan, T., Eteson, D., and Brown, K. 1993. Fragilitas ossium (fro/fro) in the mouse: a model for a recessively inherited type of osteogenesis imperfecta. *Am J Med Genet* 45:276-283.
54. Morello, R., Bertin, T.K., Chen, Y., Hicks, J., Tonachini, L., Monticone, M., Castagnola, P., Rauch, F., Glorieux, F.H., Vranka, J., et al. 2006. CRTAP is required for prolyl 3- hydroxylation and mutations cause recessive osteogenesis imperfecta. *Cell* 127:291-304.
55. Cassella, J.P., Pereira, R., Khillan, J.S., Prockop, D.J., Garrington, N., and Ali, S.Y. 1994. An ultrastructural, microanalytical, and spectroscopic study of bone from a transgenic mouse with a COL1.A1 pro-alpha-1 mutation. *Bone* 15:611-619.
56. Khillan, J.S., Olsen, A.S., Kontusaari, S., Sokolov, B., and Prockop, D.J. 1991. Transgenic mice that express a mini-gene version of the human gene for type I procollagen (COL1A1) develop a phenotype resembling a lethal form of osteogenesis imperfecta. *J Biol Chem* 266:23373-23379.
57. Pereira, R.F., Hume, E.L., Halford, K.W., and Prockop, D.J. 1995. Bone Fragility in Transgenic Mice Expressing a Mutated Gene for Type-I Procollagen (Col1a1) Parallels the Age-Dependent Phenotype of Human Osteogenesis Imperfecta. *Journal of Bone and Mineral Research* 10:1837-1843.
58. Prockop, D.J., Colige, A., Helminen, H., Khillan, J.S., Pereira, R., and Vandenberg, P. 1993. Mutations in type 1 procollagen that cause

osteogenesis imperfecta: effects of the mutations on the assembly of collagen into fibrils, the basis of phenotypic variations, and potential antisense therapies. *J Bone Miner Res* 8 Suppl 2:S489-492.
59. Daley, E., Streeten, E.A., Sorkin, J.D., Kuznetsova, N., Shapses, S.A., Carleton, S.M., Shuldiner, A.R., Marini, J.C., Phillips, C.L., Goldstein, S.A., et al. 2009. Variable Bone Fragility Associated with an Amish COL1A2 Variant and a Knock-in Mouse Model. *J Bone Miner Res*.
60. Chipman, S.D., Sweet, H.O., McBride, D.J., Jr., Davisson, M.T., Marks, S.C., Jr., Shuldiner, A.R., Wenstrup, R.J., Rowe, D.W., and Shapiro, J.R. 1993. Defective pro alpha 2(I) collagen synthesis in a recessive mutation in mice: a model of human osteogenesis imperfecta. *Proc Natl Acad Sci U S A* 90:1701-1705.
61. Pihlajaniemi, T., Dickson, L.A., Pope, F.M., Korhonen, V.R., Nicholls, A., Prockop, D.J., and Myers, J.C. 1984. Osteogenesis imperfecta: cloning of a pro-alpha 2(I) collagen gene with a frameshift mutation. *J Biol Chem* 259:12941-12944.
62. Saban, J., Zussman, M.A., Havey, R., Patwardhan, A.G., Schneider, G.B., and King, D. 1996. Heterozygous oim mice exhibit a mild form of osteogenesis imperfecta. *Bone* 19:575-579.
63. Camacho, N.P., Hou, L., Toledano, T.R., Ilg, W.A., Brayton, C.F., Raggio, C.L., Root, L., and Boskey, A.L. 1999. The material basis for reduced mechanical properties in oim mice bones. *J Bone Miner Res* 14:264-272.
64. Grabner, B., Landis, W.J., Roschger, P., Rinnerthaler, S., Peterlik, H., Klaushofer, K., and Fratzl, P. 2001. Age- and genotype-dependence of bone material properties in the osteogenesis imperfecta murine model (oim). *Bone* 29:453-457.
65. McBride, D.J., Jr., Shapiro, J.R., and Dunn, M.G. 1998. Bone geometry and strength measurements in aging mice with the oim mutation. *Calcif Tissue Int* 62:172-176.
66. Phillips, C.L., Bradley, D.A., Schlotzhauer, C.L., Bergfeld, M., Libreros-Minotta, C., Gawenis, L.R., Morris, J.S., Clarke, L.L., and Hillman, L.S. 2000. Oim mice exhibit altered femur and incisor mineral composition and decreased bone mineral density. *Bone* 27:219-226.
67. Delos, D., Yang, X., Ricciardi, B.F., Myers, E.R., Bostrom, M.P., and Camacho, N.P. 2008. The effects of RANKL inhibition on fracture healing and bone strength in a mouse model of osteogenesis imperfecta. *J Orthop Res* 26:153-164.
68. Barker, D.D., Wu, H., Hartung, S., Breindl, M., and Jaenisch, R. 1991. Retrovirus-induced insertional mutagenesis: mechanism of collagen mutation in Mov13 mice. *Mol Cell Biol* 11:5154-5163.
69. Harbers, K., Kuehn, M., Delius, H., and Jaenisch, R. 1984. Insertion of retrovirus into the first intron of alpha 1(I) collagen gene to embryonic lethal mutation in mice. *Proc Natl Acad Sci U S A* 81:1504-1508.
70. Bonadio, J., Saunders, T.L., Tsai, E., Goldstein, S.A., Morris-Wiman, J., Brinkley, L., Dolan, D.F., Altschuler, R.A., Hawkins, J.E., Jr., Bateman,

J.F., et al. 1990. Transgenic mouse model of the mild dominant form of osteogenesis imperfecta. *Proc Natl Acad Sci U S A* 87:7145-7149.
71. Bonadio, J., Jepsen, K.J., Mansoura, M.K., Jaenisch, R., Kuhn, J.L., and Goldstein, S.A. 1993. A murine skeletal adaptation that significantly increases cortical bone mechanical properties. Implications for human skeletal fragility. *J Clin Invest* 92:1697-1705.
72. Jepsen, K.J., Goldstein, S.A., Kuhn, J.L., Schaffler, M.B., and Bonadio, J. 1996. Type-I collagen mutation compromises the post-yield behavior of Mov13 long bone. *J Orthop Res* 14:493-499.
73. Jepsen, K.J., Schaffler, M.B., Kuhn, J.L., Goulet, R.W., Bonadio, J., and Goldstein, S.A. 1997. Type I collagen mutation alters the strength and fatigue behavior of Mov13 cortical tissue. *J Biomech* 30:1141-1147.
74. Forlino, A., Porter, F.D., Lee, E.J., Westphal, H., and Marini, J.C. 1999. Use of the Cre/lox recombination system to develop a non-lethal knock-in murine model for osteogenesis imperfecta with an alpha1(I) G349C substitution. Variability in phenotype in BrtlIV mice. *J Biol Chem* 274:37923-37931.
75. Kozloff, K.M., Carden, A., Bergwitz, C., Forlino, A., Uveges, T.E., Morris, M.D., Marini, J.C., and Goldstein, S.A. 2004. Brittle IV mouse model for osteogenesis imperfecta IV demonstrates postpubertal adaptations to improve whole bone strength. *J Bone Miner Res* 19:614-622.
76. Uveges, T.E., Collin-Osdoby, P., Cabral, W.A., Ledgard, F., Goldberg, L., Bergwitz, C., Forlino, A., Osdoby, P., Gronowicz, G.A., and Marini, J.C. 2008. Cellular mechanism of decreased bone in Brtl mouse model of OI: imbalance of decreased osteoblast function and increased osteoclasts and their precursors. *J Bone Miner Res* 23:1983-1994.
77. Uveges, T.E., Kozloff, K.M., Ty, J.M., Ledgard, F., Raggio, C.L., Gronowicz, G., Goldstein, S.A., and Marini, J.C. 2009. Alendronate treatment of the brtl osteogenesis imperfecta mouse improves femoral geometry and load response before fracture but decreases predicted material properties and has detrimental effects on osteoblasts and bone formation. *J Bone Miner Res* 24:849-859.
78. Boden, S.D., Schimandle, J.H., and Hutton, W.C. 1995. An experimental lumbar intertransverse process spinal fusion model. Radiographic, histologic, and biomechanical healing characteristics. *Spine (Phila Pa 1976)* 20:412-420.
79. Gruber, H.E., Gordon, B., Williams, C., Ingram, J.A., Norton, H.J., and Hanley, E.N., Jr. 2009. A new small animal model for the study of spine fusion in the sand rat: pilot studies. *Lab Anim* 43:272-277.
80. Salamon, M.L., Althausen, P.L., Gupta, M.C., and Laubach, J. 2003. The effects of BMP-7 in a rat posterolateral intertransverse process fusion model. *J Spinal Disord Tech* 16:90-95.
81. Schimandle, J.H., and Boden, S.D. 1994. Spine update. The use of animal models to study spinal fusion. *Spine (Phila Pa 1976)* 19:1998-2006.

82. Colnot, C., Romero, D.M., Huang, S., and Helms, J.A. 2005. Mechanisms of action of demineralized bone matrix in the repair of cortical bone defects. *Clin Orthop Relat Res*:69-78.
83. Lutolf, M.P., Weber, F.E., Schmoekel, H.G., Schense, J.C., Kohler, T., Muller, R., and Hubbell, J.A. 2003. Repair of bone defects using synthetic mimetics of collagenous extracellular matrices. *Nat Biotechnol* 21:513-518.
84. Campbell, T.M., Wong, W.T., and Mackie, E.J. 2003. Establishment of a model of cortical bone repair in mice. *Calcif Tissue Int* 73:49-55.
85. Chiba, S., Okada, K., Lee, K., Segre, G.V., and Neer, R.M. 2001. Molecular analysis of defect healing in rat diaphyseal bone. *J Vet Med Sci* 63:603-608.
86. Wang, J. 2000. Spatial orientation of the microscopic elements of cortical repair bone. *Clin Orthop Relat Res*:265-277.
87. Cancedda, R., Giannoni, P., and Mastrogiacomo, M. 2007. A tissue engineering approach to bone repair in large animal models and in clinical practice. *Biomaterials* 28:4240-4250.
88. Einhorn, T.A. 1999. Clinically applied models of bone regeneration in tissue engineering research. *Clin Orthop Relat Res*:S59-67.
89. Holstein, J.H., Garcia, P., Histing, T., Kristen, A., Scheuer, C., Menger, M.D., and Pohlemann, T. 2009. Advances in the establishment of defined mouse models for the study of fracture healing and bone regeneration. *J Orthop Trauma* 23:S31-38.
90. Nunamaker, D.M. 1998. Experimental models of fracture repair. *Clin Orthop Relat Res*:S56-65.
91. O'Loughlin, P.F., Morr, S., Bogunovic, L., Kim, A.D., Park, B., and Lane, J.M. 2008. Selection and development of preclinical models in fracture-healing research. *J Bone Joint Surg Am* 90 Suppl 1:79-84.
92. Reichert, J.C., Saifzadeh, S., Wullschleger, M.E., Epari, D.R., Schutz, M.A., Duda, G.N., Schell, H., van Griensven, M., Redl, H., and Hutmacher, D.W. 2009. The challenge of establishing preclinical models for segmental bone defect research. *Biomaterials* 30:2149-2163.
93. Cullinane, D.M., Salisbury, K.T., Alkhiary, Y., Eisenberg, S., Gerstenfeld, L., and Einhorn, T.A. 2003. Effects of the local mechanical environment on vertebrate tissue differentiation during repair: does repair recapitulate development? *J Exp Biol* 206:2459-2471.
94. Smith-Adaline, E.A., Volkman, S.K., Ignelzi, M.A., Jr., Slade, J., Platte, S., and Goldstein, S.A. 2004. Mechanical environment alters tissue formation patterns during fracture repair. *J Orthop Res* 22:1079-1085.
95. Bonnarens, F., and Einhorn, T.A. 1984. Production of a standard closed fracture in laboratory animal bone. *J Orthop Res* 2:97-101.
96. An, Y., Friedman, R.J., Parent, T., and Draughn, R.A. 1994. Production of a standard closed fracture in the rat tibia. *J Orthop Trauma* 8:111-115.
97. Hiltunen, A., Vuorio, E., and Aro, H.T. 1993. A standardized experimental fracture in the mouse tibia. *J Orthop Res* 11:305-312.

98. Manigrasso, M.B., and O'Connor, J.P. 2004. Characterization of a closed femur fracture model in mice. *J Orthop Trauma* 18:687-695.
99. Oetgen, M.E., Merrell, G.A., Troiano, N.W., Horowitz, M.C., and Kacena, M.A. 2008. Development of a femoral non-union model in the mouse. *Injury* 39:1119-1126.
100. Lindsey, B.A., Clovis, N.B., Smith, E.S., Salihu, S., and Hubbard, D.F. 2009. An animal model for open femur fracture and osteomyelitis: Part I. *J Orthop Res*.
101. Histing, T., Holstein, J.H., Garcia, P., Matthys, R., Kristen, A., Claes, L., Menger, M.D., and Pohlemann, T. 2009. Ex vivo analysis of rotational stiffness of different osteosynthesis techniques in mouse femur fracture. *J Orthop Res* 27:1152-1156.
102. Tiyapatanaputi, P., Rubery, P.T., Carmouche, J., Schwarz, E.M., O'Keefe R, J., and Zhang, X. 2004. A novel murine segmental femoral graft model. *J Orthop Res* 22:1254-1260.
103. Cranney, A., Guyatt, G., Griffith, L., Wells, G., Tugwell, P., Rosen, C., Osteoporosis Methodology, G., and The Osteoporosis Research Advisory, G. 2002. Meta-analyses of therapies for postmenopausal osteoporosis. IX: Summary of meta-analyses of therapies for postmenopausal osteoporosis. *Endocr Rev* 23:570-578.
104. Cummings, S.R., San Martin, J., McClung, M.R., Siris, E.S., Eastell, R., Reid, I.R., Delmas, P., Zoog, H.B., Austin, M., Wang, A., et al. 2009. Denosumab for prevention of fractures in postmenopausal women with osteoporosis. *N Engl J Med* 361:756-765.
105. Bone, H.G., McClung, M.R., Roux, C., Recker, R.R., Eisman, J.A., Verbruggen, N., Hustad, C.M., Dasilva, C., Santora, A.C., and Ince, B.A. 2009. Odanacatib, a Cathepsin-K Inhibitor for Osteoporosis: A Two-Year Study in Postmenopausal Women With Low Bone Density. *J Bone Miner Res*.
106. Ryaby, J.T. 2005. Biophysical Stimulation Using Electircal, Electromagnetic, and Ultrasonic Fields: Effects on Fracture Healing and Spinal Fusion. In *Bone regeneration and repair: biology and clinical applications*. J.R. Lieberman, and G.E. Friedlaender, editors. Totowa, NJ: Humana Press. 291-309.
107. Lubbert, P.H., van der Rijt, R.H., Hoorntje, L.E., and van der Werken, C. 2008. Low-intensity pulsed ultrasound (LIPUS) in fresh clavicle fractures: a multi-centre double blind randomised controlled trial. *Injury* 39:1444-1452.
108. Mollon, B., da Silva, V., Busse, J.W., Einhorn, T.A., and Bhandari, M. 2008. Electrical stimulation for long-bone fracture-healing: a meta-analysis of randomized controlled trials. *J Bone Joint Surg Am* 90:2322-2330.
109. Patil, S., Holt, G., Raby, N., McLellan, A.R., Smith, K., O'Kane, S., Beastall, G., and Crossan, J.F. 2009. Prospective, double blind, randomized, controlled trial of simvastatin in human fracture healing. *J Orthop Res* 27:281-285.

110. Doetsch, A.M., Faber, J., Lynnerup, N., Watjen, I., Bliddal, H., and Danneskiold-Samsoe, B. 2004. The effect of calcium and vitamin D3 supplementation on the healing of the proximal humerus fracture: a randomized placebo-controlled study. *Calcif Tissue Int* 75:183-188.
111. Pettway, G.J., Schneider, A., Koh, A.J., Widjaja, E., Morris, M.D., Meganck, J.A., Goldstein, S.A., and McCauley, L.K. 2005. Anabolic actions of PTH (1-34): use of a novel tissue engineering model to investigate temporal effects on bone. *Bone* 36:959-970.
112. Barnes, G.L., Kakar, S., Vora, S., Morgan, E.F., Gerstenfeld, L.C., and Einhorn, T.A. 2008. Stimulation of fracture-healing with systemic intermittent parathyroid hormone treatment. *J Bone Joint Surg Am* 90 Suppl 1:120-127.
113. Schmidmaier, G., Wildemann, B., Heeger, J., Gabelein, T., Flyvbjerg, A., Bail, H.J., and Raschke, M. 2002. Improvement of fracture healing by systemic administration of growth hormone and local application of insulin-like growth factor-1 and transforming growth factor-beta1. *Bone* 31:165-172.
114. Raschke, M., Rasmussen, M.H., Govender, S., Segal, D., Suntum, M., and Christiansen, J.S. 2007. Effects of growth hormone in patients with tibial fracture: a randomised, double-blind, placebo-controlled clinical trial. *Eur J Endocrinol* 156:341-351.
115. Boatright, K.C., and Boden, S.D. 2005. Biology of Spine Fusion: Biology and Clinical Applications. In *Bone regeneration and repair: biology and clinical applications*. J.R. Lieberman, and G.E. Friedlaender, editors. Totowa, NJ: Humana Press. 225-239.
116. Friedlaender, G.E., Perry, C.R., Cole, J.D., Cook, S.D., Cierny, G., Muschler, G.F., Zych, G.A., Calhoun, J.H., LaForte, A.J., and Yin, S. 2001. Osteogenic protein-1 (bone morphogenetic protein-7) in the treatment of tibial nonunions. *J Bone Joint Surg Am* 83-A Suppl 1:S151-158.
117. Govender, S., Csimma, C., Genant, H.K., Valentin-Opran, A., Amit, Y., Arbel, R., Aro, H., Atar, D., Bishay, M., Borner, M.G., et al. 2002. Recombinant human bone morphogenetic protein-2 for treatment of open tibial fractures: a prospective, controlled, randomized study of four hundred and fifty patients. *J Bone Joint Surg Am* 84-A:2123-2134.
118. Jones, A.L., Bucholz, R.W., Bosse, M.J., Mirza, S.K., Lyon, T.R., Webb, L.X., Pollak, A.N., Golden, J.D., Valentin-Opran, A., and Group, B.M.P.E.i.S.f.T.T.-A.S. 2006. Recombinant human BMP-2 and allograft compared with autogenous bone graft for reconstruction of diaphyseal tibial fractures with cortical defects. A randomized, controlled trial. *J Bone Joint Surg Am* 88:1431-1441.
119. Murnaghan, M., McIlmurray, L., Mushipe, M.T., and Li, G. 2005. Time for treating bone fracture using rhBMP-2: a randomised placebo controlled mouse fracture trial. *J Orthop Res* 23:625-631.
120. Salkeld, S.L., Patron, L.P., Barrack, R.L., and Cook, S.D. 2001. The effect of osteogenic protein-1 on the healing of segmental bone defects treated with autograft or allograft bone. *J Bone Joint Surg Am* 83-A:803-816.

121. White, A.P., Vaccaro, A.R., Hall, J.A., Whang, P.G., Friel, B.C., and McKee, M.D. 2007. Clinical applications of BMP-7/OP-1 in fractures, nonunions and spinal fusion. *Int Orthop* 31:735-741.
122. Lyles, K.W., Colon-Emeric, C.S., Magaziner, J.S., Adachi, J.D., Pieper, C.F., Mautalen, C., Hyldstrup, L., Recknor, C., Nordsletten, L., Moore, K.A., et al. 2007. Zoledronic acid and clinical fractures and mortality after hip fracture. *N Engl J Med* 357:1799-1809.
123. Munns, C.F., Rauch, F., Zeitlin, L., Fassier, F., and Glorieux, F.H. 2004. Delayed osteotomy but not fracture healing in pediatric osteogenesis imperfecta patients receiving pamidronate. *J Bone Miner Res* 19:1779-1786.
124. Pizones, J., Plotkin, H., Parra-Garcia, J.I., Alvarez, P., Gutierrez, P., Bueno, A., and Fernandez-Arroyo, A. 2005. Bone healing in children with osteogenesis imperfecta treated with bisphosphonates. *J Pediatr Orthop* 25:332-335.
125. Amanat, N., Brown, R., Bilston, L.E., and Little, D.G. 2005. A single systemic dose of pamidronate improves bone mineral content and accelerates restoration of strength in a rat model of fracture repair. *J Orthop Res* 23:1029-1034.
126. Amanat, N., McDonald, M., Godfrey, C., Bilston, L., and Little, D. 2007. Optimal timing of a single dose of zoledronic acid to increase strength in rat fracture repair. *J Bone Miner Res* 22:867-876.
127. Bauss, F., Schenk, R.K., Hort, S., Muller-Beckmann, B., and Sponer, G. 2004. New model for simulation of fracture repair in full-grown beagle dogs: model characterization and results from a long-term study with ibandronate. *J Pharmacol Toxicol Methods* 50:25-34.
128. Bilston, L.E., Little, D.G., Smith, N.C., Williams, P., and Briody, J. 2002. Zoledronic acid improves the mechanical properties of normal and healing bone. *Clin Biomech (Bristol, Avon)* 17:716-718.
129. Koivukangas, A., Tuukkanen, J., Kippo, K., Jamsa, T., Hannuniemi, R., Pasanen, I., Vaananen, K., and Jalovaara, P. 2003. Long-term administration of clodronate does not prevent fracture healing in rats. *Clin Orthop Relat Res*:268-278.
130. Li, J., Mori, S., Kaji, Y., Kawanishi, J., Akiyama, T., and Norimatsu, H. 2000. Concentration of bisphosphonate (incadronate) in callus area and its effects on fracture healing in rats. *J Bone Miner Res* 15:2042-2051.
131. Li, J., Mori, S., Kaji, Y., Mashiba, T., Kawanishi, J., and Norimatsu, H. 1999. Effect of bisphosphonate (incadronate) on fracture healing of long bones in rats. *J Bone Miner Res* 14:969-979.
132. Peter, C.P., Cook, W.O., Nunamaker, D.M., Provost, M.T., Seedor, J.G., and Rodan, G.A. 1996. Effect of alendronate on fracture healing and bone remodeling in dogs. *J Orthop Res* 14:74-79.
133. Smith, E.J., McEvoy, A., Little, D.G., Baldock, P.A., Eisman, J.A., and Gardiner, E.M. 2004. Transient retention of endochondral cartilaginous matrix with bisphosphonate treatment in a long-term rabbit model of distraction osteogenesis. *J Bone Miner Res* 19:1698-1705.

134. McDonald, M.M., Dulai, S., Godfrey, C., Amanat, N., Sztynda, T., and Little, D.G. 2008. Bolus or weekly zoledronic acid administration does not delay endochondral fracture repair but weekly dosing enhances delays in hard callus remodeling. *Bone* 43:653-662.
135. Gilbert, R.S., and Wolfe, S.W. 2005. Vascularized Fibula Grafts. In *Bone regeneration and repair: biology and clinical applications*. J.R. Lieberman, and G.E. Friedlaender, editors. Totowa, NJ: Humana Press. 311-336.
136. Stevenson, S. 1999. Biology of bone grafts. *Orthop Clin North Am* 30:543-552.
137. Davy, D.T. 1999. Biomechanical issues in bone transplantation. *Orthop Clin North Am* 30:553-563.
138. Wheeler, D.L., and Enneking, W.F. 2005. Allograft bone decreases in strength in vivo over time. *Clin Orthop Relat Res*:36-42.
139. Ito, H., Koefoed, M., Tiyapatanaputi, P., Gromov, K., Goater, J.J., Carmouche, J., Zhang, X., Rubery, P.T., Rabinowitz, J., Samulski, R.J., et al. 2005. Remodeling of cortical bone allografts mediated by adherent rAAV-RANKL and VEGF gene therapy. *Nat Med* 11:291-297.
140. Koefoed, M., Ito, H., Gromov, K., Reynolds, D.G., Awad, H.A., Rubery, P.T., Ulrich-Vinther, M., Soballe, K., Guldberg, R.E., Lin, A.S., et al. 2005. Biological effects of rAAV-caAlk2 coating on structural allograft healing. *Mol Ther* 12:212-218.
141. Xie, C., Ming, X., Wang, Q., Schwarz, E.M., Guldberg, R.E., O'Keefe, R.J., and Zhang, X. 2008. COX-2 from the injury milieu is critical for the initiation of periosteal progenitor cell mediated bone healing. *Bone* 43:1075-1083.
142. Xie, C., Reynolds, D., Awad, H., Rubery, P.T., Pelled, G., Gazit, D., Guldberg, R.E., Schwarz, E.M., O'Keefe, R.J., and Zhang, X. 2007. Structural bone allograft combined with genetically engineered mesenchymal stem cells as a novel platform for bone tissue engineering. *Tissue Eng* 13:435-445.
143. Zhang, X., Xie, C., Lin, A.S., Ito, H., Awad, H., Lieberman, J.R., Rubery, P.T., Schwarz, E.M., O'Keefe, R.J., and Guldberg, R.E. 2005. Periosteal progenitor cell fate in segmental cortical bone graft transplantations: implications for functional tissue engineering. *J Bone Miner Res* 20:2124-2137.
144. Hench, L.L. 1991. Bioceramics: From Concept to Clinic. *Journal of the American Ceramic Society* 74:1487-1510.
145. Khan, Y., Yaszemski, M.J., Mikos, A.G., and Laurencin, C.T. 2008. Tissue engineering of bone: material and matrix considerations. *J Bone Joint Surg Am* 90 Suppl 1:36-42.
146. LeGeros, R.Z. 2002. Properties of osteoconductive biomaterials: calcium phosphates. *Clin Orthop Relat Res*:81-98.
147. Liu, X., and Ma, P.X. 2004. Polymeric scaffolds for bone tissue engineering. *Ann Biomed Eng* 32:477-486.

148. Rosso, F., Marino, G., Giordano, A., Barbarisi, M., Parmeggiani, D., and Barbarisi, A. 2005. Smart materials as scaffolds for tissue engineering. *J Cell Physiol* 203:465-470.
149. Sanchez, C., Arribart, H., and Guille, M.M. 2005. Biomimetism and bioinspiration as tools for the design of innovative materials and systems. *Nat Mater* 4:277-288.
150. Liao, S.S., and Cui, F.Z. 2004. In vitro and in vivo degradation of mineralized collagen-based composite scaffold: nanohydroxyapatite/collagen/poly(L-lactide). *Tissue Eng* 10:73-80.
151. Liao, S.S., Cui, F.Z., Zhang, W., and Feng, Q.L. 2004. Hierarchically biomimetic bone scaffold materials: nano-HA/collagen/PLA composite. *J Biomed Mater Res B Appl Biomater* 69:158-165.
152. Han, D., and Zhang, Q. 2006. An essential requirement for osteoclasts in refined bone-like tissue reconstruction in vitro. *Med Hypotheses* 67:75-78.
153. Cartmell, S., Huynh, K., Lin, A., Nagaraja, S., and Guldberg, R. 2004. Quantitative microcomputed tomography analysis of mineralization within three-dimensional scaffolds in vitro. *J Biomed Mater Res A* 69:97-104.
154. Mauney, J.R., Sjostorm, S., Blumberg, J., Horan, R., O'Leary, J.P., Vunjak-Novakovic, G., Volloch, V., and Kaplan, D.L. 2004. Mechanical stimulation promotes osteogenic differentiation of human bone marrow stromal cells on 3-D partially demineralized bone scaffolds in vitro. *Calcif Tissue Int* 74:458-468.
155. Nisbet, D.R., Forsythe, J.S., Shen, W., Finkelstein, D.I., and Horne, M.K. 2009. Review paper: a review of the cellular response on electrospun nanofibers for tissue engineering. *J Biomater Appl* 24:7-29.
156. Nakagawa, K., Abukawa, H., Shin, M.Y., Terai, H., Troulis, M.J., and Vacanti, J.P. 2004. Osteoclastogenesis on tissue-engineered bone. *Tissue Eng* 10:93-100.
157. Schilling, A.F., Linhart, W., Filke, S., Gebauer, M., Schinke, T., Rueger, J.M., and Amling, M. 2004. Resorbability of bone substitute biomaterials by human osteoclasts. *Biomaterials* 25:3963-3972.

CHAPTER 2: Beam Hardening Artifacts and Bone Densitometry in µCT

Introduction

The mechanical properties of bone tissue are determined by a variety of factors that range in size from the whole bone to the tissue ultrastructure. Bone mineral density (BMD) is one of these factors. BMD measurement methods continue to be an important area of research because ash content measurements, the gold standard for measuring mineral content in bone, are destructive and do not allow for measurement of site-specific mineral density patterns. To circumvent this, several non-destructive methods have been used to measure BMD in both clinical and basic science studies. While quantitative ultrasound methods have been used, the more typical methodologies use X-ray based imaging, such as single photon absorptimetry, dual photon absorptimetry, dual energy X-ray absorptimetry (DXA), peripheral quantitative computed tomography (pQCT), and micro-computed tomography (µCT).[1,2] DXA measurements have been a valuable screening tool for bone diseases, but the accuracy of DXA measurements has been questioned and DXA cannot account

for the three-dimensional architectural properties of bone.[2,3] To overcome the challenges of DXA, peripheral quantitative computed tomography (pQCT) has been used to separate trabecular bone from cortical bone and estimate mechanical strength.[4,5] While pQCT can assess both mineral content and structural properties in three dimensions from the same scan, its relatively low resolution can lead to errors when scanning small specimens.[6,7] The resolution of micro-computed tomography (μCT) images is superior to clinical pQCT and, as a result, μCT has become the standard for accurate morphological and mineral density measurements in many pre-clinical studies.[7]

The micro-radiographic techniques that form the foundation for quantitative μCT based density measurements were published nearly two decades ago.[8] At that time, only relative densities were reported because these values were not calibrated or validated against a standard. This relative density is difficult to verify because the CT image acquisition process is subject to artifacts from partial-voluming, photon starvation, photon scatter, under-sampling, and beam hardening.[9] Beam hardening is arguably the most problematic for accurate BMD quantification and is caused by a preferential absorption of the low energy photons. This results in artifacts that appear as cupping, streaks, dark bands, or flare artifacts.[9-11] Because most laboratory and clinical CT systems use sources that generate polychromatic X-ray spectra, beam hardening artifacts must be taken into account for accurate quantitative imaging.

Corrections for beam hardening can be applied during the image acquisition process, during image reconstruction, or as empirical corrections.

Procedures that are applied during the image acquisition process may require dual energy imaging. This corrects for beam hardening and can be used to minimize cupping, streak, and flare artifacts.[10,12,13] Reconstruction based approaches to prevent beam hardening artifacts in the 3D image can also be used in both dual-energy and single-energy imaging if the input spectrum is known,[14] or may require a thresholding step so that path lengths can be estimated.[11,15,16] Last, iterative reconstruction approaches based on Poisson distributions have also been proposed, both with and without the need for segmentation.[17-19] Despite the availability of sophisticated reconstruction algorithms, empirical corrections are arguably the most widely used class of beam hardening corrections. These can be applied prior to image reconstruction,[20,21] or applied to the reconstructed image by applying polynomial basis functions, linearization procedures, calibration curves, or conversion tables.[22-26]. These empirical approaches have been used in laboratory desktop µCT systems with some success, but the polynomial corrections that were used were not perfect and could not completely remove beam hardening artifacts for all cases.[27-29]

Despite the wealth of possibilities to correct for beam hardening artifacts that result from the use of polychromatic X-ray spectra, it would be preferable to avoid beam hardening artifacts altogether. Monochromatic synchrotron radiation can be used for µCT and can allow for accurate BMD assessments, but limited synchrotron access can make studies difficult.[30-32] While a crystal monochromator or band-pass filters can be used to convert a polychromatic

spectrum into a monochromatic or quasi-monochromatic spectra,[33,34] filtration is typically used to pre-harden the X-ray spectrum by removing low-energy X-rays. This common filtration approach can be enhanced by using water to ensure that the path lengths of the X-ray beam are approximately equivalent as they pass through the object being imaged.[35] Because beam hardening affects BMD measurements, the purpose of this study was to assess beam hardening artifacts associated with μCT imaging and ensure that accurate BMD measurements can be obtained. The accuracy of BMD measurements has previously been shown,[36] so the purpose of this study was to examine how beam hardening artifacts may affect these estimations. This was accomplished in a two part study. In the first part, X-ray filtration in conjunction with beam flattening was applied as a method to reduce cupping artifacts in bone-like materials. Beam hardening artifacts can also occur in scan setups that are commonly used for murine skeletal phenotyping, so these were investigated in the second part of this study.

Methods

Animal Use

Bones were harvested from mice for the second portion of this study. These mice were primarily utilized in other experiments that were performed under approval of the University Committee on the Use and Care of Animals (UCUCA) at the University of Michigan. Femora were dissected from 12 mice ranging in age from approximately one month to ten months. These mice were

maintained in colonies to investigate the effects of Thrombospondin 2, Thrombospondin 3, LRP5, and LRP6. While this study was not specifically designed to look at how these skeletal phenotypes change with age, these bones were chosen to minimize the effect of a particular phenotype or age on the results.[37-40]

Part 1: Assessment and quantification of beam hardening-induced cupping artifacts

Phantom Design

The ability of different filter materials and a beam flattener to reduce beam hardening induced cupping artifacts was assessed using a tower phantom design with 11 separate circular tiers combined into one object (Figure 1). The circular geometry was chosen because cupping artifacts are most prominent in circular sections. One phantom was made from a material that mimics cortical bone (SB3; physical density of 1.82 g/cm^3),[41] and a second phantom was made from CB2-50% (physical density of 1.56 g/cm^3) to represent bone with lower densities (Gammex RMI, Middleton, WI, USA).[42]

Image acquisition protocols & X-ray beam filtration

A commercially available µCT system was used (eXplore Locus SP, GE Healthcare Pre-Clinical Imaging, London, ON, Canada). This system uses a micro-focus source with an 8 µm focal spot size and a tungsten anode (Kevex PXS5-925EA, Thermo Scientific, Waltham, MA, USA). A source voltage of 80

kVp was used for this study to generate a spectrum that is primarily in the energy range of photoelectric absorption after filtration. In this system, five choices are available for beam filtration as X-rays exit the source: no added filtration, 0.254 mm aluminum (Al.), 0.508 mm Al, 1.016 mm Al, and 0.254 mm Al followed by 0.254 mm copper (Cu) (Table 1). Each of these filters affects the X-ray spectrum. To estimate this effect, the X-ray spectrum was estimated for the case of 0.010 in. Al filter.[43] Spectra for the other filters were then calculated using the freely available MATLAB code PhotonAttenuation2, which calculates photon attenuation based on NIST reference data. The specimens were immersed in distilled water and an acrylic beam flattener was used to equalize the beam path length within the field of view (Figure 2).

Current and integration times were selected to ensure that the photon statistics reaching the detector used approximately 75-85% of the dynamic range of the detector (Table 1). The scan setup utilized a magnification of 2.60 with 2x2 detector binning, resulting in an acquired pixel size of 18 μm. 720 projections were acquired for each individual scan over 360° of rotation. These projections were corrected using low-end and high-end outlier replacement in conjunction with a sinogram based long-term trend correction and reconstructed using a filtered cone-beam backprojection algorithm with a Ram-Lak filter to generate images with an isotropic voxel size of 18 μm.[44,45] To calibrate the system, a phantom containing air, water, and SB3 was scanned with the beam flattener for each acquisition protocol. In this calibration process, air was mapped to -1000

Hounsfield Units (HU), water was mapped to 0 HU, and the HU value of bone was extrapolated based on these two points.

Noise Measurement

X-ray beam filtration is known to affect the signal to noise ratio (SNR) and the contrast to noise ratio (CNR).[46,47] To determine how phantom material influences noise measurements , a cube region of interest that was 25x25x25 pixels in size was placed in 9 separate locations of pure water at regions adjacent to tiers 2-10 of the tower phantom. Tiers 1 and 11 were not used due to proximity to the top and bottom of the scan, and to alleviate partial volume artifacts at these tower levels. This process was repeated for each filter for both the SB3 and CB2-50% phantoms, with and without the beam flattener. At each water location, the standard deviation of the voxel grayscale values was calculated to estimate the noise level.[48]

Beam Hardening Quantification

To quantify the amount of beam hardening that occurred as a function of beam filtration, specimen thickness, and specimen material, two-dimensional slices were taken for each combination of these variables. Histograms were used to select global threshold ranges to delineate the specimen from water; one range was chosen for the Al and Cu filter and another range was chosen for the remaining filters (Figure 4). Single slice images were plotted and grayscale values were mapped onto a color scale using the limits determined from the

global thresholding procedure. A line plot across the center was then created and a 30 pixel wide moving average filter was applied to reduce noise so that cupping could be visually detected.

Beam hardening effects will be most apparent when comparing voxels near the tower edge, which should be relatively unaffected, to voxels near the tower center, which will be most affected. A stochastic sampling approach was used to quantify the amount of beam hardening. A lognormal distribution was defined for the outer portion of the phantom to avoid partial volume artifacts (Figure 3). A similar distribution was defined for the central portion of the phantom. These distributions both had values for the cumulative density function (CDF) of 0.995 at the half-tier radius. An outer voxel value was selected by defining a random radius based on the outer sampling distribution, and a pseudorandom angle selected from a uniform distribution over the interval $[0,2\pi]$. This process was repeated using the central voxel distribution. In this manner, voxels were sampled with replacement for 10^6 iterations, and the mean grayscale differences and percent differences were calculated between the sampled outer voxel population and inner voxel population. Beam hardening artifacts were considered significant when the difference between central and edge population means was greater than the baseline noise level.

BMD Quantification

To quantify how cupping artifacts affect BMD measurements, commercially available software was used to quantify the mineral density

(MicroView 2.2 Advanced Bone Analysis Application, GE Healthcare – Pre-clinical imaging, London, ON, Canada). In this software, the voxel grayscale value for SB3 in a manufacturer provided phantom is correlated to a physical mineral density of 1073 mg/cc and voxel mineral contents are calculated using a linear correlation. The mineral densities for all other tissues are either interpolated or extrapolated based on this point and water at 0 HU with 0 mg/cc of mineral. For our own phantoms, these relationships resulted in an estimated mineral density of 1056 mg/cc for SB3 and 695 mg/cc for CB2-50%. The slight difference in estimated SB3 mineral densities was verified in a side by side comparison and may represent manufacturing inhomogeneities because these two materials were obtained at different times and came in slightly different forms. Global threshold levels were chosen based on the histograms of the phantom material to make tissue specific measurements.

Statistical Analysis

Noise levels for every filter both with and without the beam flattener were compared using a two-way ANOVA. This was followed with a one-way ANOVA using Tukey's post-hoc text (MATLAB, Statistics toolbox, Mathworks Inc., Natick, MA, USA) to determine pairwise differences between filters within each material and flattener condition.

Part 2: Assessment of scan protocol parameters that contribute to accurate density measurements

Image Acquisition

Femora were scanned on the same μCT system used in the first part of this study. The scan protocol entailed the use of the beam flattener with a 0.508 mm Al. filter, the source set at 80 kVp and 80 μA, a magnification of 2.60 an exposure time of 1600 ms and an increment angle of 0.5°. The images were reconstructed using a Feldkamp cone beam backprojection algorithm with a Ram-Lak filter to obtain an isotropic voxel size of 18 μm. To determine if artifacts affect mineral density measurements and common morphometric parameters in setups used to increase throughput, these bones were scanned using four methods. In the first method, 4 bones were simultaneously scanned using acquisitions limited to 200° of rotation to represent the shortest scan time. To examine artifacts in the reconstructed images caused by scanning multiple bones simultaneously, the same bones were then scanned individually over 200° of rotation. In this scanner, 200° of sample rotation was used because it is 180° plus the cone angle, representing the minimal complete data set for a reconstruction.[49] To help elucidate artifacts which may result from this minimal data set, these bones were scanned 4 at a time over 360° of rotation. As a relative gold standard image that avoided these limitations, each bone was then individually scanned over 360° of rotation. In every scan setup, each bone was placed in a sample holder away from the center of rotation (Figure 2). When 4 bones were scanned simultaneously, this configuration resulted in X-rays

transmitting through two separate samples for some projection images. The scanner was calibrated once daily using a three point calibration of water, air, and SB3 to account for underlying day to day variation in the system stability.

Image Analysis

A standard image analysis procedure was used to analyze the morphologic and mineral density measurements from these bones. Briefly, the images were reformatted using tricubic interpolations to align the long axis of the bone with a principal axis of the image. Images for each common bone were then registered using a rigid-body transform (translation and rotation) based on the selection of 4 sets of fiducial points. The femoral length was measured on the image of the bones scanned individually over 360°, and the region of interest (ROI) were normalized to this length. For the cortical bone, a ROI that was 20% of the femoral length was placed in the mid-diaphysis. For the trabecular bone, a ROI that was 10% of the femoral length was placed in the distal metaphysis. Trabecular bone was semi-automatically segmented from cortical bone by defining splines along the cortical-trabecular interface no more than 10 CT slices apart followed by linear interpolation between these selections. Because the images were registered, only one cortical and one trabecular ROI were defined for each bone. Based on these ROIs, the morphology and mineral density of the cortical bone and trabecular bone (using standard stereological techniques) were measured using commercially available software (MicroView 2.2 Advanced Bone Analysis, GE Healthcare Pre-Clinical Imaging). The same set of global thresholds

was used for each image (one threshold for the cortical bone and one threshold for the trabecular bone).

Statistical Analysis

To analyze the data, a subset of the variables was chosen to capture the morphologic and density properties of interest while limiting dependencies between the data points. To assess cortical bone morphology, the cortical thickness, moment of inertia, outer perimeter, and cross-sectional areas were measured. To assess the trabecular bone morphology, only the BV/TV ratio and trabecular number were analyzed because these are the only two independent measures using stereologic approaches. For densitometry assessments, both the mineral content and mineral density values were examined, even though they are mathematically related, because both have a unique physiologic interpretation. A repeated measures ANOVA was used for each variable to compare the data between the four scan protocols using a mixed linear model (SPSS 16, SPSS Inc., Chicago, IL, USA). Post-hoc tests were performed to determine pairwise differences using data for the bones scanned individually over 360° as a reference. Bonferroni corrections were used to adjust for multiple comparisons (α=0.05 after adjustment).

Results

Part 1: Assessment and quantification of beam hardening induced cupping artifacts

X-ray spectral comparison & Histogram assessment

Results of the X-ray spectral comparison show a decrease in spectral height between the filter with 0.254 mm Al and 0.254 mm Cu and all other filters due to the decrease in the number of photons (Figure 5). As the amount of filtration increases, there is also an upward shift in the mean energy of the spectrum. The weighted mean energies were 40.7525, 41.4193, 42.5701 and 51.3822 kV for filters the 0.254 mm Al, 0.508 mm Al, 1.016 mm Al and 0.254 mm Al / 0.254 mm Cu filters, respectively. This upward shift resulted in less attenuation and decrease in contrast, as shown on the histograms (Figure 4). As a result of this contrast change, the thresholds chosen depended on the amount of filtration. For SB3, the values 2200-3200 HU were used for the 0.254 mm Al/0.254 mm Cu filter and the values 2000-4300 were the 0.254 mm Al/0.254 mm Cu filter and the values 1600-3200HU were used for all other filters. In addition to this, there was also a change in peak shape when noticeable beam hardening artifacts occurred.

Noise Measurement

To characterize effects of tower thickness, material, and presence or absence of the beam flattener on baseline noise levels, cubic regions of interest in 9 locations of water were analyzed adjacent to 9 levels of both tower

phantoms. In the presence of each material, both the beam flattener and filter affect baseline noise levels, but there is no interaction between the two (for the interaction term: p=0.9868 for the CB2-50% phantom; p=0.8342 for the SB3 phantom). Because no interaction was present, the effects of the flattener and the filters were interpreted separately. In the presence of both materials, there was a statistically significant increase in the amount of measured noise when the flattener was used (Figure 6: p=0.0009 for the CB2-50% phantom; p= 0.0276 for the SB3 phantom). When the noise levels were compared across the filters, results of the ANOVA analysis indicated that there were some statistically significant differences ($p<0.0001$ for the CB2-50% phantom; p=0.0001 for the SB3 phantom). Post-hoc tests indicated that there was more noise with the 0.254 mm Al/0.254 mm Cu filter for all cases except when compared to the 1.016 mm Al filter with SB3. In the presence of CB2-50% phantom, there was also more noise with the 1.016 mm Al filter than with the the 0.254 mm Al filter (Figure 6).To determine a cutoff point for beam hardening quantification (see the section on Beam Hardening Quantification below), the noise measurements for no filtration and the three Al filters were averaged resulting in baseline noise levels of 116 HU and 109 HU for in the presence of CB2-50% with and without the flattener, respectively, and 124 HU and 119 HU in the presence of SB3 with and without the flattener, respectively. Data from the 0.254 mm Al/0.254 mm Cu filter was not included in these calculations because no measureable cupping occurred with this filter.

Beam Hardening Quantification

Histograms were used to establish global threshold levels (Figure 4). Lower threshold ranges were required for the filter with Cu, coinciding with a decrease in contrast as beam filtration increases. In addition, there was a change in the histogram peak shape for thicker portions of the phantom due to cupping artifacts. To determine the specimen thickness where beam hardening artifacts begin to occur, a stochastic approach was used to find the difference in grayscale values between the outer and central portions of the phantom. We assumed that significant beam hardening artifacts occurred when this difference was greater than the baseline noise level. The results indicate that both filtration and use of the beam flattener affect the onset of beam hardening artifacts. Tables 2 and 3 summarize the percentage changes between the inside and outside of the phantom for all cases. Tables 4 and 5 show the corresponding HU quantifications, and Figures 7-10 show visualizations of the results. The thickness where cupping artifacts becomes significant increases as the amount of filtration increases. No significant cupping artifacts occurred for any thickness tested for either material when the filter containing Al and Cu was was used. After cupping began to occur, the magnitude of the change increased as the phantom became thicker.

BMD estimation

The ultimate utility of uCT is bone mineral density measurements rather than beam hardening quantifications. We calculated the tissue mineral densities

(TMD) for the SB3 and CB2-50% phantoms from scans that were obtained both with, and without, the beam flattener (Figure 11). Here, we define TMD as the Bone Mineral Content of a region of interest normalized by bone volume of that region, creating a true volumetric measure of mineral density independent of bone size and shape. There was no measureable change in the TMD measurements from the expected density values when the filter of 0.254 mm Cu and 0. 254 mm Al was used for either material in either scan condition. However, for the other filter materials, the least amount filtration corresponded with the greatest difference from the expected TMD value for both materials. For the test conditions without the beam flattener, there was a deviation from the expected TMD values even for the smallest diameter.

Part 2: Assessment of scan protocol parameters that contribute to accurate density measurements

Quantification of the cortical thickness, moment of inertia, and outer perimeter indicated that there are some statistically significant differences when the specimens are scanned 4 at a time in comparison to when the bones were scanned individually. However, there were no differences in the measured cross-sectional areas, the value for the mean thickness difference was less than the size of a voxel, and the thickness difference was within the range of error previously reported for a similar methodology.[50] Because of the mathematical relationship between thickness, moment of inertia, perimeter and cross-sectional area, we believe that these sub-voxel differences in morphology do not represent

meaningful changes that occurred because of the scan protocol. When the trabecular bone morphology was examined, the results also indicated that there was a statistically significant decrease in the measured bone volume fraction with multiple bones in the path of the x-ray beam when the bones were over 200° ($p = 0.002$) and a trend toward a measured decrease when the bones were scanned over 360° ($p = 0.080$) (Figure 12E). However, the difference only represented a 2% change in the volume fraction. Therefore, this may not represent a physiologically meaningful change. Likewise, analysis of the trabecular number indicates that scanning 4 bones simultaneously over 360° results in fewer measured trabeculae than when the bones are scanned individually over 360° (Figure 12F). For the densitometry measures, the results indicate that scanning the bones individually over 200° results in a statistically significant ($p < 0.001$) and meaningful increase in the measured mineral content and mineral density of cortical bone (Figure 12A,B). The results from the mineral content and density measurements of trabecular bone were slightly different. In these analyses, simultaneously scanning over 200° results in a significant underestimation of the tissue mineral content (TMC) ($p = 0.042$), and a trend toward a decrease over 360° ($p = 0.058$) (Figure 12C). When these measurements are normalized to the volume of bone, both protocols that used a scan angle of 200° resulted in a slight overestimation of the TMD ($p = 0.001$ for 4 bones simultaneously, $p = 0.011$ when bones were individually scanned). The protocol where 4 bones were simultaneously scanned over 360° resulted in an underestimation of the TMD ($p = 0.045$, Figure 12D).

Discussion

The overall goal of this study was to investigate interactions between beam hardening and mineral density measurements in μCT imaging. As a first goal, we attempted to determine when beam hardening-induced cupping artifacts occur in μCT imaging, how these artifacts impact BMD measurements, and determine the efficacy of beam filtration and beam flattening to reduce these artifacts. This theoretical example may not translate directly to research projects, so the possibility that artifacts may bias morphological and mineral density measurements was then investigated in a typical murine phenotyping study.

The quantitative results of these studies are specific to the μCT system in this study, but the principles still apply to all scanners that use a polychromatic x-ray tube. In fact, it is possible to make meaningful μCT based mineral density measurements using other scanners.[27-31,51] These systems utilized linearization procedures based on step wedge calibration or polynomial based approaches to correct the beam hardening artifacts, but even these corrections may be limited. The data in one of these studies indicates the ability to correct a skewed histogram,[29] similar to what was seen in this study using filtration. Similarly to the filtration in this study, errors of up to approximately 45% and 60% occurred with inadequate correction and could be reduced to less than 5% with the correct density-specific linearization.[27,31] While the data in this study could be used for this type of linearization correction, we have chosen to use filtration and an acrylic beam flattener to minimize the fundamental problem. These data

show that the beam flattener has the ability to reduce beam hardening artifacts. Furthermore, increasing the amount of filtration can minimize or reduce these artifacts. In general, the bone-like material SB3 was more prone to beam hardening artifacts than a similar material with a lower radiodensity (CB2-50%). The magnitude of the artifacts increased with thickness and corresponded to decreases in the measured BMD. Interestingly, the acrylic beam flattener did not seem to have as much of an effect in SB3 as it did in CB2-50%. The acrylic is similar to water and provided the same path length affect that water bags provided in early CT scanners,[35] so it was a reasonable first choice as a material. However, choosing a material that has a closer radiodensity match to SB3 may reduce the artifacts more.

The differences between the filter that used 0.254 mm Al and 0.254 mm Cu and the filter that used 1.016 mm Al were also evident. The filter that used Cu reduced cupping to an undetectable level for the thicknesses and materials tested in this study. This can be attributed to the difference in the x-ray spectrum after transmission through the filter with Cu (Figure 5). In fact, previous data have shown that the spectrum transmitted by a 0.10 mm Cu filter is a very close to the spectrum transmitted by a 3.7 mm Al filter.[52] Filtration can be used to reduce the radiation dose for in vivo imaging,[46,51,53] although the results of this study indicate a reduction in contrast and increase in noise with filtration. In fact, the decrease in contrast with the 0.254 mm Al and 0.254 mm Cu filter in this study required the use of an entirely separate color map to visualize this data. Last, as a practical issue, using the filter composed of 0.254 mm Al and 0.254 mm Cu

required a substantial increase in the integration time to obtain adequate photon statistics at the detector, resulting in scans that were approximately 3.5 to 3.75 times longer in comparison to no filtration. Therefore, many investigators use synchrotron based systems with monochromatic spectra. This has spurred interest in comparing synchrotron based systems with the more readily available laboratory systems.[31,32,54,55].

While the x-ray spectrum is arguably the most important consideration to control when trying to minimize beam hardening artifacts, it is also possible that other aspects of the image acquisition and/or reconstruction processes can influence the measurement results. Charge integrating detectors are less prone to beam hardening artifacts than photon counting detectors.[56] In addition, increasing the number of views can increase the SNR.[57] These facts led us to the second portion of this study where we investigated limitations that arise when imaging multiple samples with a short scan. Four mouse femurs were simultaneously scanned over 200° for the high throughput approach, and scanning each specimen individually over 360° was used as the relative gold standard. Cortical bone densitometry results suggest that imaging four bones simultaneously does not bias these measurements. This is not surprising since the longest path length for two sections of mouse cortical bone is smaller than the first tier of our SB3 phantom where no significant cupping was detected. However, limiting the number of views resulted in a statistically significant and meaningful increase in measurements of TMC and TMD in cortical bone when the bones were scanned individually. This may indicate that the ‘front’ bone acted

as a low level filter when the bones were scanned 4 at a time. We have seen evidence that this type of effect occurs in another study where only two mice tibias were simultaneously scanned (Figure 13).

This possibility is also supported by the densitometry measurements for trabecular bone. The beam path length for trabecular bone will be longer because of an increased amount of tissue. This would increase the likelihood for Compton scattering that may occur for some of the higher photon energies in this X-ray beam and cone beam effects may occur because the metaphysis is further from the center of the field of view. This could theoretically result in a lower density than expected for the second specimen in the beam path and, in fact, this occurred when four bones were simultaneously scanned over 360°. The trabecular bone data when the specimens were scanned individually shows the same overestimates for the mineral content and mineral density that were seen in cortical bone, futher reinforcing the bias induced by limiting the number of views. Just as for cortical bone, there is an interaction between limiting the number of views and potential beam hardening when four specimens were scanned simultaneously. The TMC measurements for these data indicate that the subtle beam hardening effect may be prevalent, whereas TMD measurements indicate that limiting the number of views may dominate, so the underlying cause is still difficult to discern since the TMD change can be mathematically attributed to the decrease in BV/TV. These distinctions may be avoidable in the future by increasing the amount of beam filtration used to scan mice bones, but they may also be attributed to the inherent difficulties in

assessing mouse trabecular bone structures. Limiting the number of views will reduce the SNR, and this may be particularly troublesome for trabecular bone due to resolution limitations that have been previously reported.[50,58-60] Only one of these studies is for mouse bones [50], and the voxel size used in this study was smaller than the 20μm voxel size that correlated well to their gold standard image.[50] It is still possible, however, that those images have a better spatial resolution than reported in this study because those images were obtained by digital downsampling that may not represent the actual resolution if the bones were scanned at that voxel size.[58]

There may still be other limitations in our assessment of the trabecular bone morphology and mineral density. First, we used a global thresholding approach that may limit the capability to obtain accurate quantifications. Partial volume artifacts around the edges of trabeculae can make thresholding difficult,[61] so several studies have previously attempted to validate different thresholding or segmentation algorithms.[61-67] Most of these studies validate the thresholding algorithm by comparing the μCT images to a histological reference standard. While we could have performed a similar comparison in this study to use as a gold standard, our main goal in the second part of this study was to understand the limitations of different μCT protocols. Using the protocol that generates the best image quality obtainable was adequate for the comparisons of interest.

The end goal for these analyses is to have accurate measures of the mineral density. The only way to verify these measurements is to compare them with

physical measurements which, for the case of mineral content data, is typically performed by ashing. This has been previously done using a scanner that is nearly identical to the one used in this study using murine vertebral bodies.[36] Femora may be slightly different than vertebra, but the TMC and TMD data for the femora were a statistical average, so we believe the data are similar. Furthermore, we cannot claim that to make mineral density estimates on a voxel by voxel level in our system because this type of measurement would be prone to image quality issues such as noise, partial volume artifacts, center of rotation artifacts and motion artifacts. However, it is possible to visualize patterns of mineralization that are based on the grayscale values.

There are also other limitations of this work. The studies are presented here in the logical order of understanding how beam hardening affects BMD measurements, and then investigating how the scan setup affects BMD measurements. Despite this presentation, the chronological order of these studies was the exact opposite of this presentation. The use of 0.508 mm Al filtration in the first study compares directly to the amount of filtration used in the second. The path lengths where artifacts began to occur with this amount filtration were longer than typical path lengths for mouse femora or veterbrae so it is unclear if this would be a problem. Furthermore, increasing the amount filtration increases noise, so the precision of densitometry measurements could plausibly decrease if more filtration was used. However, the accuracy should be consistent as long as beam attenuation is dominated by photoelectric absorption.

In conclusion, filtering the X-ray beam can reduce beam hardening-induced cupping artifacts in bone-like materials at thicknesses relevant to typical µCT studies. Filtration does not necessarily require software based beam hardening corrections, but it does decrease contrast, increase the baseline noise, and decrease throughput. These artifacts do not significantly impact estimates of the mineral density in cortical bone, but they may be concerning for trabecular bone. Beam hardening induces less artifacts for morphology than densitometric measurements so, if an appropriate scan setup is used, the results can be meaningful.

References

1. Blake, G.M., and Fogelman, I. 2002. Methods and Clinical Issues in Bone Densitometry and Quantitative Ultrasonometry. In *Principles of Bone Biology, 2nd ed.* J.P. Bilezikian, L.G. Raisz, and G.A. Rodan, editors. San Diego: Academic Press. 1573-1585.
2. Genant, H.K., Faulkner, K.G., Gluer, C.C., and Engelke, K. 1993. Bone densitometry: current assessment. *Osteoporos Int* 3 Suppl 1:91-97.
3. Bolotin, H.H. 2007. DXA in vivo BMD methodology: An erroneous and misleading research and clinical gauge of bone mineral status, bone fragility, and bone remodelling. *Bone* 41:138-154.
4. Lochmuller, E.M., Lill, C.A., Kuhn, V., Schneider, E., and Eckstein, F. 2002. Radius bone strength in bending, compression, and falling and its correlation with clinical densitometry at multiple sites. *J Bone Miner Res* 17:1629-1638.
5. Martin, D.E., Severns, A.E., and Kabo, J.M. 2004. Determination of mechanical stiffness of bone by pQCT measurements: correlation with non-destructive mechanical four-point bending test data. *J Biomech* 37:1289-1293.
6. Brodt, M.D., Pelz, G.B., Taniguchi, J., and Silva, M.J. 2003. Accuracy of peripheral quantitative computed tomography (pQCT) for assessing area and density of mouse cortical bone. *Calcif Tissue Int* 73:411-418.
7. Schmidt, C., Priemel, M., Kohler, T., Weusten, A., Muller, R., Amling, M., and Eckstein, F. 2003. Precision and accuracy of peripheral quantitative computed tomography (pQCT) in the mouse skeleton compared with

histology and microcomputed tomography (microCT). *J Bone Miner Res* 18:1486-1496.
8. Kuhn, J.L., Goldstein, S.A., Choi, K., London, M., Feldkamp, L.A., and Matthews, L.S. 1989. Comparison of the trabecular and cortical tissue moduli from human iliac crests. *J Orthop Res* 7:876-884.
9. Barrett, J.F., and Keat, N. 2004. Artifacts in CT: recognition and avoidance. *Radiographics* 24:1679-1691.
10. Duerinckx, A.J., and Macovski, A. 1978. Polychromatic Streak Artifacts in Computed Tomography Images. *Journal of Computer Assisted Tomography* 2:481-487.
11. Joseph, P.M., and Spital, R.D. 1978. Method for Correcting Bone Induced Artifacts in Computed Tomography Scanners. *Journal of Computer Assisted Tomography* 2:100-108.
12. Alvarez, R.E., and Macovski, A. 1976. Energy-Selective Reconstructions in X-Ray Computerized Tomography. *Physics in Medicine and Biology* 21:733-744.
13. Remeysen, K., and Swennen, R. 2006. Beam hardening artifact reduction in microfocus computed tomography for improved quantitative coal characterization. *International Journal of Coal Geology* 67:101-111.
14. Yan, C.H., Whalen, R.T., Beaupre, G.S., Yen, S.Y., and Napel, S. 2000. Reconstruction algorithm for polychromatic CT imaging: Application to beam hardening correction. *Ieee Transactions on Medical Imaging* 19:1-11.
15. Hsieh, J., Molthen, R.C., Dawson, C.A., and Johnson, R.H. 2000. An iterative approach to the beam hardening correction in cone beam CT. *Medical Physics* 27:23-29.
16. Kijewski, P.K., and Bjarngard, B.E. 1978. Correction for beam hardening in computed tomography. *Medical Physics* 5:209-214.
17. Elbakri, I.A., and Fessler, J.A. 2002. Statistical image reconstruction for polyenergetic X-ray computed tomography. *Ieee Transactions on Medical Imaging* 21:89-99.
18. Elbakri, I.A., and Fessler, J.A. 2003. Segmentation-free statistical image reconstruction for polyenergetic x-ray computed tomography with experimental validation. *Physics in Medicine and Biology* 48:2453-2477.
19. Prevrhal, S. 2004. Beam Hardening Correction and Quantitative Micro-CT. In *Developments in X-ray tomography IV*. U. Bonse, editor. Denver, CO USA: SPIE. 152-161.
20. Fu, J., and Lu, H.N. 2006. Beam-hardening correction method based on original sinogram for X-CT. *Nuclear Instruments & Methods in Physics Research Section a-Accelerators Spectrometers Detectors and Associated Equipment* 556:379-385.
21. La Riviere, P.J., Bian, J., and Vargas, P.A. 2006. Penalized-likelihood sinogram restoration for computed tomography. *IEEE Trans Med Imaging* 25:1022-1036.
22. Burch, S.F. 2001. X-ray computerised tomography for quantitative measurement of density variations in materials. *Insight* 43:29-31.

23. Chen, C.Y., Chuang, K.S., Wu, J., Lin, H.R., and Li, M.J. 2001. Beam hardening correction for computed tomography images using a postreconstruction method and equivalent tissue concept. *Journal of Digital Imaging* 14:54-61.
24. de Paiva, R.F., Lynch, J., Rosenberg, E., and Bisiaux, M. 1998. A beam hardening correction for X-ray microtomography. *Ndt & E International* 31:17-22.
25. Kachelriess, M., Sourbelle, K., and Kalender, W.A. 2006. Empirical cupping correction: A first-order raw data precorrection for cone-beam computed tomography. *Medical Physics* 33:1269-1274.
26. Meagher, J.M., Mote, C.D., and Skinner, H.B. 1990. Ct Image Correction for Beam Hardening Using Simulated Projection Data. *Ieee Transactions on Nuclear Science* 37:1520-1524.
27. Fajardo, R.J., Cory, E., Patel, N.D., Nazarian, A., Laib, A., Manoharan, R.K., Schmitz, J.E., Desilva, J.M., Maclatchy, L.M., Snyder, B.D., et al. 2009. Specimen size and porosity can introduce error into muCT-based tissue mineral density measurements. *Bone* 44:176-184.
28. Mulder, L., Koolstra, J.H., and Van Eijden, T.M. 2004. Accuracy of microCT in the quantitative determination of the degree and distribution of mineralization in developing bone. *Acta Radiol* 45:769-777.
29. Postnov, A.A., Vinogradov, A.V., Van Dyck, D., Saveliev, S.V., and De Clerck, N.M. 2003. Quantitative analysis of bone mineral content by x-ray microtomography. *Physiological Measurement* 24:165-178.
30. Burghardt, A.J., Kazakia, G.J., Laib, A., and Majumdar, S. 2008. Quantitative assessment of bone tissue mineralization with polychromatic micro-computed tomography. *Calcif Tissue Int* 83:129-138.
31. Kazakia, G.J., Burghardt, A.J., Cheung, S., and Majumdar, S. 2008. Assessment of bone tissue mineralization by conventional x-ray microcomputed tomography: comparison with synchrotron radiation microcomputed tomography and ash measurements. *Med Phys* 35:3170-3179.
32. Nuzzo, S., Peyrin, F., Cloetens, P., and Baruchel, J. 2002. Quantification of the degree of mineralization of bone in three dimensions using synchrotron radiation microtomography. *Medical Physics* 29:2672-2681.
33. Kirby, B.J., Davis, J.R., Grant, J.A., and Morgan, M.J. 1997. Monochromatic microtomographic imaging of osteoporotic bone. *Physics in Medicine and Biology* 42:1375-1385.
34. Lopes, R.T., Costa, E.B., and de Jesus, E.F.O. 2000. Computed tomography with monochromatic bremsstrahlung radiation. *Applied Radiation and Isotopes* 53:665-671.
35. Brooks, R.A., and Dichiro, G. 1976. Beam Hardening in X-Ray Reconstructive Tomography. *Physics in Medicine and Biology* 21:390-398.
36. Kozloff, K.M. 2005. Influence of a collagen mutation of the mechanical nature of bone : governing factors in a disease model for osteogenesis imperfecta type IV. In *Biomedical Engineering*. Ann Arbor, MI: University of Michigan.

37. Bab, I., Hajbi-Yonissi, C., Gabet, Y., and Muller, R. 2007. *Micro-tomographic atlas of the mouse skeleton*. New York: Springer. viii, 205 p. pp.
38. Hankenson, K.D., Bain, S.D., Kyriakides, T.R., Smith, E.A., Goldstein, S.A., and Bornstein, P. 2000. Increased marrow-derived osteoprogenitor cells and endosteal bone formation in mice lacking thrombospondin 2. *J Bone Miner Res* 15:851-862.
39. Hankenson, K.D., Hormuzdi, S.G., Meganck, J.A., and Bornstein, P. 2005. Mice with a disruption of the thrombospondin 3 gene differ in geometric and biomechanical properties of bone and have accelerated development of the femoral head. *Mol Cell Biol* 25:5599-5606.
40. Holmen, S.L., Giambernardi, T.A., Zylstra, C.R., Buckner-Berghuis, B.D., Resau, J.H., Hess, J.F., Glatt, V., Bouxsein, M.L., Ai, M., Warman, M.L., et al. 2004. Decreased BMD and limb deformities in mice carrying mutations in both Lrp5 and Lrp6. *J Bone Miner Res* 19:2033-2040.
41. White, D.R. 1978. Tissue substitutes in experimental radiation physics. *Med Phys* 5:467-479.
42. Inc., G. 2009. Gammex 467 Tissue Characterization Phantom.
43. Tucker, D.M., Barnes, G.T., and Chakraborty, D.P. 1991. Semiempirical model for generating tungsten target x-ray spectra. *Med Phys* 18:211-218.
44. Feldkamp, L.A., Davis, L.C., and Kress, J.W. 1984. Practical cone-beam algorithm. *J Opt Soc Am A, Opt Image Sci Vis* 858:612-619.
45. Ramachandran, G.N., and Lakshminarayanan, A.V. 1971. 3-Dimensional reconstruction from radiographs and electron micrographs - application of convolutions instead of Fourier transforms. *Proc Natl Acad Sci U S A* 68:2236-2240.
46. Van de Casteele, E., Van Dyck, D., Sijbers, J., and Raman, E. 2002. An energy-based beam hardening model in tomography. *Physics in Medicine and Biology* 47:4181-4190.
47. Webb, A.G. 2003. *Introduction to Biomedical Imaging*: Wiley-IEEE Press.
48. Marxen, M., Thornton, M.M., Chiarot, C.B., Klement, G., Koprivnikar, J., Sled, J.G., and Henkelman, R.M. 2004. MicroCT scanner performance and considerations for vascular specimen imaging. *Med Phys* 31:305-313.
49. Parker, D.L. 1982. Optimal short scan convolution reconstruction for fanbeam CT. *Med Phys*:254-257.
50. Kohler, T., Beyeler, M., Webster, D., and Muller, R. 2005. Compartmental bone morphometry in the mouse femur: reproducibility and resolution dependence of microtomographic measurements. *Calcif Tissue Int* 77:281-290.
51. Nazarian, A., Snyder, B.D., Zurakowski, D., and Muller, R. 2008. Quantitative micro-computed tomography: a non-invasive method to assess equivalent bone mineral density. *Bone* 43:302-311.
52. Jennings, R.J. 1988. A Method for Comparing Beam-Hardening Filter Materials for Diagnostic-Radiology. *Medical Physics* 15:588-599.

53. Sandborg, M., Carlsson, C.A., and Carlsson, G.A. 1994. Shaping X-Ray-Spectra with Filters in X-Ray-Diagnostics. *Medical & Biological Engineering & Computing* 32:384-390.
54. Olejniczak, A.J., Tafforeau, P., Smith, T.M., Temming, H., and Hublin, J.J. 2007. Technical note: Compatibility of microtomographic imaging systems for dental measurements. *Am J Phys Anthropol*.
55. Bernhardt, R., Scharnweber, D., Muller, B., Thurner, P., Schliephake, H., Wyss, P., Beckmann, F., Goebbels, J., and Worch, H. 2004. Comparison of microfocus- and synchrotron X-ray tomography for the analysis of osteointegration around Ti6Al4V implants. *Eur Cell Mater* 7:42-51; discussion 51.
56. Shikhaliev, P.M. 2005. Beam hardening artefacts in computed tomography with photon counting, charge integrating and energy weighting detectors: a simulation study. *Physics in Medicine and Biology* 50:5813-5827.
57. Wesarg, S., Ebert, M., and Bortfeld, T. 2002. Parker weights revisited. *Med Phys* 29:372-378.
58. Kim, D.G., Christopherson, G.T., Dong, X.N., Fyhrie, D.P., and Yeni, Y.N. 2004. The effect of microcomputed tomography scanning and reconstruction voxel size on the accuracy of stereological measurements in human cancellous bone. *Bone* 35:1375-1382.
59. Muller, R., and Ruegsegger, P. 1997. Micro-Tomographic Imaging for the Nondestructive Evaluation of Trabecular Bone Architecture. In *Bone research in biomechanics*. G. Lowet, editor. Amsterdam ; Washington, D.C.: IOS Press. 61-79.
60. Peyrin, F., Salome, M., Cloetens, P., Laval-Jeantet, A.M., Ritman, E., and Ruegsegger, P. 1998. Micro-CT examinations of trabecular bone samples at different resolutions: 14, 7 and 2 micron level. *Technol Health Care* 6:391-401.
61. Hangartner, T.N., and Short, D.F. 2007. Accurate quantification of width and density of bone structures by computed tomography. *Medical Physics* 34:3777-3784.
62. Buie, H.R., Campbell, G.M., Klinck, R.J., MacNeil, J.A., and Boyd, S.K. 2007. Automatic segmentation of cortical and trabecular compartments based on a dual threshold technique for in vivo micro-CT bone analysis. *Bone* 41:505-515.
63. Chappard, D., Retailleau-Gaborit, N., Legrand, E., Basle, M.F., and Audran, M. 2005. Comparison insight bone measurements by histomorphometry and microCT. *J Bone Miner Res* 20:1177-1184.
64. Fajardo, R.J., Ryan, T.M., and Kappelman, J. 2002. Assessing the accuracy of high-resolution X-ray computed tomography of primate trabecular bone by comparisons with histological sections. *Am J Phys Anthropol* 118:1-10.
65. Kuhn, J.L., Goldstein, S.A., Feldkamp, L.A., Goulet, R.W., and Jesion, G. 1990. Evaluation of a microcomputed tomography system to study trabecular bone structure. *J Orthop Res* 8:833-842.

66. Thomsen, J.S., Laib, A., Koller, B., Prohaska, S., Mosekilde, L., and Gowin, W. 2005. Stereological measures of trabecular bone structure: comparison of 3D micro computed tomography with 2D histological sections in human proximal tibial bone biopsies. *J Microsc* 218:171-179.
67. Waarsing, J.H., Day, J.S., and Weinans, H. 2004. An improved segmentation method for in vivo microCT imaging. *J Bone Miner Res* 19:1640-1650.

Table 1: The source current and detector integration times used for the image acquisition protocols.

Filter Material	Flattener	Source Current (μA)	Integration Time (ms)
None	Y	65	1600
	N	50	1600
0.254 mm Al	Y	80	1600
	N	70	1600
0.508 mm Al	Y	80	1800
	N	80	1600
1.016 mm Al	Y	80	2300
	N	80	2100
0.254 mm Al & 0. 254 mm Cu	Y	80	6000
	N	80	5400

Table 2: Percentage of beam hardening artifacts for the SB3 phantom. Shaded fields indicate areas where the mean grayscale difference is greater than the noise level for the image, indicating that significant beam hardening artifacts occurred.

Phantom Material	Test Condition	Filtration	Phantom Thickness (mm)										
			3.048	3.924	4.801	5.677	6.553	7.430	8.306	9.182	10.058	10.935	11.811
SB3	With Flattener	None	3.4%	6.5%	9.3%	8.9%	8.8%	10.3%	12.2%	12.7%	12.3%	13.1%	14.5%
		0.254 mm Al	1.2%	4.0%	7.5%	7.9%	9.1%	11.7%	13.7%	13.5%	14.3%	15.3%	16.1%
		0.508 mm Al	1.4%	3.8%	7.3%	7.0%	7.5%	10.4%	11.4%	12.7%	13.9%	15.1%	16.7%
		1.016 mm Al	-1.9%	0.1%	3.5%	3.5%	4.5%	6.7%	8.3%	9.4%	10.2%	11.9%	10.8%
		0.254 mm Al & 0.254 mm Cu	-7.1%	-7.3%	-4.6%	-5.5%	-5.0%	-3.6%	-2.1%	-1.4%	-0.8%	1.0%	0.7%
	Without Flattener	None	5.4%	9.0%	12.5%	12.9%	14.4%	18.5%	21.0%	23.2%	25.8%	28.1%	30.6%
		0.254 mm Al	5.0%	6.8%	10.8%	10.2%	11.1%	14.5%	17.3%	18.8%	20.7%	21.9%	24.3%
		0.508 mm Al	1.5%	4.3%	8.6%	8.3%	9.5%	12.5%	14.3%	16.5%	18.0%	19.0%	21.6%
		1.016 mm Al	-2.3%	0.6%	4.6%	4.6%	5.7%	8.2%	10.0%	11.7%	12.8%	14.3%	15.3%
		0.254 mm Al & 0.254 mm Cu	-9.0%	-8.8%	-5.5%	-6.0%	-6.3%	-3.2%	-2.2%	-1.5%	-0.9%	0.5%	2.0%

Table 3: Percentage of beam hardening artifacts for the CB2-50% phantom. Shaded fields indicate areas where the mean grayscale difference is greater than the noise level for the image, indicating that significant beam hardening artifacts occurred.

Phantom Material	Test Condition	Filtration	Phantom Thickness (mm)										
			3.048	3.924	4.801	5.677	6.553	7.430	8.306	9.182	10.058	10.935	11.811
CB2-50%	With Flattener	None	-0.9%	2.6%	5.6%	5.2%	5.1%	6.6%	7.9%	7.9%	9.3%	8.9%	8.3%
		0.254 mm Al	-0.1%	1.8%	5.5%	5.6%	5.3%	7.5%	9.7%	10.7%	11.1%	12.4%	14.3%
		0.508 mm Al	-2.1%	0.1%	3.8%	5.0%	4.9%	8.0%	8.8%	9.9%	11.0%	12.8%	13.6%
		1.016 mm Al	-3.5%	-2.1%	1.1%	1.1%	2.4%	3.6%	5.4%	6.4%	7.5%	9.0%	10.5%
		0.254 mm Al & 0.254 mm Cu	-10.5%	-8.3%	-5.3%	-6.5%	-6.1%	-6.0%	-6.0%	-3.8%	-2.2%	-1.5%	-0.5%
	Without Flattener	None	5.0%	7.8%	12.2%	12.3%	14.4%	18.1%	20.7%	23.6%	26.0%	30.7%	32.6%
		0.254 mm Al	1.8%	4.8%	7.8%	8.3%	9.4%	12.2%	15.9%	17.4%	19.6%	22.5%	25.2%
		0.508 mm Al	-0.3%	1.9%	5.3%	6.0%	6.9%	9.9%	12.8%	14.8%	16.3%	19.1%	20.9%
		1.016 mm Al	-2.8%	-1.6%	2.2%	2.8%	3.2%	6.5%	8.1%	9.6%	11.1%	13.5%	14.8%
		0.254 mm Al & 0.254 mm Cu	-10.1%	-7.7%	-7.2%	-6.6%	-6.7%	-5.0%	-4.5%	-3.2%	-1.8%	-0.6%	-0.8%

Table 4: Raw HU differences that were deemed artifacts for the SB3 phantom. Shaded fields indicate areas where the mean grayscale difference is greater than the noise level for the image, indicating that significant beam hardening artifacts occurred.

Phantom Material	Test Condition	Filtration	Phantom Thickness (mm)										
			3.048	3.924	4.801	5.677	6.553	7.43	8.306	9.182	10.058	10.935	11.811
SB3	With Flattener	None	144.8	260.7	364.5	337.6	329.0	375.1	432.5	442.6	419.0	442.5	469.8
		0.254 mm Al	58.4	159.3	290.0	297.9	338.2	427.1	496.8	473.7	492.5	524.6	530.9
		0.508 mm Al	59.3	149.4	275.4	261.9	272.8	375.5	405.1	442.5	479.3	513.2	555.5
		1.016 mm Al	-59.7	11.5	131.3	130.2	163.3	236.7	290.9	326.7	352.1	407.8	357.2
		0.254 mm Al & 0.254 mm Cu	-167.7	-167.1	-104.5	-129.7	-117.4	-81.4	-41.6	-24.6	-9.0	38.3	30.4
	Without Flattener	None	206.6	329.3	453.2	458.0	503.2	645.3	724.9	791.8	877.5	971.2	1029.9
		0.254 mm Al	192.7	250.6	393.8	367.0	391.6	506.4	600.8	639.9	703.0	731.3	803.7
		0.508 mm Al	66.6	163.4	314.4	302.3	339.5	439.8	496.5	573.5	618.4	656.9	726.9
		1.016 mm Al	-69.6	28.9	168.1	166.9	204.6	291.1	353.3	407.6	448.3	498.6	519.7
		0.254 mm Al & 0.254 mm Cu	-215.7	-207.7	-128.0	-144.8	-152.4	-74.8	-46.8	-28.0	-12.6	23.5	63.2

Table 5: Raw HU differences that were deemed artifacts for the CB2-50% phantom. Shaded fields indicate areas where the mean grayscale difference is greater than the noise level for the image, indicating that significant beam hardening artifacts occurred.

Phantom Material	Test Condition	Filtration	Phantom Thickness (mm)										
			3.048	3.924	4.801	5.677	6.553	7.43	8.306	9.182	10.058	10.935	11.811
CB2-50%	With Flattener	None	-17.3	81.0	161.5	146.5	142.6	180.0	209.0	206.7	236.1	222.1	202.0
		0.254 mm Al	6.9	53.8	150.6	151.1	140.4	195.5	249.6	271.7	278.5	308.4	345.0
		0.508 mm Al	-48.2	11.2	104.3	131.1	128.7	206.2	220.5	245.4	270.7	312.0	324.0
		1.016 mm Al	-75.9	-38.7	36.2	34.9	66.8	98.1	135.4	159.3	185.1	220.3	250.5
		0.254 mm Al & 0.254 mm Cu	-161.7	-121.2	-74.4	-94.4	-88.5	-84.3	-85.1	-50.4	-21.8	-8.3	9.7
	Without Flattener	None	128.45	190.26	293.92	297.41	344.18	431.74	495.74	564.92	623.82	731.38	789.40
		0.254 mm Al	55.46	130.39	205.16	217.20	242.44	314.15	405.52	439.82	494.98	569.66	628.35
		0.508 mm Al	-0.07	55.68	141.57	158.91	176.76	252.26	324.71	373.34	409.92	480.48	517.54
		1.016 mm Al	-58.82	-27.54	62.42	75.57	84.98	165.70	202.77	237.71	275.48	333.26	359.54
		0.254 mm Al & 0.254 mm Cu	-147.42	-111.44	-106.98	-97.68	-101.19	-71.20	-61.93	-41.82	-16.45	4.74	2.15

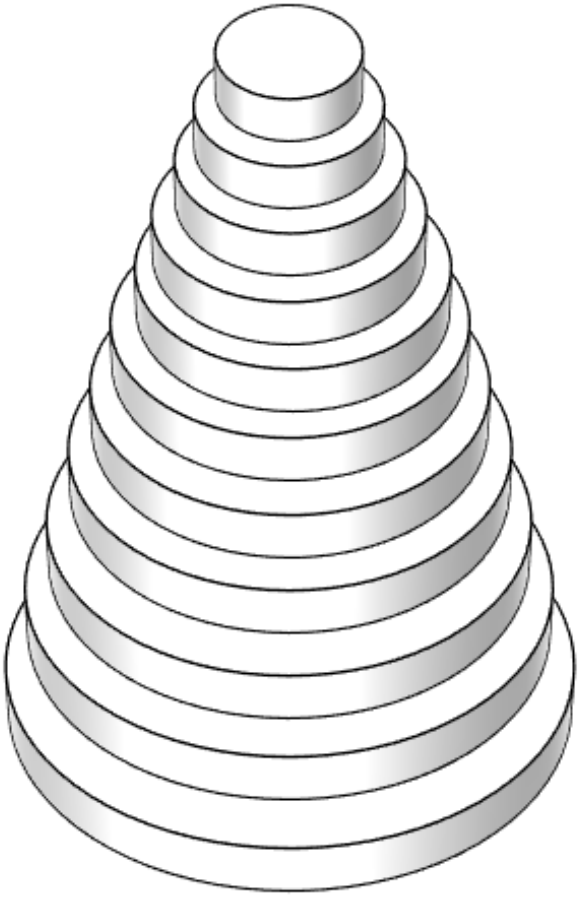

Figure 1:Schematic of the phantom design for beam hardening assessments.

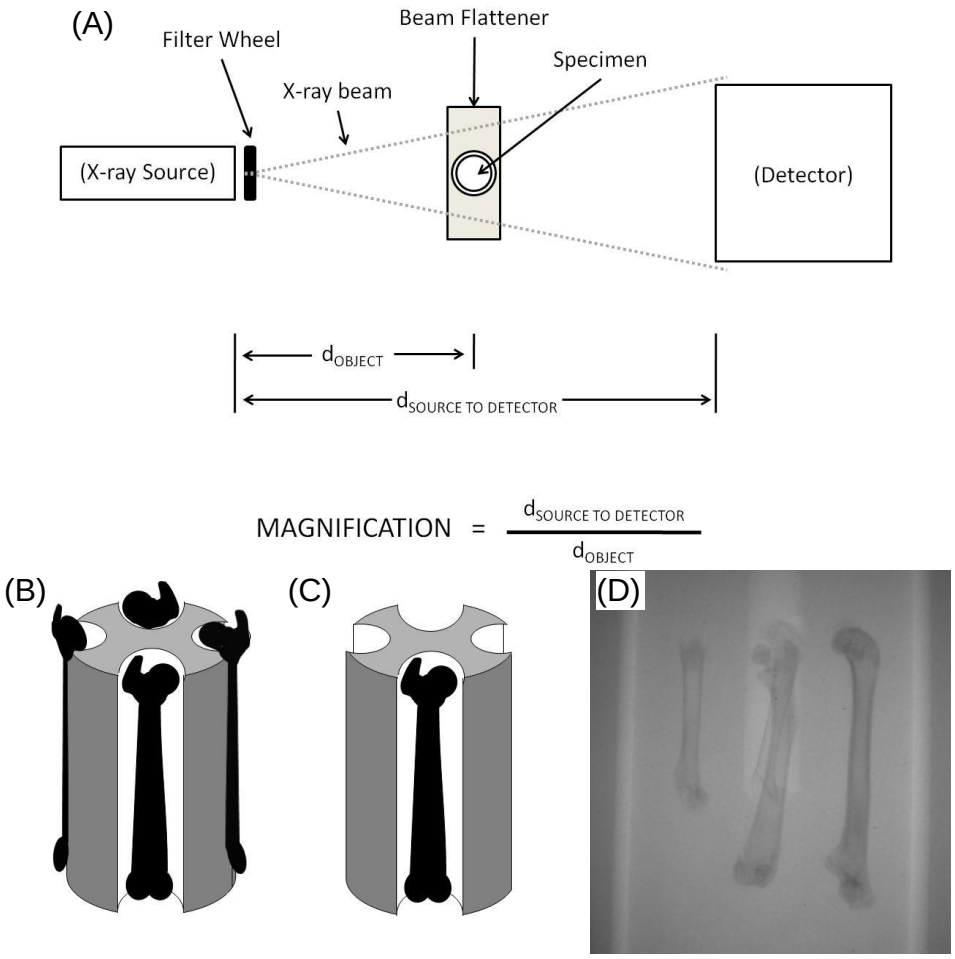

Figure 2: Scan setups used for the scanner in the murine phenotyping study.

This figure shows (A) a top down view of the scanner setup including the major components. Note the filter immediately after the source and the flattener around the specimen. The specimen tube can be used to hold (B) four bones simultaneously or (C) one bone at a time away from the center of rotation. As shown in the representative projection image (D), when more than one bone is placed in the holder X-rays will pass through multiple specimens.

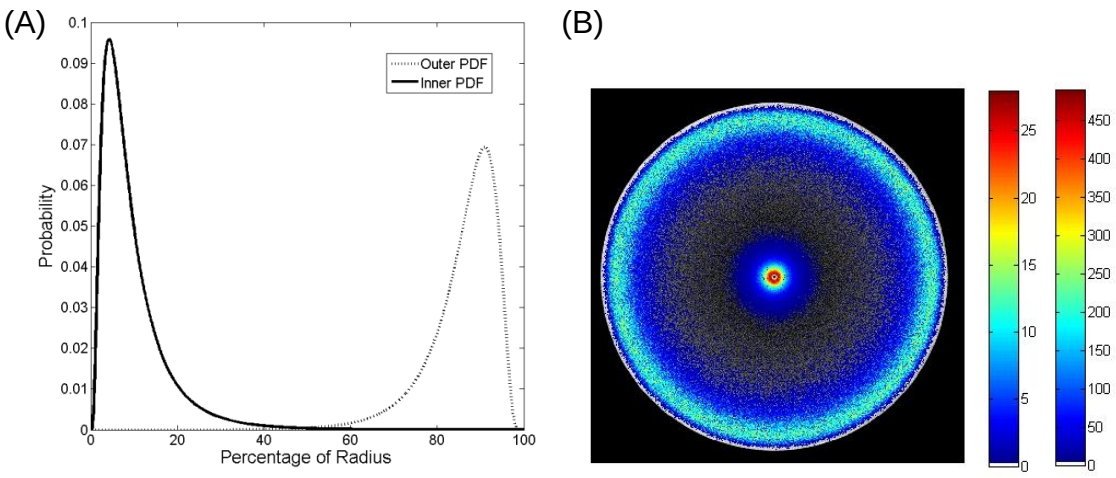

Figure 3: Sampling distributions used to assess voxel grayscale differences.

In (A) the probability density functions of the lognormal functions are shown, demonstrating the distributions that were sampled to represent the center of the phantom (black) and the outer edge of the phantom (gray). In (B), a representative example of this sampling process is shown. The color bar at the left shows the number of voxels for the distribution at the edge of the phantom. The color bar at the right shows the number of voxels for the distribution at the center of the phantom.

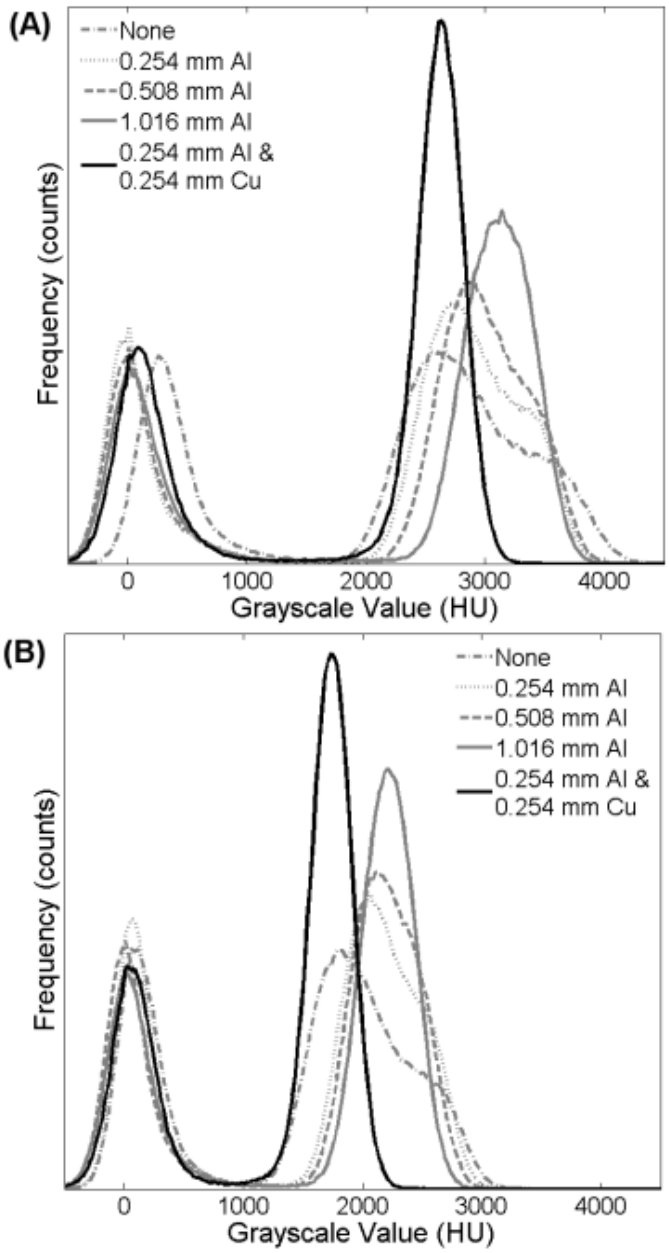

Figure 4: Histograms showing the decrease in contrast that occurs as a result of beam filtration.

Histograms for Tier 11 in the phantoms made from (A) SB3 and (B) CB2-50% when scanned without the flattener. The peak centered around the value of 0 represents water in the background of the image.

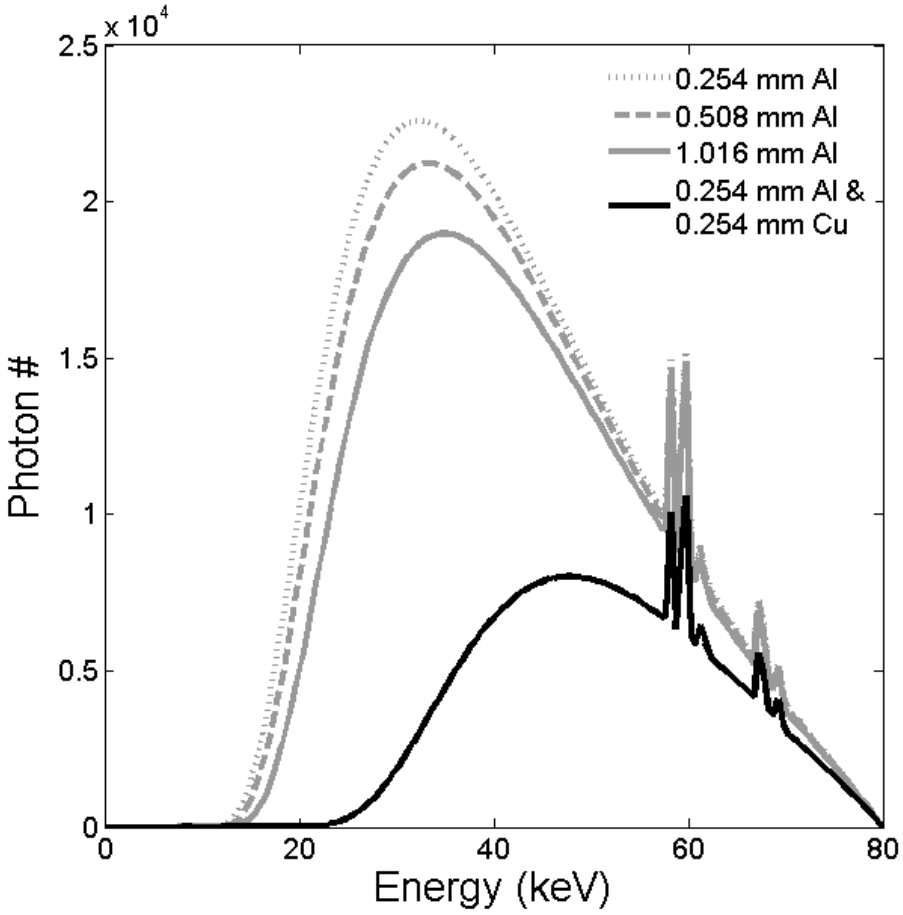

Figure 5: X-ray spectral comparison.

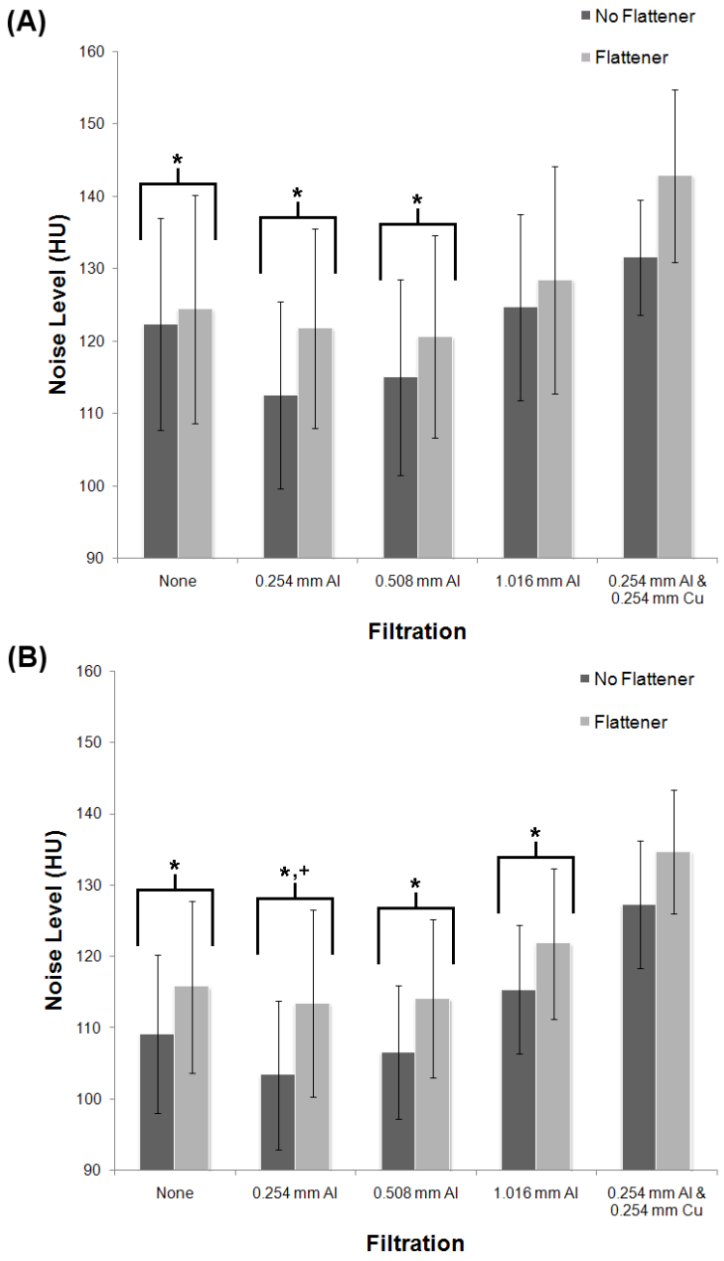

Figure 6: Noise levels increased with extensive beam filtration and use of a beam flattener.

Mean noise levels for water adjacent to the tiered phantoms made from (A) SB3 and (B) CB2-50%. * indicates significance in comparison to the the 0.254 mm Al/0.254 mm Cu filter and + indicates significance in comparison to the 1.016 mm Al filter. Data are presented as the mean ± one standard deviation.

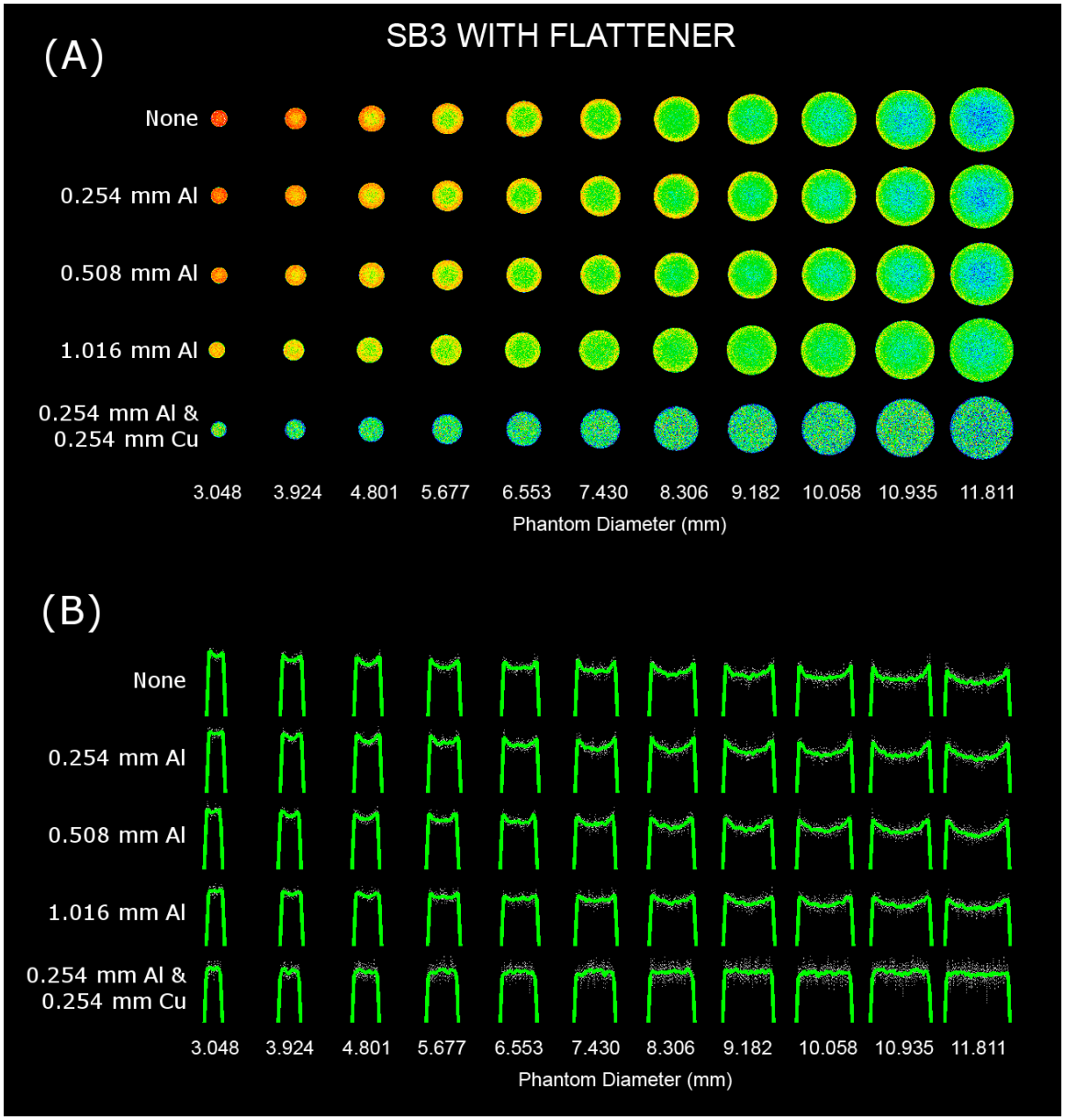

Figure 7: Visualization of the beam hardening artifacts for the SB3 phantom when scanned with the flattener.

In a colormapped version for each of the images represents the grayscale values,(A) a change in the color pattern indicates an apparent change in the voxel HU value between the inside and outsie. This can also be seen using a line plot across the center of each image (B).

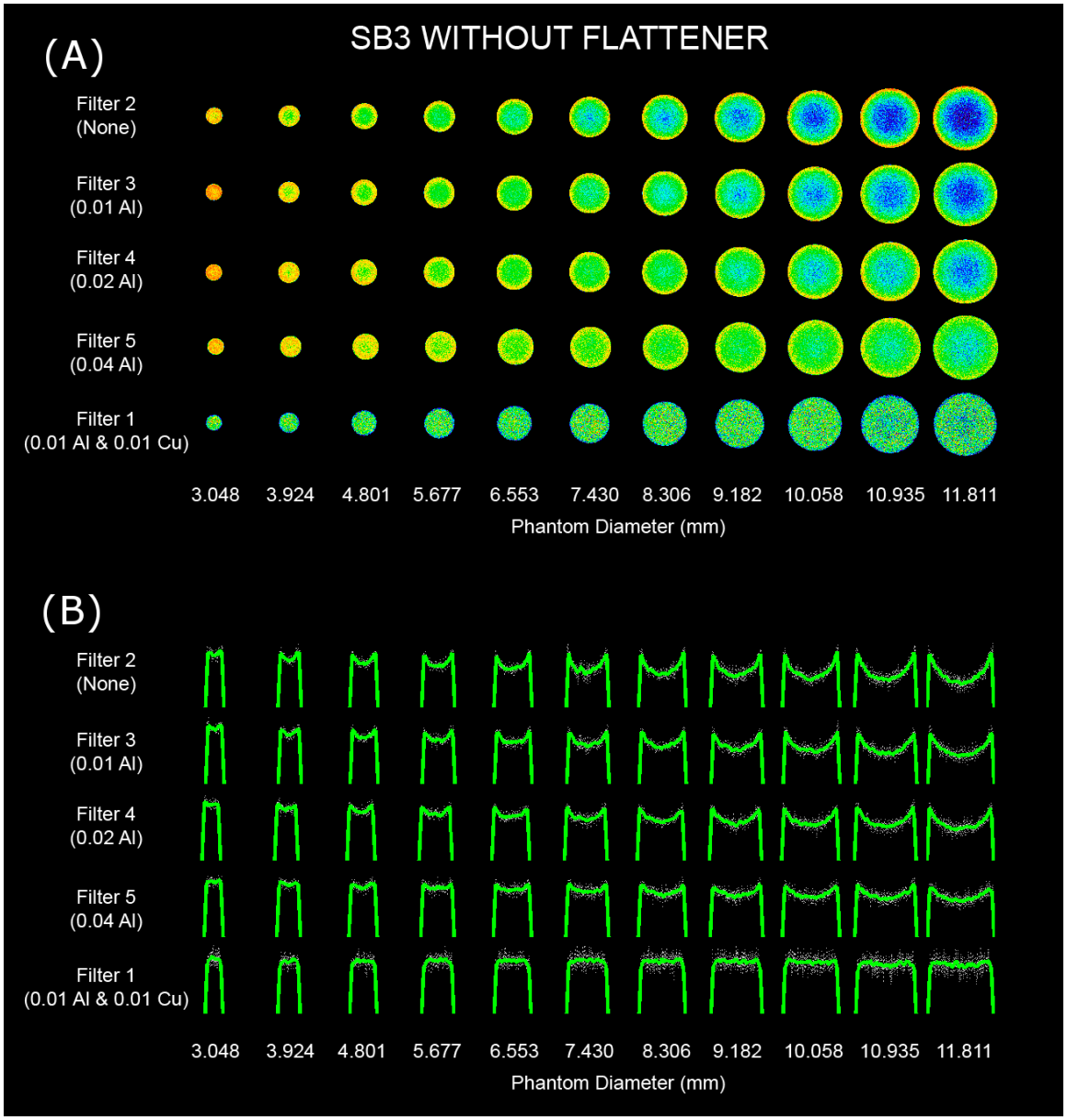

Figure 8: Visualization of the beam hardening artifacts for the SB3 phantom when scanned without the flattener.

In a colormapped version for each of the images represents the grayscale values,(A) a change in the color pattern indicates an apparent change in the voxel HU value between the inside and outsie. This can also be seen using a line plot across the center of each image (B).

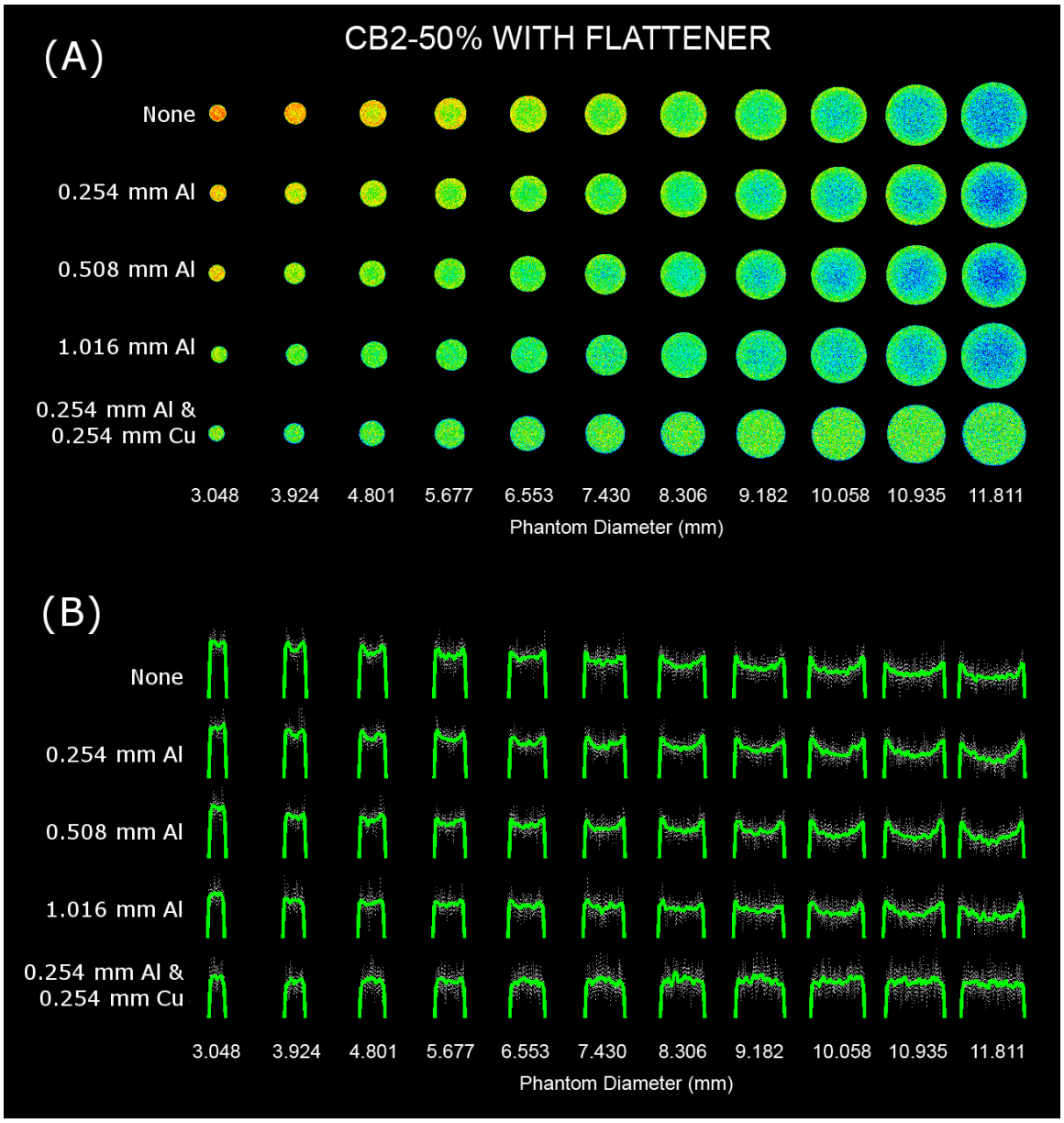

Figure 9: Visualization of the beam hardening artifacts for the CB2-50%phantom when scanned with the flattener.

In a colormapped version for each of the images represents the grayscale values,(A) a change in the color pattern indicates an apparent change in the voxel HU value between the inside and outsie. This can also be seen using a line plot across the center of each image (B).

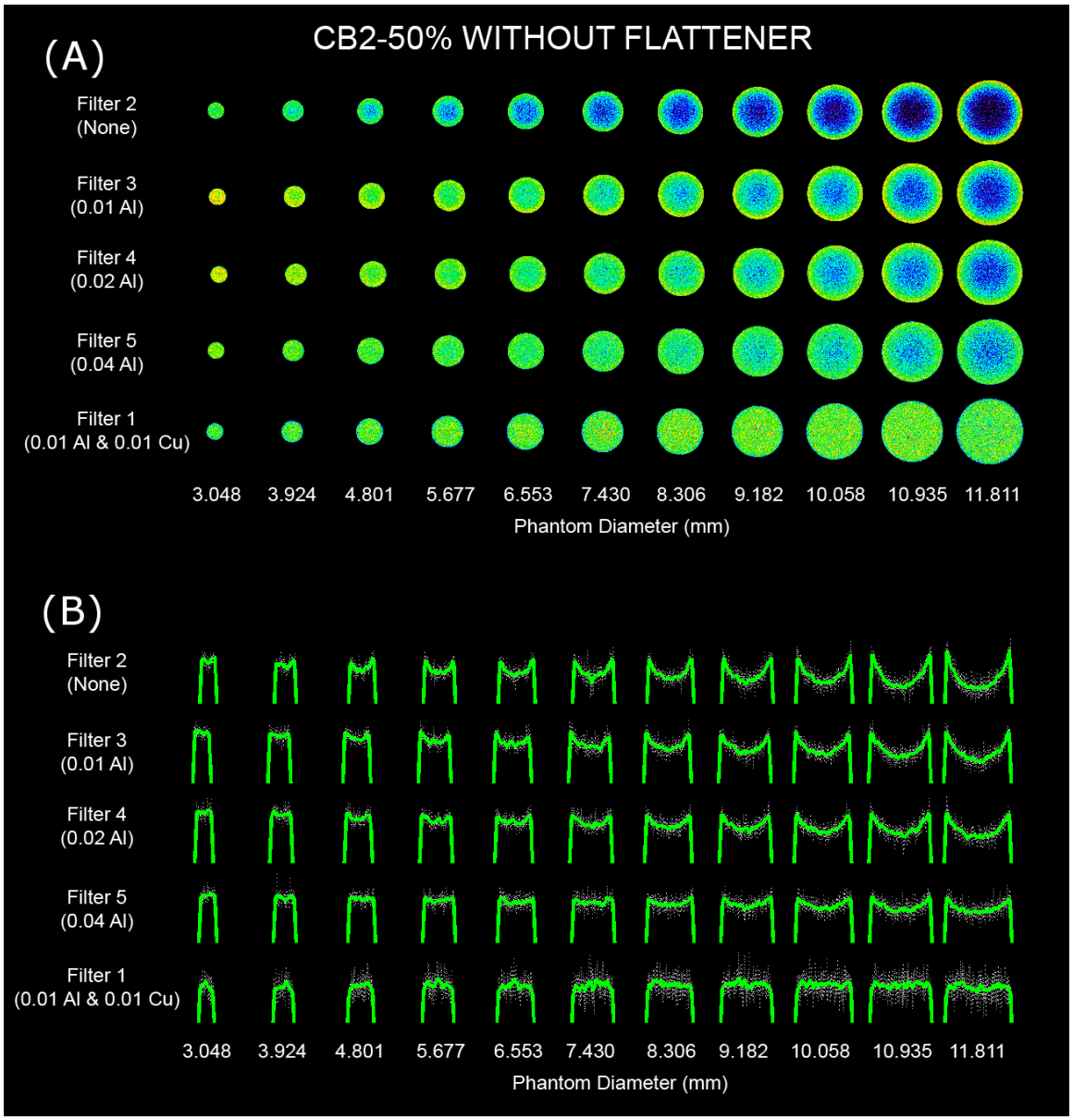

Figure 10: Visualization of the beam hardening artifacts for the CB2-50% phantom when scanned without the flattener.

In a colormapped version for each of the images represents the grayscale values,(A) a change in the color pattern indicates an apparent change in the voxel HU value between the inside and outsie. This can also be seen using a line plot across the center of each image (B).

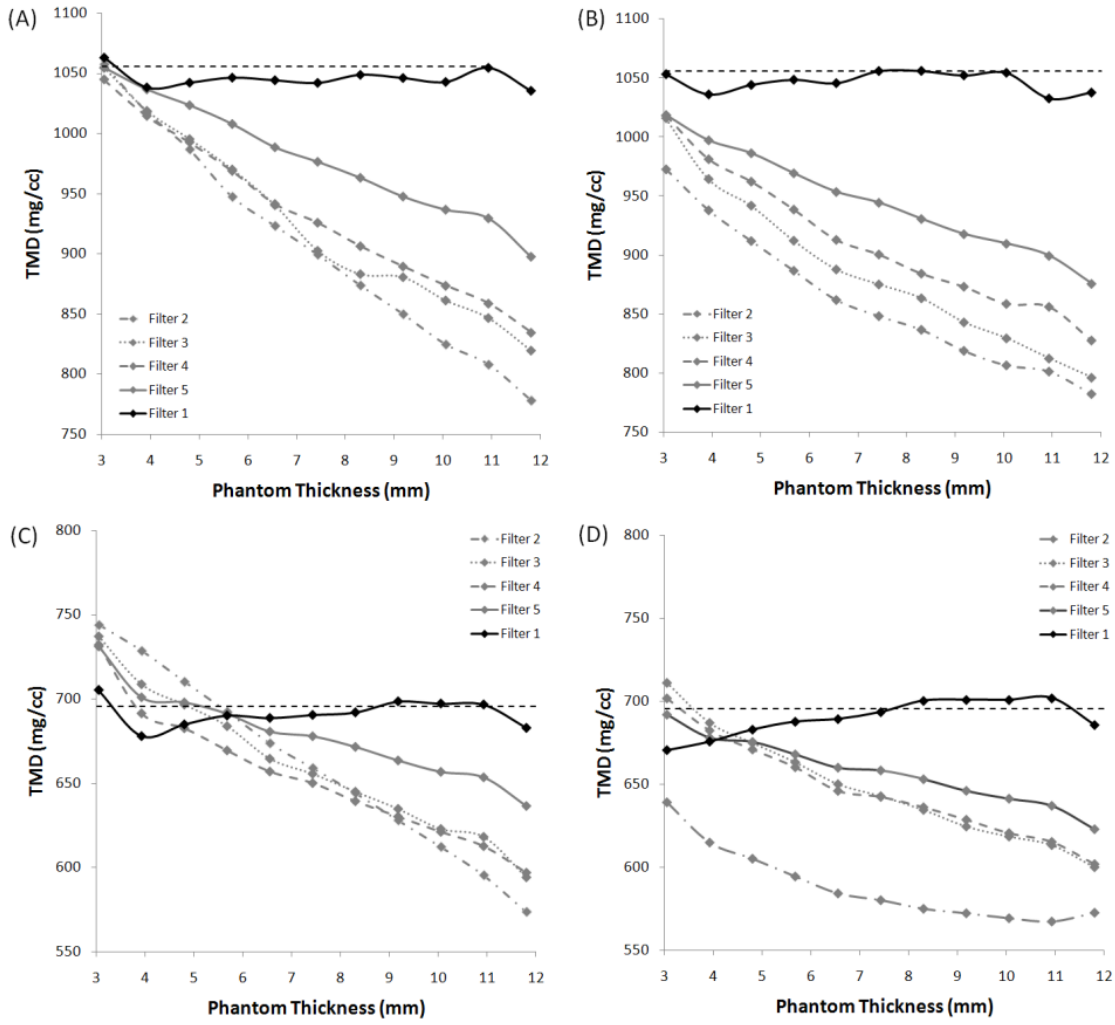

Figure 11: The measured tissue mineral density decreases with specimen thickness due to beam hardening artifacts.

Results of the TMD quantification for (A) the SB3 phantom scanned with the flattener, (B) the SB3 phantom scanned without the flattener, (C) the CB2-50% phantom scanned with the flattener, and (D) the CB2-50% phantom without the flattener. The theoretical 'ideal' value for the TMD of each material is superimposed as a dashed line.

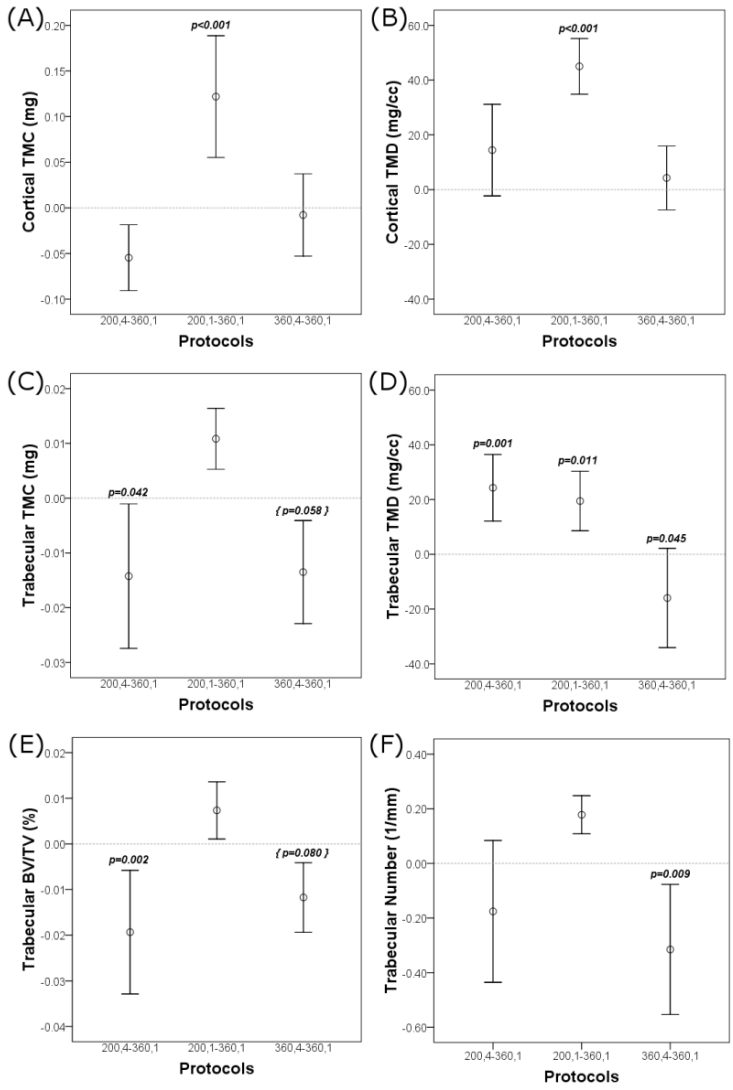

Figure 12: Impact of scan setup on bone densitometry and trabecular morphology measurements.

Comparisons of measurements on murine cortical bone for the (A) diaphyseal cortical TMC (B) diaphyseal cortical TMD (C) metaphyseal trabecular TMC, (D) metaphyseal trabecular TMD (E) trabecualar bone volume fraction and (F) trabecular number. The results are presented as 95% CI of paired comparisons to the scanning condition where each bone was scanned individually over 360°. An asterisk indicates a statistically significant difference ($p<0.05$ unless indicated).

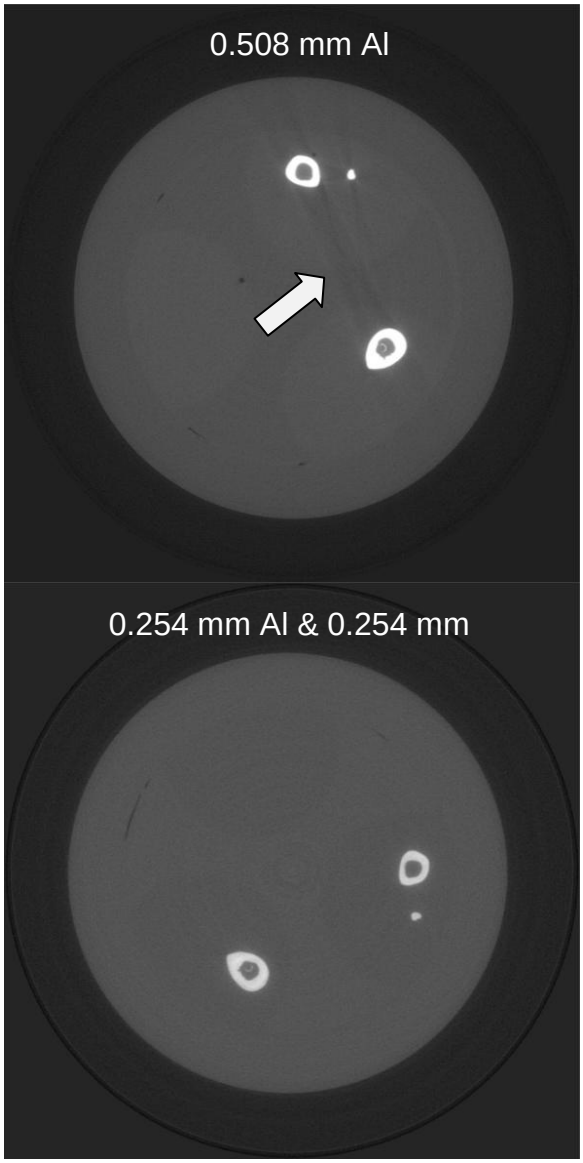

Figure 13: Beam hardening associated streaks can occur when scanning multiple mouse bones.

Two murine tibiae were scanned. Streaks between the two bones when we scanned with a 0.508 mm Al filter (top) that disappeared when they were rescanned the same bones using the 0.254 mm Al/0.254 mm Cu filter (bottom).

CHAPTER 3: THE EFFECTS OF ALENDRONATE ON FRACTURE HEALING IN THE BRTL/+ MOUSE MODEL OF OSTEOGENESIS IMPERFECTA

Introduction

Osteogenesis Imperfecta (OI) is a genetic disease that results in a high incidence of fractures during childhood and adolescence. Most of the mutations that cause OI are dominant and affect the genes encoding type I collagen,[1] although the genes CRTAP and LEPRE1 have recently been linked to recessive inheritance.[2] The exact relationships between specific genetic mutations and the phenotypic alterations have been elusive, although mutations which affect the major ligand binding regions seem to be more severe.[1] In mild and moderate forms of OI, these mutations can cause a decrease in the amount of collagen and/or a structurally abnormal type I collagen molecules. Irrespective of the specific mutations and molecular affects, the major problem for OI patients is skeletal fragility. There are some case reports of hypertrophic or hyperplastic callus formation in OI patients (for examples see [3,4]), and one report indicated delayed healing in almost 30% of patients.[5] However, it is generally thought that fractures in OI patients heal normally.[6]

Several controlled clinical studies have utilized bisphosphonates in an effort to prevent or reduce the number of fractures in OI patients.[7-10] These studies all show improvements in DXA based measurements and, in the three reporting fracture rates, a decrease in fracture risk. However, fractures still occurred in patients receiving treatment. This reduction in fracture risk occurs because bisphosphonates increase bone mass by mechanisms involving both osteoblasts and osteoclasts.[11] Bisphosphonates have a high affinity for bone mineral and, in early assessment of alendronate, were predicted to have a half life of over 10 years.[12]. The amount of bisphosphonate retained depends on the mechanism of delivery,[13] and the rate of bone turnover. Osteoporosis patients with relatively low turnover rates may not need to continue treatment for longer than five years.[14] In pediatric patients, who generally have higher metabolic rates, pamidronate has been detected in urine up to 8 years after cessation of treatment.[15] In one extreme case, 6 ½ years after the cessation of pamidronate there were still noticeable radiographic abnormalities and a subsequent fracture did not heal after 2 years.[16] This has led to caution in treating OI patients with bisphosphonates.[17]

This long term retention has led to a number of studies investigating fracture healing with bisphosphonates and anti-resorptives in both adult and pediatric populations. One randomized, double-blind, placebo-controlled trial with zoledronic acid infusions following a hip fracture did not show an increased risk for delayed union.[18] Similarly, in pediatric OI patients, bisphosphonate treatment is not usually associated with altered fracture healing although

intravenous pamidronate treatments may lead to delayed osteotomy healing.[19,20]

These important clinical studies are limited in their ability to understand ultrastructural changes. Therefore, there has been substantial interest in using animal models to understand how bisphosphonates impact fracture healing.[21-33] Early studies with non-nitrogen containing bisphosphonates indicate that high doses can lead to non-union,[28] and there may not be any effect on the callus biomechanical properties.[27,31] These effects are quite different with the nitrogenous bisphosphonates such as alendronate, zoledronic acid, incandronate and pamidronate. Zoledronic acid may not affect the rate or pattern of endochondral ossification.[32] Later in the healing process, the results generally indicate an increase in callus size and structural biomechanical changes, although the specifics depend on the particular bisphosphonate chosen, dose, delivery method, and timepoint of healing.[21,22,24-26,30,32,33] However, only three of these studies address the question about how fracture healing would be affected if bisphosphonates are present in the skeleton prior to fracture.[30,33,34] This distinction is important given the residence time of bisphosphonates in the skeleton.

In light of these concerns, and in an effort to obtain more fundamental information about how bisphosphonates affect fracture healing in OI, we performed a controlled fracture healing experiment with alendronate treatment using the Brtl/+ mouse model of OI. This knock-in model was created to mimic a clinical patient with a glycine substitution mutation, shows the same small size

and skeletal fragility that are clinical hallmarks of OI, and responds to alendronate therapy in a similar fashion to clinical patients.[35-38] It remains unclear if bisphosphonate treatment should be halted at the time of fracture or continued during healing in OI, so both treatment courses were examined. Growing mice were used because many of the affected pediatric patients will be growing at the time of fracture, and four timepoints were examined because of the dynamic nature of fracture healing. The purposes were to investigate fracture healing in the Brtl/+ mouse and to investigate how the presence of alendronate in the bone before fracture and during fracture healing impact the regenerating tissue.

Materials and Methods

Study Design

Male Brtl/+ mice, the progeny of Brtl/Brtl and WT parents, and male WT mice were enrolled into the study at 2 weeks (2w) of age. The breeding scheme primarily utilized intercrosses, but a backcross was occasionally performed as well. Upon enrollment, the mice were randomly assigned to receive one of three alendronate treatment protocols and be euthanized at one of four fracture healing timepoints (Figure 14). The alendronate treatment protocols were (1) no treatment, (2) treatment only before the fracture or (3) treatment before and after fracture. All mice were weighed once weekly and, when needed, a 0.219 μg/g subcutaneous injection of alendronate (Sigma Aldrich) was administered. This dose is based on a previous study indicating an effect comparable to clinical

therapy in the Brtl/+ mouse.[38] At 8 weeks of age, an intramedullary pin was inserted in one randomly chosen tibia and a fracture was created using a guillotine device and the limb was stabilized using a tape splint as previously described.[39] Animals received a buprenorphine injection pre-operatively to alleviate pain. A radiograph was taken at the time of fracture to categorize the fractures as simple, wedge, or complex using the classification scheme accepted by the Orthopaedic Trauma Association.[40] The animals then healed for 1, 2, 3 or 5 weeks after fracture to capture the phases of fracture healing that encompass the initial callus formation, bony formation, bridged calluses and early remodeling. The tibiae were harvested, wrapped in saline soaked gauze, and stored at -20 °C until further testing. All experiments were performed under approval of the University of Michigan IACUC.

μCT

The tibiae were thawed and scanned using a commercially available μCT system (eXplore Locus SP, GE Healthcare Pre-clinical Imaging, London, ONT) using a source voltage of 80 kVp, a source current of 80 μA, 2x2 detector binning and an exposure time of 1600 ms. A 0.5 mm aluminum filter and beam flattener were used to minimize beam hardening artifacts.[41] The raw data were corrected with bright and dark pixel corrections and a sinogram based filter and then reconstructed using a Feldkamp cone beam backprojection algorithm to obtain images with 18 μm voxels. In the reconstructed images, the callus volume, bone volume fraction (BVF) and tissue mineral density (TMD) of bone in the

callus and residual cortical bone were measured (MicroView 2.2, GE Healthcare Preclinical Imaging) using a segmentation approach very similar to a previously published technique.[39] Briefly, a spline based semi-automatic segmentation was used to segment the outer callus boundary. A second spline based segmentation in combination with a threshold confined region growing procedure was used to select the cortical bone. A Boolean operation was then performed on these two segmentations to create a region which only included bone in the callus. This region also included the intramedullary space because healing bone was present in the marrow cavity as well.

Biomechanical Testing

A randomly assigned subset of the fractured tibiae and their contralateral (intact) controls were tested in torsion as previously described.[39] Briefly, the specimens were potted using a low melting temperature metal alloy. This potting material was chosen instead of polymethylmethacrylate (PMMA) because it generates much less heat and sets up in less than one minute, allowing high throughput testing without causing heat induced damage in the ends of the bone near the potting material. The potted bone was then mounted in a custom torsion tester, wetted with saline, and tested in external rotation at 0.5°/s until failure using a custom LabView program to run a custom miniature torsion tester. Using a MATLAB script, the raw data were filtered and the stiffness, angular displacement at failure, torque at failure and the energy to failure were measured.

Quantitative Histology

A subset of the fractured tibia was fixed, decalcified, embedded, sectioned. The slides were then stained using (1) Safranin-O, Fast Green and Hematoxylin to assess cartilage, (2) tartrate resistant acid phosphatase (387A, Sigma Aldrich, St. Louis, MO) to assess osteoclasts or (3) picrosirius red for subsequent collagen analyses.

To analyze the Safranin-O stained slides, a custom ImageJ macro based on a color deconvolution technique was used to separate the Safranin-O component from the fast green and hematoxylin components.[42] This macro was implemented to assess both the amount of cartilage within the callus tissue and, because of an earlier report indicating additional cartilage retention in healing bone with zoledronic acid treatment,[43] the amount of cartilage within trabeculated bone of the callus. Slides from mice which healed for 1w, 2w, 3w and 5w were examined.

Two and six month old Brtl/+ mice have an increased number of osteoclasts and osteoclast surface per bone surface,[37] and alendronate works in part by affecting osteoclasts.[11] Since remodeling is actively occurring after 5w of fracture healing, TRAP analyses were performed on fractured tibiae from mice which healed for 5w. Only the outer callus boundary was examined because the μCT data indicated a change in callus volume between 3w and 5w (Figure 17), implying that remodeling would be occurring at the outer callus boundary. The number of osteoclasts per bone surface (OcN/BS) and the length

of TRAP positive osteoclast area on this surface per bone surface (OcS/BS) were measured on both the anterior and posterior sides of the callus using commercially available software. (BioQuant, Nashville, TN)

To analyze the picrosirius red stained slides, a polarized light method was implemented based on previously published techniques.[44,45] Briefly, a rotating stage was placed on a standard light microscope (Olympus BX-51). A linear polarizer between the light source and stage was crossed with a linearly oriented analyzer between the objective and camera. The section was placed on the stage, defining 0 deg. to align with the longitudinal axis of the bone. The stage was then rotated in increments of 5 or 10 deg. and images were captured at each stage rotation. These images were then imported into MATLAB and, using a custom script combined with the ImageJ TurboReg plugin, the images for each position of the rotation stage were registered. This facilitated analysis of the polarized light images on a pixel by pixel basis. These images were then segmented and thresholded to analyze the trabeculated bone of the callus separately from the residual cortical bone. The parallelism index (PI) was calculated for residual cortical bone and the trabeculated bone of the healing callus.[44] Polarized light analysis was only performed on 5w animals without treatment to investigate the differences in healing between the genotypes as indicated by biomechanical data.

Raman Microspectroscopy

All mice were sacrificed 3w after fracture creation, and the tibiae were excised and stored frozen for Raman analysis. To acquire spectra, the tibia were thawed, placed in a Petri dish, and kept moist with PBS while being illuminated through a 20x 0.75NA objective with 150 mW of 785 nm laser light in a 7x100 µm line profile. Ten separate spectra were acquired from the central portion of the callus (for fractured tibiae) or tibial mid-diaphysis (for contralateral intact control limbs) to account for variation in the tissue. A multiple step correction process was applied on a pixel by pixel basis to each spectral image to account for the relative transmission efficiency as a function of wavelength in the spectra due to the dichroic filter used to prevent incident light from impacting the scatter measurements.[46] The preprocessing routine also included an image rotation of 0.1185° to account for misalignment in the system. Spectra of neon and Teflon were used to determine the Raman shift axis on a daily basis. This calibration was used to clip the spectral data from approximately 615 to 1740 cm^{-1} to prevent extraneous data from biasing the subsequent spectral baselining technique that was performed using a 2nd degree polynomial in a custom implementation of the GIFTS method.[47]

All spectra were normalized to the height of the phenylalanine ring (~1002 cm^-1) because this peak height should be relatively independent of the experimental changes. Four separate outcome measurements were made. Crystallinity was measured as the inverse full width at half height of the 960 cm-1

peak.[48] The carbonate to phosphate ratio was calculated as the ratio of band areas for the 1070 cm^{-1} to 960 cm^{-1} peak.[49] The cross-linking ratio was calculated in the Amide I band by applying a five peak fit (1630, 1645, 1660, 1675 and 1690 cm^{-1}) and measuring the ratio of the area under the 1660 band to the area under the 1690 band. This metric, extended from an FTIR based technique,[50] has been utilized previously to estimate the degree of collagen cross-linking.[49,51] Mineral to matrix ratios were estimated using three different metrics. The first metric calculated the area under the 960 cm-1 band to the areas under the band representing hydroxyproline and proline (851, 873 and 917 cm-1), representing a measure of the amount of mineral to the amount of raw collagen.[52] The second metric used was the height of the 960 peak to the height of the CH2 wag peak (1445 cm^{-1}).[49] The third method was the area of the 960 cm-1 peak divided by the area under the Amide I band.[51] In all cases where peak fitting was required, a custom MATLAB script was implemented using the Levenberg-Marquardt method of curve fitting using mixed Gaussian-Lorentzian functions to fit each peak. This routine included an optimization step to find the best fits for the height, width, wavenumber and %Gaussian-Lorentzian.

Statistical Analysis

Results of the torsion biomechanical testing were analyzed using ANCOVA models to assess changes in the 3 main effects (genotype, alendronate treatment protocol, and duration of healing) and their interactions

using weight, fracture complexity (when applicable) and gage length as covariates. The fractured and intact tibias were initially analyzed using separate models. The models were built by starting with a model that included everything up through all of the 3-way interactions. Terms that either did not add to the model or terms with no obvious interpretation were subsequently removed. The highest order interactions of the main effects were then assessed using post-hoc tests with a Bonferroni correction to look for pairwise differences ($p<0.05$) with the covariates for gage length and weight included. A similar 3-way ANCOVA method was performed for each dependent variable assessed in the fractured tibias using the main effects of alendronate treatment, genotype, and duration of healing in a model that included the fracture complexity and weight as covariates. The final statistical models are shown in Table 7 (tx: alendronate treatment protocol, genotype: animal genotype, time: duration of healing, gage: gage length measured during torsion testing). Sample sizes for the individual groups of data used in this analysis are shown in tables Table 8 through Table 10.

To analyze the TRAP stained slides, a full factorial 2 way ANOVA was used to test for differences between treatments and genotypes. To analyze the Safranin-O / Fast Green stained slides, a 2 way ANOVA was employed. To analyze the picrosirius red stained results, a 2 way ANOVA was employed and, due to the interest in collagen orientation within the cortical bone, the difference between the polarized light metrics for the cortical bone between the Brtl/+ and WT mice were compared using a t-test.

Each experimental group in the Raman microspectroscopy analysis had sample sizes of 6-7 mice. Data from the fractured and intact tibias from these mice were analyzed using a two step approach. This approach was applied separately for each dependent variable. In the first step, the intraclass correlation coefficient was calculated to determine how much variance existed between samples in comparison to the variance of the 10 spectra within each bone. These results indicated correlations that were reasonable for all variables except the cross-linking ratio, so these 10 measurements were averaged to obtain one measurement per metric for each specimen. In the second step, a 2-way ANOVA was then applied to this aggregated data for each limb and each variable to look for changes between the genotypes and alendronate treatment protocols. As before, post-hoc tests using a Bonferroni correction were used to look for significant pairwise differences.

Results

Study Design & Animal Model

Of the 285 mice used n this analysis, most fractures were simple but there were also some wedge and complex fractures. There was no significant difference between the complexity of fractures between the Brtl/+ animals and their WT counterparts (Table 6). The weight gain that occurs during growth is not affected by alendronate treatment and Brtl/+ mice weigh less than their WT counterparts (Figure 15). This is important because of the breeding scheme used. Although a true filial analysis is only defined for intercrosses,[53] an

analysis for all of the mice in this study (assuming the progeny are one generation younger than the youngest parent for backcrosses) indicated that the mice were up to 6 generations from the founders (mean of 3.63 generations for WT mice and 4.35 generations for Brtl/+; see Figure 16 for histogram).

μCT

There was not enough bone in the fractured tibias from mice which healed for 1 week to provide a well defined boundary of the callus in μCT images, so these bones were not scanned. Only fractured tibia harvested from animals which healed for 2, 3 and 5 weeks were imaged. The detailed results are shown in Table 8. ANOVA analyses did not indicate any significant 3-way interactions between the three main variables of duration of healing, alendronate treatment protocol and genotype. Because of this, and because the fracture healing process is inherently dynamic, only meaningful two way interactions which included time were probed to look for pairwise differences. There were no measureable differences in the callus volume, bone volume fraction, or tissue mineral density of bone in the callus after 2w of healing. After 3w of healing, there was an increase in the BVF when alendronate injections were continued (Figure 17). This increase in BVF persisted through 5w of healing and, by that timepoint, the callus was also larger with continued alendronate injections (Figure 17). This change in callus volume was primarily due to a change in the dynamics. While the callus volume decreased between 2w and 5w of healing in mice that did not receive any alendronate or in mice where alendronate treatments were

halted at the time of fracture, the callus morphology maintained the same size between 3w and 5w in the animals treated with alendronate. These changes in callus morphology and volume fraction were subjectively noticeable when viewing the μCT images of fracture calluses after 5w of healing (Figure 18). Neither the genotype nor alendronate treatment protocols seemed to have an effect on density of the bone. The TMD increased in bone in the callus from 2w to 3w, and again from 3w to 5w, although even after 5w the local mineral density is still far less than the residual cortical bone. Density of the residual cortical bone increased between 3w and 5w of healing ($p=0.052$).

Biomechanical Testing

Because the μCT results only indicated a poorly defined bony callus after 1w, the fractured tibia which healed for 1w were not biomechanically tested. Only fractured tibia from mice with fractures that healed for 2w, 3w and 5w were tested. Results for the fracture calluses and intact tibiae are shown in Table 9 and Table 10, respectively. As done with the μCT analyses, the highest order interaction of the main effects that was meaningful in the ANCOVA model was investigated using post-hoc tests to look for pairwise differences. This was done because the effects of time played a major role in the healing process. The angular displacement to failure decreased from 2w to 3w (Figure 19). The stiffness, energy to failure and torque to failure increased from 2w to 3w and again from 3w to 5w (stiffness is shown in Figure 19; energy is shown in Figure 22). Therefore, any interaction without time would not account for the underlying fundamental changes and was excluded from the statistical models. The

interaction term analyzed for the stiffness data included all three main effects. For the torque at failure, angular displacement at failure, and energy to failure, this interaction only included two of the main effects (either time and treatment or time and genotype; Table 7).

The only difference after 2w of healing was a decrease in angular displacement at failure in the animals treated with alendronate both before and after the fracture in comparison to mice treated with alendronate before the fracture and a trend toward in comparison to mice that were untreated ($p = 0.076$) (not shown). After 3w of healing in WT mice, there was a decrease in stiffness for mice treated with alendronate before and after the fracture in comparison to their untreated WT counterparts (Figure 20A). In addition to this, after 3w of healing the fracture calluses from WT mice had higher stiffnesses than their Brtl/+ counterparts for the mice that were untreated and the mice that were treated with alendronate before the fracture. After 3w of healing, the energy to failure and ultimate torque were greater in fractured tibias from WT mice than in Brtl/+ when the treatment effects were pooled (Figure 20B,C). After 5w of healing, fracture calluses from WT mice increased in stiffness with continued alendronate treatment (Figure 20D), but this did not occur for Brtl/+ mice. There was an increase in the torque at failure for the fractured tibias with continued alendronate treatment in comparison to stopping the treatment at the time of fracture (Figure 20E). There was also an increase in energy to failure with continued alendronate treatment in fracture calluses after 5w of healing when

alendronate treatment was continued in comparison to the case when alendronate treatment was halted at the time of fracture (Figure 20F).

In the intact tibiae, there was an increase in the torque to failure in the animals that healed for 5w when alendronate treatment was continued after the fracture (Figure 19A). There was also a trend toward an increase in the angular displacement to failure in tibiae harvested from mice where the fracture healed for 2w in comparison to the mice where fractures healed for 3w ($p = 0.076$; data not shown). When the effects of time and alendronate treatment were pooled, there was a decrease in stiffness, angular displacement to failure, torque at failure and energy to failure in tibiae from the Brtl/+ mice (Figure 21). In addition to providing information that verified the genotype and treatment effects, the biomechanical data for the intact tibias were used as a reference to determine if there was any fundamental difference in fracture healing in Brtl/+ animals. Plotting the energy to failure in mice that were not treated with alendronate showed a drastic increase in the energy to failure in Brtl/+ mice after 5w of healing that was not present in the WT mice (Figure 22).

Quantitative Histology

Data from the Safranin-O / fast green slides indicated the presence of cartilage through 2w of healing, but this had dissipated by 3w. Neither the genotype nor the alendronate treatment protocol had an impact on the amount of cartilage present in the callus. There was also no detectable change in the

percentage of cartilage that contained trabeculated woven bone with alendronate treatment.(Figure 23)

It was clear that the alendronate treatment protocol had an effect on callus volume after 5w of healing based on μCT data. Therefore, TRAP analysis was only performed on slides from animals which healed for 5w. This callus volume would primarily be caused by changes occurring at the callus boundary, so this was the only surface analyzed. A 2-way ANOVA analysis did not indicate any change in the osteoclast surface per bone surface or the number of osteoclasts between the genotypes or the alendronate treatment protocols (Figure 24).

In order to better understand the increased energy to failure in the fracture callus compared to intact tibiae in Brtl/+ mice after 5w of healing, a polarized light analysis was employed to look more directly at the collagen structure. Plotting the mean intensity versus stage angle indicated a remarkable difference in collagen orientation between bone in the callus and the residual cortical bone, implying that bone in the callus is more woven in nature. This difference was quantified using the parallelism index (PI) in fractured tibiae from mice which healed for 5w. The PI for bone from the callus was significantly lower than residual cortical bone, verifying the woven nature of this mineralized tissue (Figure 25). A t-test to compare the difference in PI in cortical bone between Brtl/+ and WT mice indicated a trend toward a decreased PI in Brtl/+ mice ($p=0.072$).

Raman Microspectroscopy

In order to understand what ultrastructural differences occurred in the callus that may have preceded changes in the callus morphology and bone seen after 5w with continued alendronate treatment, Raman microspectroscopy was performed on the fracture calluses and the contralateral intact tibiae from mice which healed for 3w. Of all the outcome metrics investigated, the cross-linking ratio data had the lowest intraclass correlation coefficient implying that this measurement has the most variability within a bone (Table 11). The intraclass correlation coefficients for the other outcome metrics were high enough that we chose to aggregate the data within each bone and used a 2-way ANOVA to look for differences. The mineral to matrix ratio was a primary variable of interest due to the change in gross morphologic measurements, so three metrics for mineral to matrix ratio were calculated separately. The results of these metrics were highly correlated and selecting a different metric did not substantially change the interpretation (Figure 26). Within a genotype, the mineral to matrix ratio was not affected by the alendronate treatment (Figure 27A). In comparing the genotypes, there was a trend toward a decrease in the mineral to matrix ratio in the intact tibia of Brtl/+ mice when alendronate treatment was continued. There was a significant decrease in mineral to matrix ratio in the fracture calluses from the same Brtl/+ mice which received alendronate during healing, and there was a trend toward a decrease in Brtl/+ when alendronate treatment was stopped at fracture. There was no change in the cross-linking ratio (data not shown), although there were some mineral changes. Mineral in the intact tibiae of Brtl/+

mice was less crystalline in the mice which did not receive alendronate. Fracture calluses from Brtl/+ mice which did not receive alendronate also had less crystalline mineral with a higher carbonate to phosphate ratio, as did Brtl/+ mice which received alendronate treatment before and after the fracture. Plotting the crystallinity against the carbonate to phosphate ratio revealed that these changes may be associated with one another (Figure 27C). There also seemed to be a positive correlation between higher mineral to matrix ratios and the crystallinity (Figure 27B).

Discussion

Patients with OI have been treated with bisphosphonates to decrease fracture risk. This has been successful, although it remains unclear how to proceed when an OI patient on bisphosphonates presents with a subsequent fracture. This study, using the Brtl/+ knock-in mouse model of OI, was designed to help address this question. Continuing alendronate treatment during healing prevents the decrease in callus volume that would normally occur between 3 and 5 weeks of healing. This larger callus, in conjunction with the increase in bone volume fraction at this timepoint, may explain the increase in torque at failure. These results are similar to other studies examining bisphosphonates during fracture healing that have found increases in callus size and the associated structural biomechanical properties.[21,22,24-26,30]

However, when alendronate treatment was halted at the time of fracture, there were only very subtle alterations in healing when compared to the groups

where no injections were ever administered. This is corroborated by previous studies where stopping treatment at fracture with modest doses of incandronate does not result in a change in callus size or structural biomechanical properties.[30,34] When these authors quantified the amount of incandronate in the callus, there was no difference in the amount of incandronate between the callus and the cortical bone.[30] This may indicate that the amount of alendronate which was released into the fracture was relatively small and explain the lack of change in the pre-treated animals even though alendronate can exhibit a strong effect. Furthermore, assessing the cortical morphology in the intact tibiae from mice which healed for 1w (corresponding to 7w of treatment) did not indicate a difference in the cortical thickness in alendronate treated mice (Figure 28). Alendronate treatment over 12 weeks in Brtl/+ mice can result in thicker cortical bone with an increase in the ultimate load,[38] although the most striking affect is typically seen in trabecular bone. Similar to previously published results,[38] there were a noticeable bands of trabecular bone in mice which received alendronate (Figure 29). When this was quantified in an earlier study, the results indicated that more bisphosphonate was delivered to the trabecular bone than the cortical bone.[54] The fractures in this study were distal to any metaphyseal trabecular bone, and alendronate has a high affinity for bone mineral, further reinforcing the possibility that the local dose of alendronate released from the fractured cortical bone may not have been high enough to exert an effect.

To investigate the changes in resorption at the cellular level, TRAP staining was performed. Based on the decrease in callus volume between 3 and

5 weeks of healing, this outer callus boundary would have been undergoing active resorption after 5 weeks of healing so only this surface was examined. There was no detectable change in the number of osteoclasts or in the osteoclast surface per bone surface between the genotypes and bisphosphonate treatment protocols. This was initially surprising given the increased number of osteoclasts in Brtl/+ mice,[37] and an indication that alendronate treatment can result in an increase osteoclast surface after 3 weeks of fracture healing in a mouse model.[25] However, other data do not indicate a change in osteoclast number after 4 or 16 weeks of healing in rat models,[24,30]. One of these studies indicates a decrease in osteoclast number after 6 weeks of healing with alendronate in rats,[24] whereas zoledronic acid did not affect osteoclast number after 6 weeks in a different model.[22] Based on these disparities in previously published data, it is possible that the fracture healing dynamics after 5 weeks of healing in this study are negating the changes of earlier treatment and genotype differences.

An additional histological assessment to investigate the endochondral ossification process and the rates of transition from cartilage to bone did not find any alteration in Brtl/+ animals. Similar to previously published results,[22,32] there was no noticeable change in the rate of endochondral ossification when alendronate was administered. This reinforces the notion that early fracture healing in Brtl/+ animals is comparable to normal healing. To investigate this question in more depth, transient changes during healing were assessed. The energy to failure in fracture calluses from Brtl/+ mice which did not receive

alendronate is significantly increased in comparison to the contralateral intact tibia after 5 weeks of healing. This can partially be attributed to the callus being larger than the intact tibia. However, in WT mice, the callus was larger than the intact tibia without resulting in a significant change in energy to failure. Taken together, this implies that an alternative mechanism may contribute to the biomechanical properties in fracture calluses from Brtl/+ mice. We investigated the collagen orientation using polarized light from Brtl/+ mice which did not receive alendronate and quantified the collagen organization in both the fracture callus and the residual cortical bone. Similar to previously published studies,[55] bone in the callus was far less organized than cortical bone (Figure 25) indicating that this callus bone is more woven. This change in collagen orientation may govern the biomechanics during healing. In cortical bone Collagen may be slightly less organized in Brtl/+ mice in comparison their WT counterparts (Figure 25). This may partially contribute to the biomechanical changes present in the phenotype, but these alterations are not sufficient to prevent bone fragility (Figure 21). A similar trend was not seen after 6 weeks of fracture healing in oim/oim mice,[56] another mouse model for OI, so it is unclear if this result is related to the type of mutation or if it is generally true for healing in OI

Other transient changes were also investigated during healing. No μCT imaging was performed on calluses after only 1 week of healing because, similar to previously published results,[57] these calluses were predominately soft tissue and didn’t contain bone. The mineral density of bone in the callus subsequently

increased as ossification progressed. Looking at changes between 2 weeks and 3 weeks of healing, the stiffness increased and the angular displacement to failure decreased. Both can be attributed to the removal of cartilage at these timepoints seen histologically. Therefore, 3 weeks was the earliest healing timepoint when the calluses were bridged and cartilage was removed.

Raman microspectroscopy was performed to investigate changes in healing at this 3 week timepoint that may have led to the morphologic and functional changes seen after 5 weeks of healing. The Raman analysis did not indicate any affect of alendronate treatment at the peripheral callus boundary and the periosteal surface of the intact bone. The mice were euthanized one week after the last alendronate injection so, if there are spatial dependencies based on the presence of alendronate in circulation during bone formation, these surfaces may not have detected it. Comparison of the Raman results between the genotypes supports this possibility. The decreased crystallinity in intact tibiae from Brtl/+ mice is contradictory to previously published results that do not show a change in crystallinity in interior cortical bone.[36] The crystallinity differences seem to be correlated to a change in mineral to matrix ratio, possibly implying that crystallinity changes with localized mineral deposition. None of the mineral changes seem to be related to an alteration in cross-linking, although this is the most difficult metric to assess because it was the most variable outcome within each bone.

There are also limitations in this study. Because of the lethality in Brtl/+ pups,[35] and the desire to only use male mice to control for possible gender

differences, a breeding scheme was chosen to result in litters of pups which would only have be Brtl/+. This required crossing Brtl/Brtl and WT mice which may potentially induce additional recessive genetic variation. However, the Brtl/+ mice used in this study were not more than 6 generations from the WT and Brtl/+ colony founders. Given that the Brtl/+ used in this study still weighed less than their WT counterparts and the intact tibia showed the expected structural biomechanical deficiencies that would be expected in OI, the mice used in the study are still a viable OI model. Another limitation is that the untreated control group did not receive saline injections as a control. This choice was made to improve translational interpretation because no ‘untreated’ patient would receive injections. While this may have an effect on animal stress and physiology, the untreated mice were still handled weekly during weighing like their treated counterparts, and the mice which did receive treatment did not need to be sedated for the relatively simple subcutaneous injection. Another limitation is that the ANCOVA statistical analysis used weight as a covariate when analyzing the biomechanical data instead of using the bone size directly. However, weight is an appropriate proxy for size because the intact tibias had drastically different morphology than the fracture calluses and weight could be used as a covariate in both analyses. Last, while four timepoints were analyzed to encompass the range of ossification and early remodeling to understand changes in fracture healing dynamics, there are still aspects of late remodeling dynamics that were not directly examined. Investigations which look at later timepoints are needed to

understand if fracture calluses from mice treated with alendronate during healing will ever remodel and return to a normal cortical morphology.

In conclusion, fracture calluses contain woven bone during healing that seemed to override the biomechanical deficiencies inherent in intact bones from Brtl/+ mice. Treating these mice with alendronate during fracture resulted in larger calluses with increased structural biomechanical properties although it altered the normal dynamics of healing by preventing the decrease in callus volume later in the healing process. If the same is true in OI patients taking bisphosphonates during healing, this geometric advantage may help reduce the inherent fracture risk. However, since these larger calluses will contain more bisphosphonates that could potentially reside in the skeleton for a prolonged period of time in these pediatric patients, and since fracture healing seems to be relatively normal when alendronate treatment was not present during healing, a plausible clinical approach may also be to halt treatment at the time of fracture and resume therapeutic treatment after the fracture is well healed and mostly resorbed.

References

1. Marini, J.C., Forlino, A., Cabral, W.A., Barnes, A.M., San Antonio, J.D., Milgrom, S., Hyland, J.C., Korkko, J., Prockop, D.J., De Paepe, A., et al. 2007. Consortium for osteogenesis imperfecta mutations in the helical domain of type I collagen: regions rich in lethal mutations align with collagen binding sites for integrins and proteoglycans. *Hum Mutat* 28:209-221.
2. Baldridge, D., Schwarze, U., Morello, R., Lennington, J., Bertin, T.K., Pace, J.M., Pepin, M.G., Weis, M., Eyre, D.R., Walsh, J., et al. 2008. CRTAP and LEPRE1 mutations in recessive osteogenesis imperfecta. *Hum Mutat* 29:1435-1442.

3. Cheung, M.S., Glorieux, F.H., and Rauch, F. 2007. Natural history of hyperplastic callus formation in osteogenesis imperfecta type V. *Journal of Bone and Mineral Research* 22:1181-1186.
4. Ramirez, N., Vilella, F.E., Colon, M., and Flynn, J.M. 2003. Osteogenesis imperfecta and hyperplastic callus formation in a family: a report of three cases and a review of the literature. *J Pediatr Orthop B* 12:88-96.
5. Alharbi, M., Pinto, G., Finidori, G., Souberbielle, J.C., Guillou, F., Gaubicher, S., Le Merrer, M., and Polak, M. 2009. Pamidronate treatment of children with moderate-to-severe osteogenesis imperfecta: a note of caution. *Horm Res* 71:38-44.
6. Herring, J.A., Tachdjian, M.O., and Texas Scottish Rite Hospital for Children. 2002. Tachdjian's pediatric orthopaedics. Philadelphia: W.B. Saunders. 3 v. (xxxv, 2438, li p.).
7. Gatti, D., Antoniazzi, F., Prizzi, R., Braga, V., Rossini, M., Tato, L., Viapiana, O., and Adami, S. 2005. Intravenous neridronate in children with osteogenesis imperfecta: a randomized controlled study. *J Bone Miner Res* 20:758-763.
8. Letocha, A.D., Cintas, H.L., Troendle, J.F., Reynolds, J.C., Cann, C.E., Chernoff, E.J., Hill, S.C., Gerber, L.H., and Marini, J.C. 2005. Controlled trial of pamidronate in children with types III and IV osteogenesis imperfecta confirms vertebral gains but not short-term functional improvement. *J Bone Miner Res* 20:977-986.
9. Rauch, F., Munns, C.F., Land, C., Cheung, M., and Glorieux, F.H. 2009. Risedronate in the treatment of mild pediatric osteogenesis imperfecta: a randomized placebo-controlled study. *J Bone Miner Res* 24:1282-1289.
10. Sakkers, R., Kok, D., Engelbert, R., van Dongen, A., Jansen, M., Pruijs, H., Verbout, A., Schweitzer, D., and Uiterwaal, C. 2004. Skeletal effects and functional outcome with olpadronate in children with osteogenesis imperfecta: a 2-year randomised placebo-controlled study. *Lancet* 363:1427-1431.
11. Russell, R.G., Watts, N.B., Ebetino, F.H., and Rogers, M.J. 2008. Mechanisms of action of bisphosphonates: similarities and differences and their potential influence on clinical efficacy. *Osteoporos Int* 19:733-759.
12. Gertz, B.J., Holland, S.D., Kline, W.F., Matuszewski, B.K., and Porras, A.G. 1993. Clinical pharmacology of alendronate sodium. *Osteoporos Int* 3 Suppl 3:S13-16.
13. Ward, L.M., Denker, A.E., Porras, A., Shugarts, S., Kline, W., Travers, R., Mao, C., Rauch, F., Maes, A., Larson, P., et al. 2005. Single-dose pharmacokinetics and tolerability of alendronate 35- and 70-milligram tablets in children and adolescents with osteogenesis imperfecta type I. *J Clin Endocrinol Metab* 90:4051-4056.
14. Black, D.M., Schwartz, A.V., Ensrud, K.E., Cauley, J.A., Levis, S., Quandt, S.A., Satterfield, S., Wallace, R.B., Bauer, D.C., Palermo, L., et al. 2006. Effects of continuing or stopping alendronate after 5 years of treatment: the Fracture Intervention Trial Long-term Extension (FLEX): a randomized trial. *JAMA* 296:2927-2938.

15. Papapoulos, S.E., and Cremers, S.C. 2007. Prolonged bisphosphonate release after treatment in children. *N Engl J Med* 356:1075-1076.
16. Whyte, M.P., McAlister, W.H., Novack, D.V., Clements, K.L., Schoenecker, P.L., and Wenkert, D. 2008. Bisphosphonate-induced osteopetrosis: novel bone modeling defects, metaphyseal osteopenia, and osteosclerosis fractures after drug exposure ceases. *J Bone Miner Res* 23:1698-1707.
17. Marini, J.C. 2009. Bone: Use of bisphosphonates in children-proceed with caution. *Nat Rev Endocrinol* 5:241-243.
18. Lyles, K.W., Colon-Emeric, C.S., Magaziner, J.S., Adachi, J.D., Pieper, C.F., Mautalen, C., Hyldstrup, L., Recknor, C., Nordsletten, L., Moore, K.A., et al. 2007. Zoledronic acid and clinical fractures and mortality after hip fracture. *N Engl J Med* 357:1799-1809.
19. Munns, C.F., Rauch, F., Zeitlin, L., Fassier, F., and Glorieux, F.H. 2004. Delayed osteotomy but not fracture healing in pediatric osteogenesis imperfecta patients receiving pamidronate. *J Bone Miner Res* 19:1779-1786.
20. Pizones, J., Plotkin, H., Parra-Garcia, J.I., Alvarez, P., Gutierrez, P., Bueno, A., and Fernandez-Arroyo, A. 2005. Bone healing in children with osteogenesis imperfecta treated with bisphosphonates. *J Pediatr Orthop* 25:332-335.
21. Amanat, N., Brown, R., Bilston, L.E., and Little, D.G. 2005. A single systemic dose of pamidronate improves bone mineral content and accelerates restoration of strength in a rat model of fracture repair. *J Orthop Res* 23:1029-1034.
22. Amanat, N., McDonald, M., Godfrey, C., Bilston, L., and Little, D. 2007. Optimal timing of a single dose of zoledronic acid to increase strength in rat fracture repair. *J Bone Miner Res* 22:867-876.
23. Bauss, F., and Russell, R.G. 2004. Ibandronate in osteoporosis: preclinical data and rationale for intermittent dosing. *Osteoporos Int* 15:423-433.
24. Cao, Y., Mori, S., Mashiba, T., Westmore, M.S., Ma, L., Sato, M., Akiyama, T., Shi, L., Komatsubara, S., Miyamoto, K., et al. 2002. Raloxifene, estrogen, and alendronate affect the processes of fracture repair differently in ovariectomized rats. *J Bone Miner Res* 17:2237-2246.
25. Gerstenfeld, L.C., Sacks, D.J., Pelis, M., Mason, Z.D., Graves, D.T., Barrero, M., Ominsky, M.S., Kostenuik, P.J., Morgan, E.F., and Einhorn, T.A. 2009. Comparison of effects of the bisphosphonate alendronate versus the RANKL inhibitor denosumab on murine fracture healing. *J Bone Miner Res* 24:196-208.
26. Greiner, S.H., Wildemann, B., Back, D.A., Alidoust, M., Schwabe, P., Haas, N.P., and Schmidmaier, G. 2008. Local application of zoledronic acid incorporated in a poly(D,L-lactide)-coated implant accelerates fracture healing in rats. *Acta Orthop* 79:717-725.
27. Koivukangas, A., Tuukkanen, J., Kippo, K., Jamsa, T., Hannuniemi, R., Pasanen, I., Vaananen, K., and Jalovaara, P. 2003. Long-term

administration of clodronate does not prevent fracture healing in rats. *Clin Orthop Relat Res*:268-278.
28. Lenehan, T.M., Balligand, M., Nunamaker, D.M., and Wood, F.E., Jr. 1985. Effect of EHDP on fracture healing in dogs. *J Orthop Res* 3:499-507.
29. Li, C., Mori, S., Li, J., Kaji, Y., Akiyama, T., Kawanishi, J., and Norimatsu, H. 2001. Long-term effect of incadronate disodium (YM-175) on fracture healing of femoral shaft in growing rats. *J Bone Miner Res* 16:429-436.
30. Li, J., Mori, S., Kaji, Y., Kawanishi, J., Akiyama, T., and Norimatsu, H. 2000. Concentration of bisphosphonate (incadronate) in callus area and its effects on fracture healing in rats. *J Bone Miner Res* 15:2042-2051.
31. Madsen, J.E., Berg-Larsen, T., Kirkeby, O.J., Falch, J.A., and Nordsletten, L. 1998. No adverse effects of clodronate on fracture healing in rats. *Acta Orthop Scand* 69:532-536.
32. McDonald, M.M., Dulai, S., Godfrey, C., Amanat, N., Sztynda, T., and Little, D.G. 2008. Bolus or weekly zoledronic acid administration does not delay endochondral fracture repair but weekly dosing enhances delays in hard callus remodeling. *Bone* 43:653-662.
33. Peter, C.P., Cook, W.O., Nunamaker, D.M., Provost, M.T., Seedor, J.G., and Rodan, G.A. 1996. Effect of alendronate on fracture healing and bone remodeling in dogs. *J Orthop Res* 14:74-79.
34. Li, J., Mori, S., Kaji, Y., Mashiba, T., Kawanishi, J., and Norimatsu, H. 1999. Effect of bisphosphonate (incadronate) on fracture healing of long bones in rats. *J Bone Miner Res* 14:969-979.
35. Forlino, A., Porter, F.D., Lee, E.J., Westphal, H., and Marini, J.C. 1999. Use of the Cre/lox recombination system to develop a non-lethal knock-in murine model for osteogenesis imperfecta with an alpha1(I) G349C substitution. Variability in phenotype in BrtlIV mice. *J Biol Chem* 274:37923-37931.
36. Kozloff, K.M., Carden, A., Bergwitz, C., Forlino, A., Uveges, T.E., Morris, M.D., Marini, J.C., and Goldstein, S.A. 2004. Brittle IV mouse model for osteogenesis imperfecta IV demonstrates postpubertal adaptations to improve whole bone strength. *J Bone Miner Res* 19:614-622.
37. Uveges, T.E., Collin-Osdoby, P., Cabral, W.A., Ledgard, F., Goldberg, L., Bergwitz, C., Forlino, A., Osdoby, P., Gronowicz, G.A., and Marini, J.C. 2008. Cellular mechanism of decreased bone in Brtl mouse model of OI: imbalance of decreased osteoblast function and increased osteoclasts and their precursors. *J Bone Miner Res* 23:1983-1994.
38. Uveges, T.E., Kozloff, K.M., Ty, J.M., Ledgard, F., Raggio, C.L., Gronowicz, G., Goldstein, S.A., and Marini, J.C. 2009. Alendronate treatment of the brtl osteogenesis imperfecta mouse improves femoral geometry and load response before fracture but decreases predicted material properties and has detrimental effects on osteoblasts and bone formation. *J Bone Miner Res* 24:849-859.
39. Taylor, D.K., Meganck, J.A., Terkhorn, S., Rajani, R., Naik, A., O'Keefe, R.J., Goldstein, S.A., and Hankenson, K.D. 2009. Thrombospondin-2

Influences the Proportion of Cartilage and Bone During Fracture Healing. *J Bone Miner Res*.
40. 1996. Fracture and dislocation compendium. Orthopaedic Trauma Association Committee for Coding and Classification. *J Orthop Trauma* 10 Suppl 1:v-ix, 1-154.
41. Meganck, J.A., Kozloff, K.M., Thornton, M.M., Broski, S.M., and Goldstein, S.A. 2009. Beam Hardening Artifacts in Micro-Computed Tomography Scanning can be Reduced by X-ray Beam Filtration and the Resulting Images can be used to Accurately Measure BMD. *Bone*.
42. Ruifrok, A.C., and Johnston, D.A. 2001. Quantification of histochemical staining by color deconvolution. *Anal Quant Cytol Histol* 23:291-299.
43. Smith, E.J., McEvoy, A., Little, D.G., Baldock, P.A., Eisman, J.A., and Gardiner, E.M. 2004. Transient retention of endochondral cartilaginous matrix with bisphosphonate treatment in a long-term rabbit model of distraction osteogenesis. *J Bone Miner Res* 19:1698-1705.
44. Rieppo, J., Hallikainen, J., Jurvelin, J.S., Kiviranta, I., Helminen, H.J., and Hyttinen, M.M. 2008. Practical considerations in the use of polarized light microscopy in the analysis of the collagen network in articular cartilage. *Microsc Res Tech* 71:279-287.
45. Silva, M.J., Brodt, M.D., Wopenka, B., Thomopoulos, S., Williams, D., Wassen, M.H., Ko, M., Kusano, N., and Bank, R.A. 2006. Decreased collagen organization and content are associated with reduced strength of demineralized and intact bone in the SAMP6 mouse. *J Bone Miner Res* 21:78-88.
46. Esmonde-White, F.W.L., Schulmerich, M.V., Esmonde-White, K.A., and Morris, M.D. 2009. Automated Raman spectral preprocessing of bone and other musculoskeletal tissues. In *Proceedings of the SPIE*. A. Mandelis, editor. 716605-716605-716610.
47. Lieber, C.A., and Mahadevan-Jansen, A. 2003. Automated method for subtraction of fluorescence from biological Raman spectra. *Appl Spectrosc* 57:1363-1367.
48. Kazanci, M., Fratzl, P., Klaushofer, K., and Paschalis, E.P. 2006. Complementary information on in vitro conversion of amorphous (precursor) calcium phosphate to hydroxyapatite from Raman microspectroscopy and wide-angle X-ray scattering. *Calcif Tissue Int* 79:354-359.
49. Dehring, K.A., Crane, N.J., Smukler, A.R., McHugh, J.B., Roessler, B.J., and Morris, M.D. 2006. Identifying chemical changes in subchondral bone taken from murine knee joints using Raman spectroscopy. *Appl Spectrosc* 60:1134-1141.
50. Paschalis, E.P., Verdelis, K., Doty, S.B., Boskey, A.L., Mendelsohn, R., and Yamauchi, M. 2001. Spectroscopic characterization of collagen cross-links in bone. *J Bone Miner Res* 16:1821-1828.
51. Wallace, J.M., Golcuk, K., Morris, M.D., and Kohn, D.H. 2009. Inbred strain-specific response to biglycan deficiency in the cortical bone of C57BL6/129 and C3H/He mice. *J Bone Miner Res* 24:1002-1012.

52. Kohn, D.H., Sahar, N.D., Wallace, J.M., Golcuk, K., and Morris, M.D. 2009. Exercise alters mineral and matrix composition in the absence of adding new bone. *Cells Tissues Organs* 189:33-37.
53. Silver, L.M. 1995. *Mouse genetics : concepts and applications*. New York: Oxford University Press. xiii, 362 p. pp.
54. Kozloff, K.M., Weissleder, R., and Mahmood, U. 2007. Noninvasive optical detection of bone mineral. *J Bone Miner Res* 22:1208-1216.
55. Tonna, E.A. 1964. Fracture Callus Formation in Young and Old Mice Observed with Polarized Light Microscopy. *Anat Rec* 150:349-361.
56. Delos, D., Yang, X., Ricciardi, B.F., Myers, E.R., Bostrom, M.P., and Camacho, N.P. 2008. The effects of RANKL inhibition on fracture healing and bone strength in a mouse model of osteogenesis imperfecta. *J Orthop Res* 26:153-164.
57. Duvall, C.L., Taylor, W.R., Weiss, D., Wojtowicz, A.M., and Guldberg, R.E. 2007. Impaired angiogenesis, early callus formation, and late stage remodeling in fracture healing of osteopontin-deficient mice. *Journal of Bone and Mineral Research* 22:286-297.

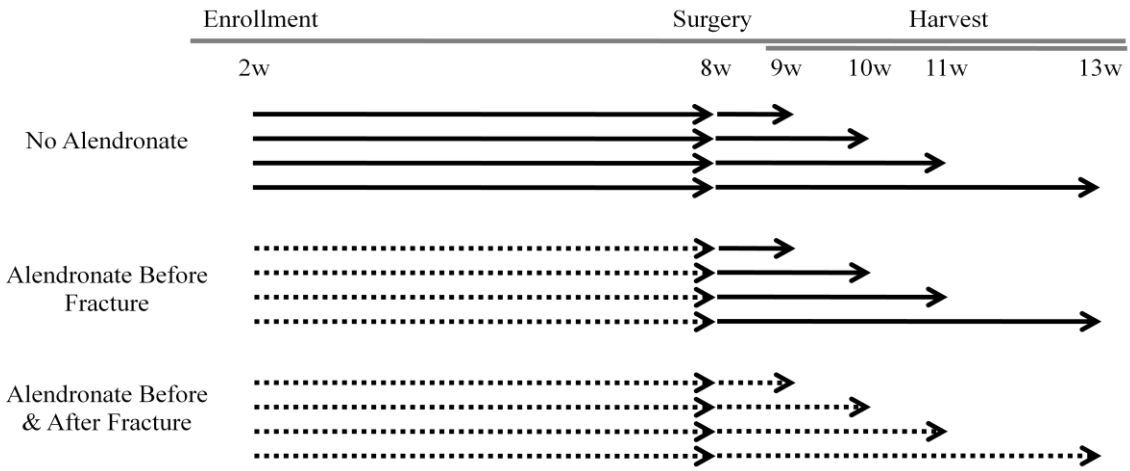

Figure 14: Study Design for the Brtl/+ fracture healing experiment.

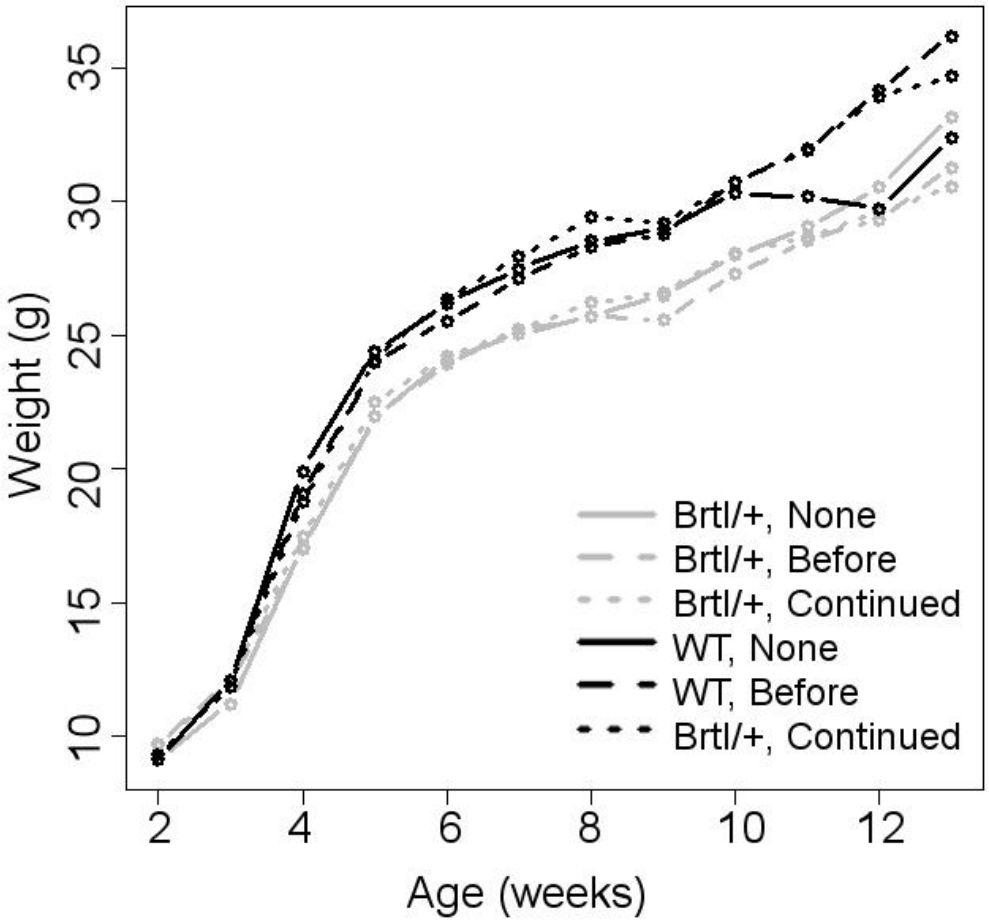

Figure 15: Growth curves for Brtl/+ and WT mice with and without alendronate treatment.

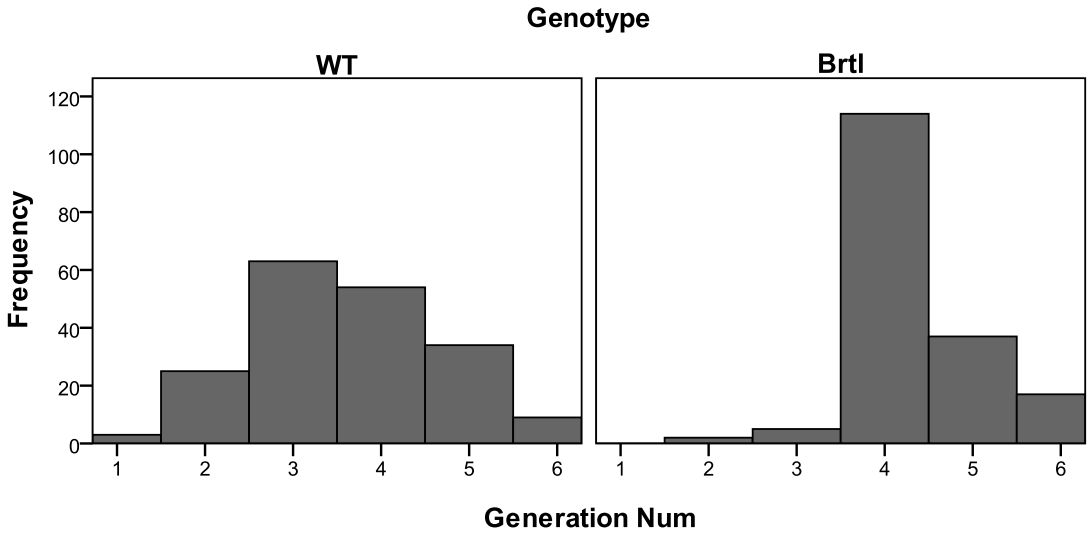

Figure 16: Filial histogram to examine generations of mice used in the Brtl/+ fracture healing experiment.

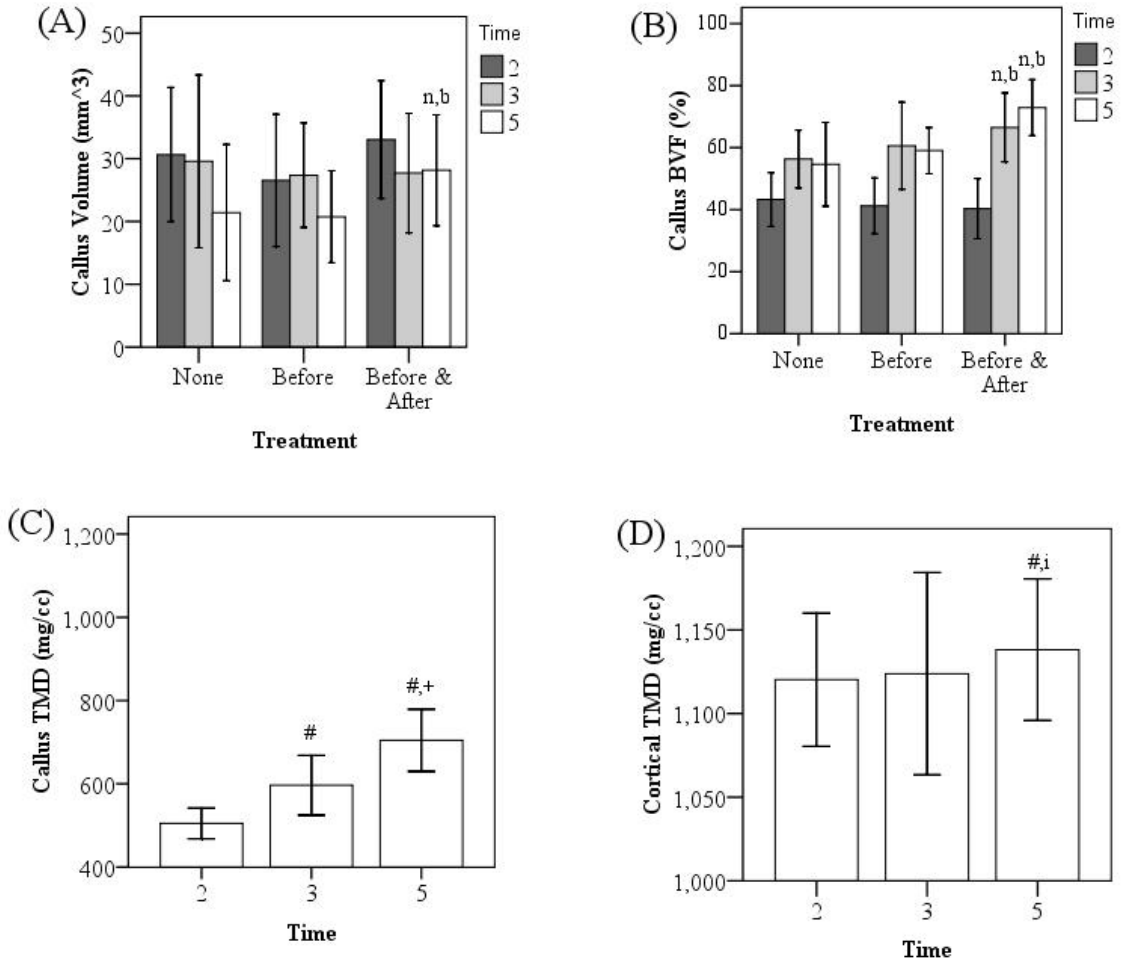

Figure 17: Quantitative μCT results for callus morphology and densitometry.

These results are for (A) callus volume and (B) bone volume fraction during healing. The tissue mineral densities were also examined for the (C) bone in the callus and (D) residual cortical bone. Notations indicate significance with respect to no alendronate treatment (n), alendronate treatment before fracture (b), 2 weeks of healing (#) or 3 weeks of healing (+). There was also a trend in comparison to 3 weeks of healing (i; p=0.064).

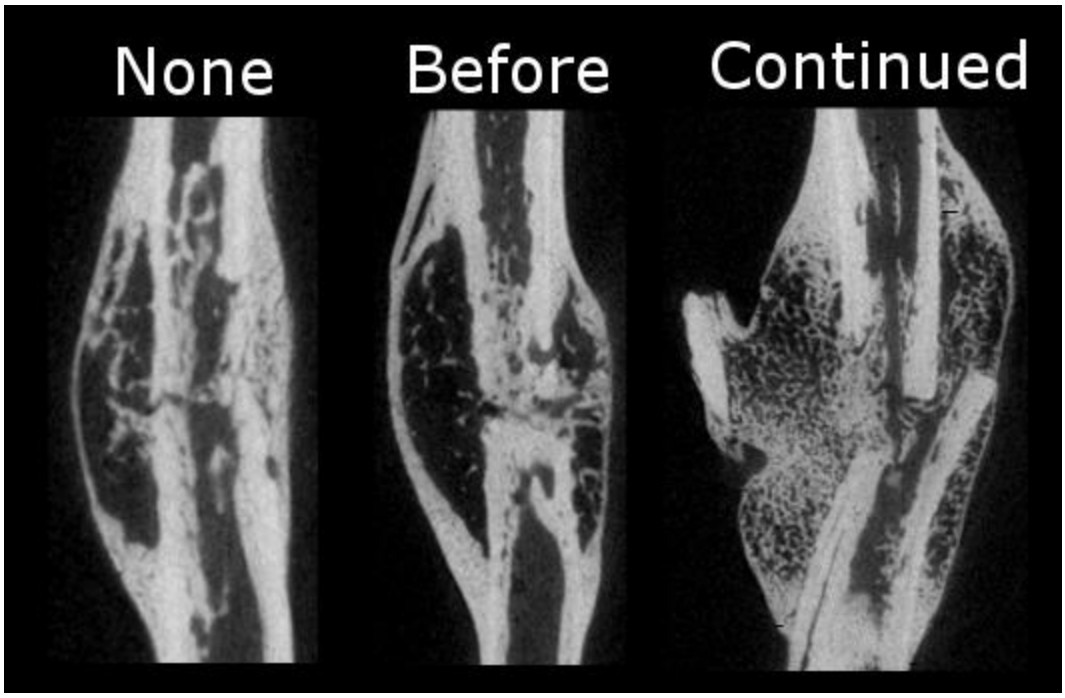

Figure 18: Representative μCT images taken from WT mice after 5w of healing.

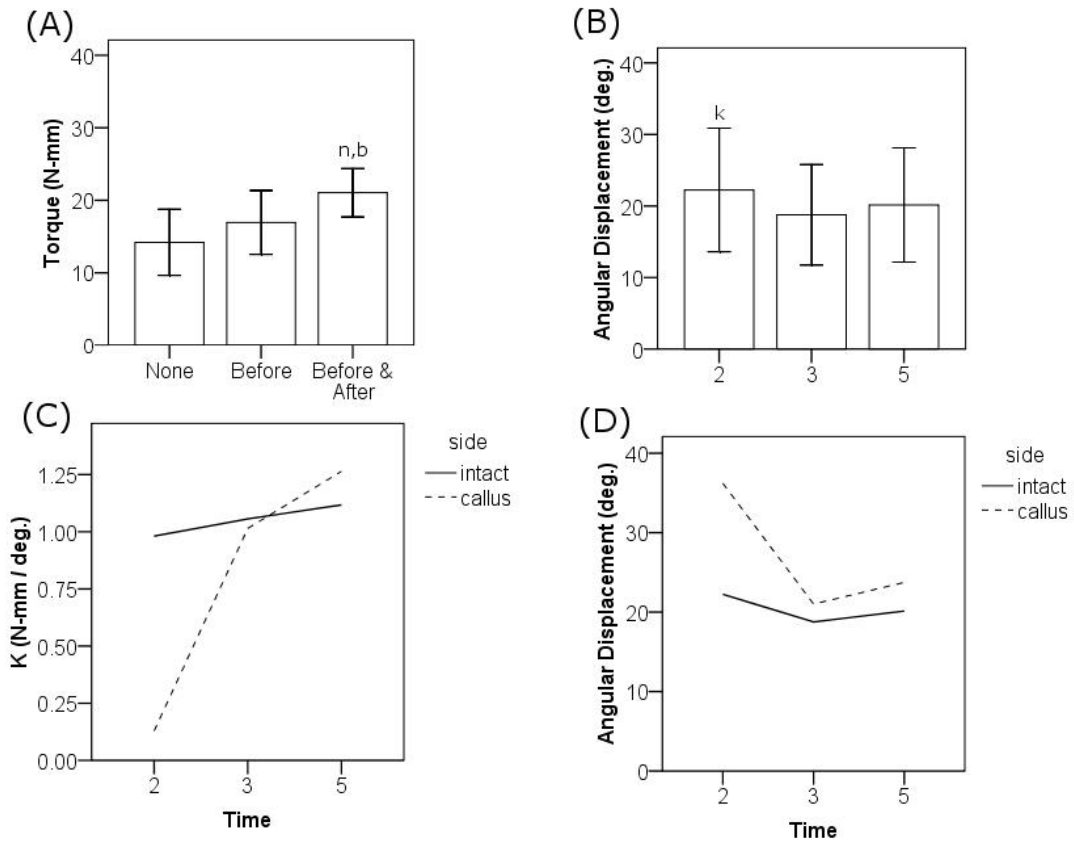

Figure 19: Biomechanical properties fractured and intact tibiae over time.

These results show the torque at failure after 5w of healing (A). The changes in time were examined for angular displacement to failure (B,D) and stiffness (C). Notations indicate significance with respect to no alendronate treatment (n), alendronate treatment before fracture (b) or a trend with respect to 3w (k; p=0.076).

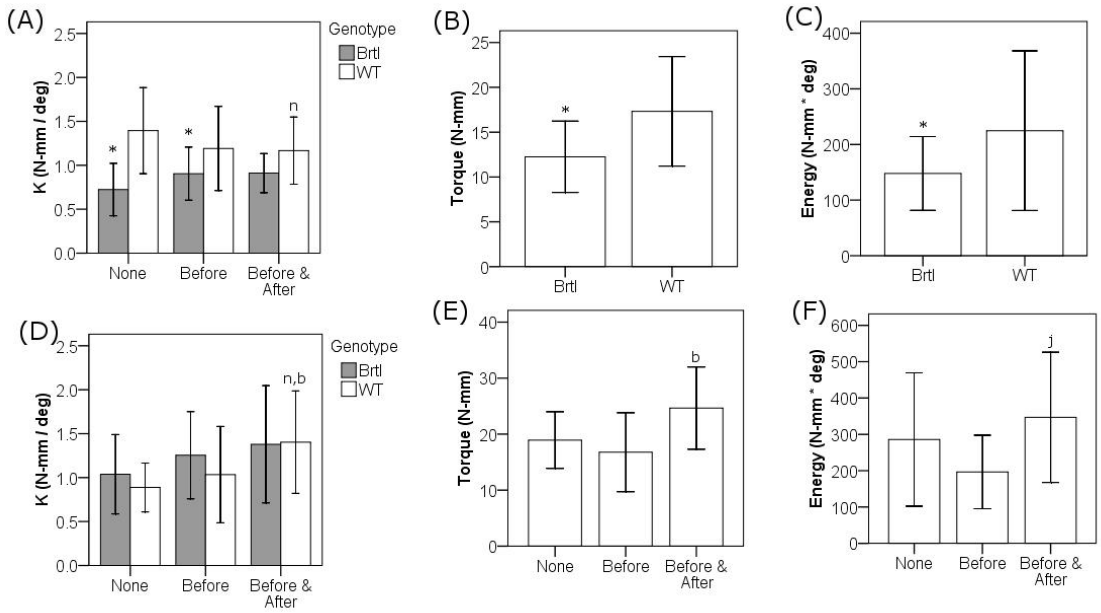

Figure 20: Biomechanical changes in fracture calluses based on genotypic and treatment protocol variations.

The differences are shown after 3 weeks of healing (A-C) or 5 weeks of healing (D-F). The differences are shown for stiffness (A,D), torque at failure (B,E) or energy to failure (C,F). Notations indicate significance with respect to no alendronate treatment (n), alendronate treatment before fracture (b), or between the genotypes (*). In (F), there was also a trend toward a difference between the mice which received alendronate during healing and those where alendronate treatments were stopped at the time of fracture (j; p=0.053).

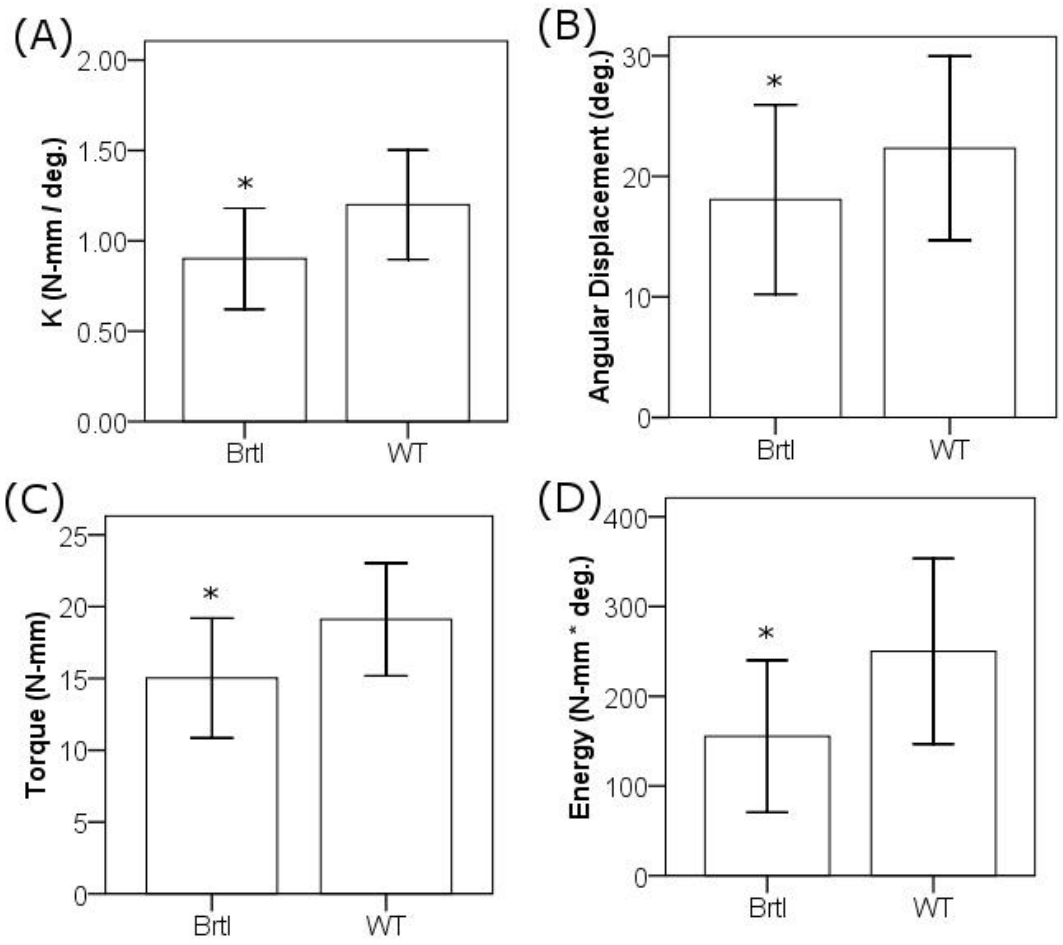

Figure 21: Torsional properties of intact tibiae.

The results are pooled over time and treatment for stiffness (A), angular displacement to failure (B), torque at failure (C) and energy to Failure (D). Notations indicate significance with respect to genotype differences (*; $p<0.05$).

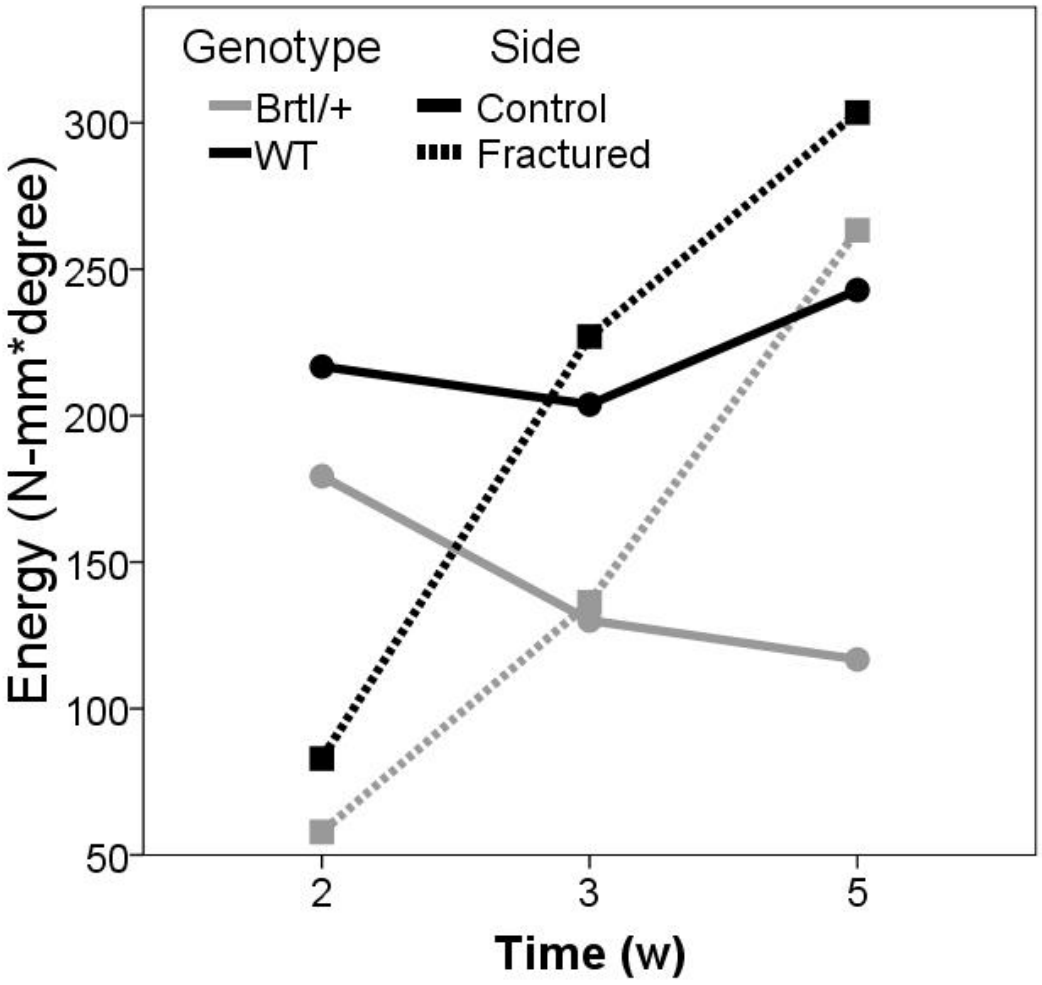

Figure 22: Examination of energy to failure during healing.

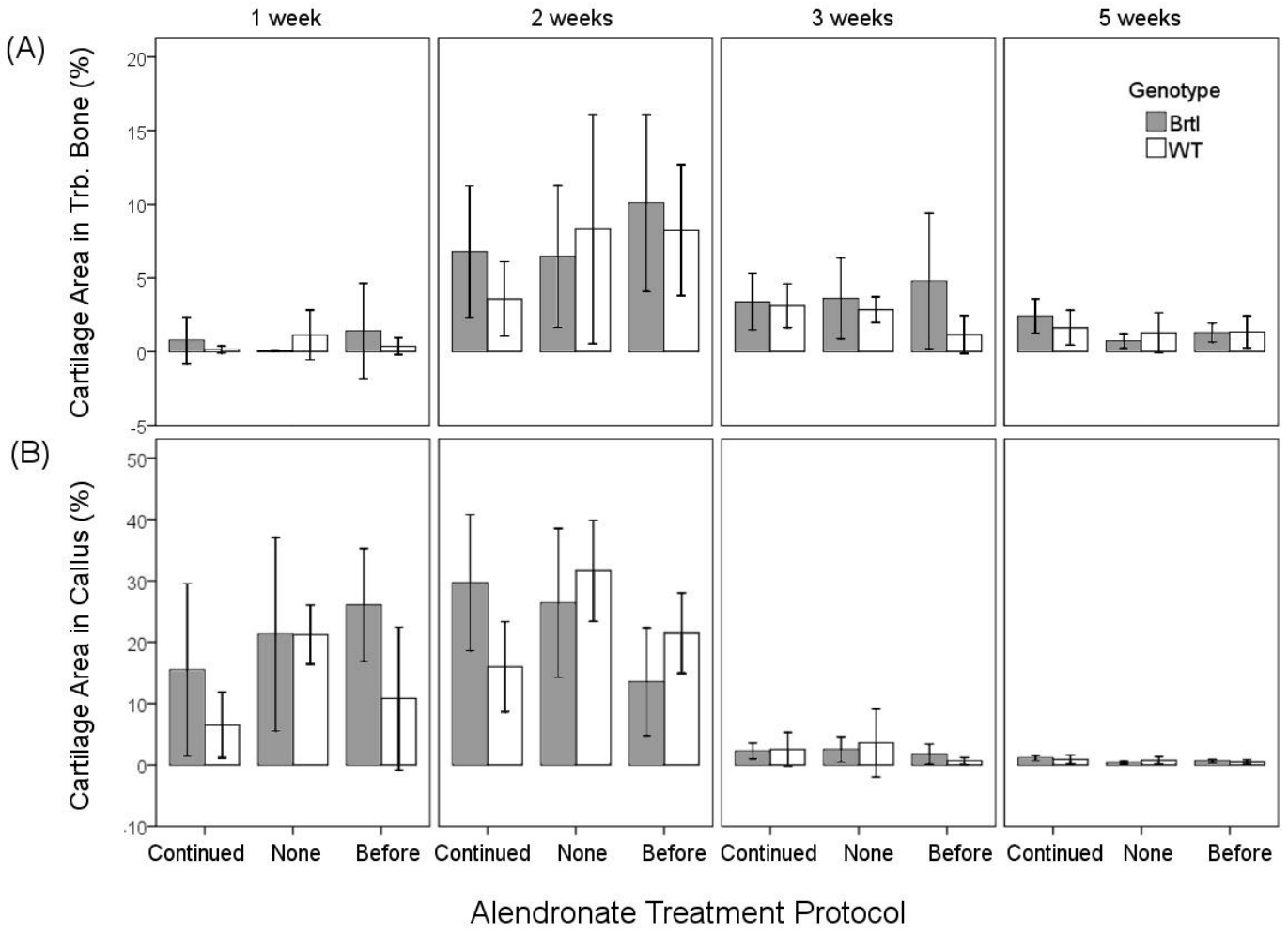

Figure 23: Histomorphometry Results for Safranin-O stained slides.

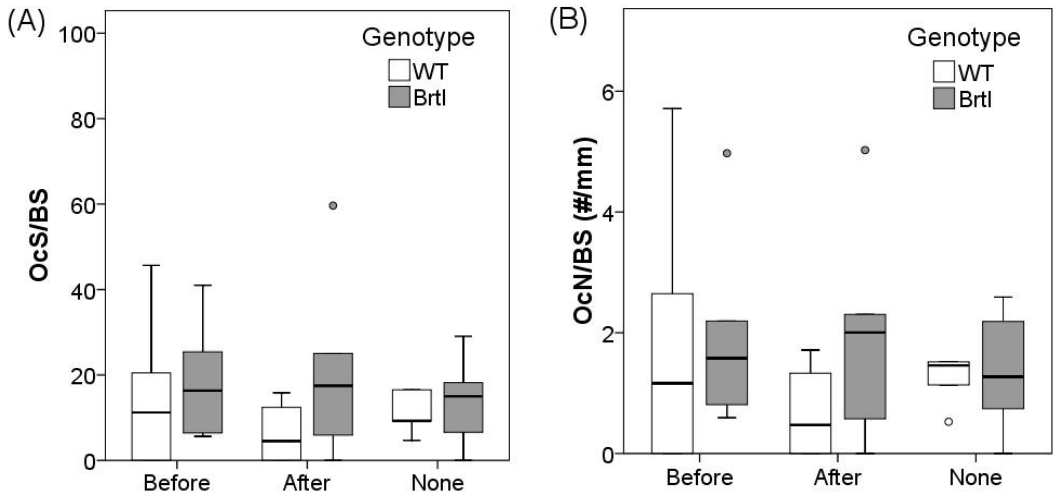

Figure 24: TRAP Histomorphometry results.

The results are presented as boxplots for osteoclast surface per bone surface (A) and osteoclast number per bone surface (B).

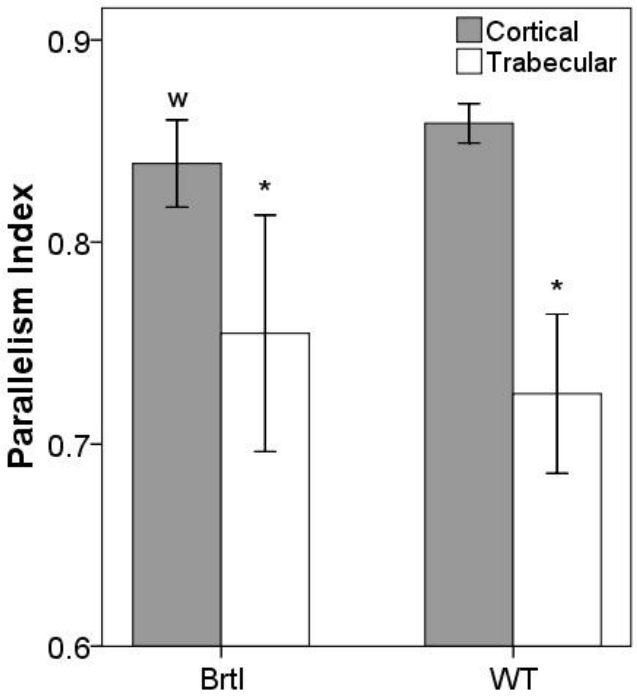

Figure 25: Parallelism Index results for polarized light analysis.

Results are shown as mean ± one standard deviation. Notations indicate significance with respect to the cortical bone within a genotype (*; $p<0.05$). For the cortical bone, there is a also a trend toward a difference between the genotypes (w; $p = 0.072$).

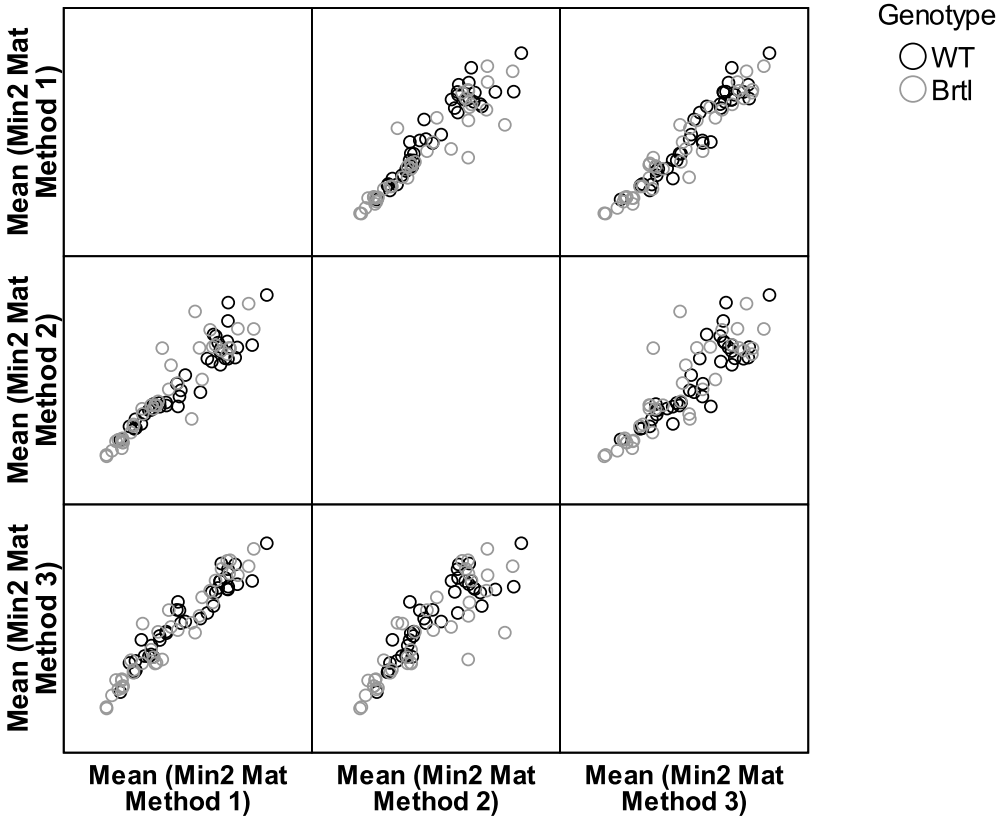

Figure 26: Comparisons of the mineral:matrix ratio calculations used in this study.

This graph shows scatterplots of the mineral to matrix ratios tested. Method 1 normalized to the area of the hydroxyproline and proline bands. Method 2 normalized to the height of the CH2 wag peak. Method 3 normalized to the area under the Amide I band.

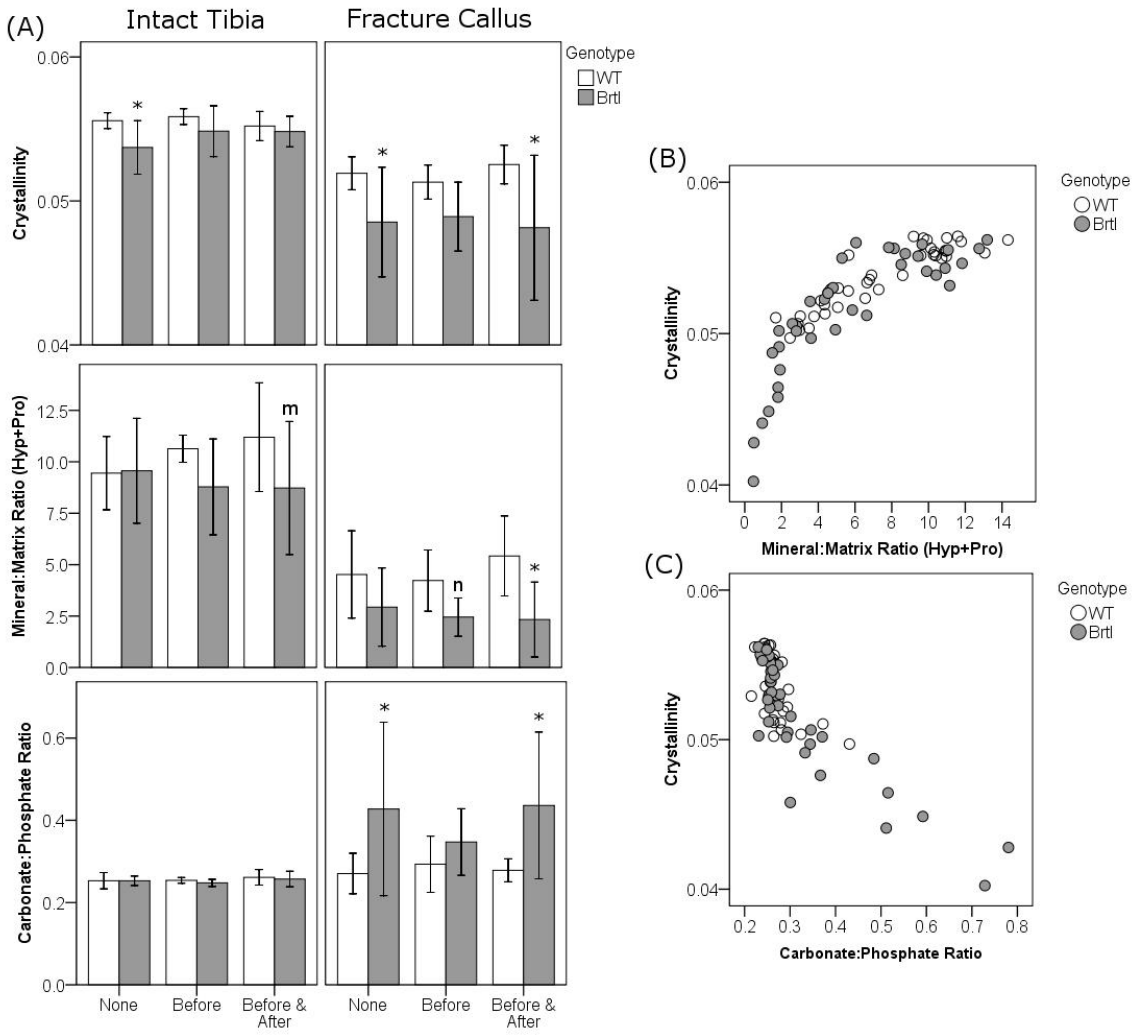

Figure 27: Raman microspectroscopy results for the Brtl/+ fracture healing study. This figure shows the results for (A) crystallinity, mineral to matrix ratio and carbonate to phosphate ratio. Crystallinity was then plotted against the mineral to matrix ratio (B) or the crystallinity (C). Results for (A) are presented as mean ± one standard deviation. Notations indicate significance with respect to genotype (*;$p<0.05$). There were also trends toward changes in the genotype (m; $p=0.076$ and n; $p=0.075$)

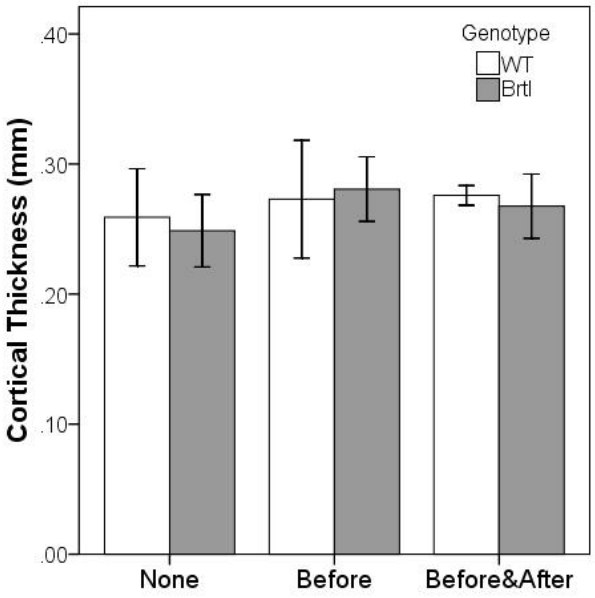

Figure 28: Cortical Thickness measurements for intact tibiae from 1w mice.

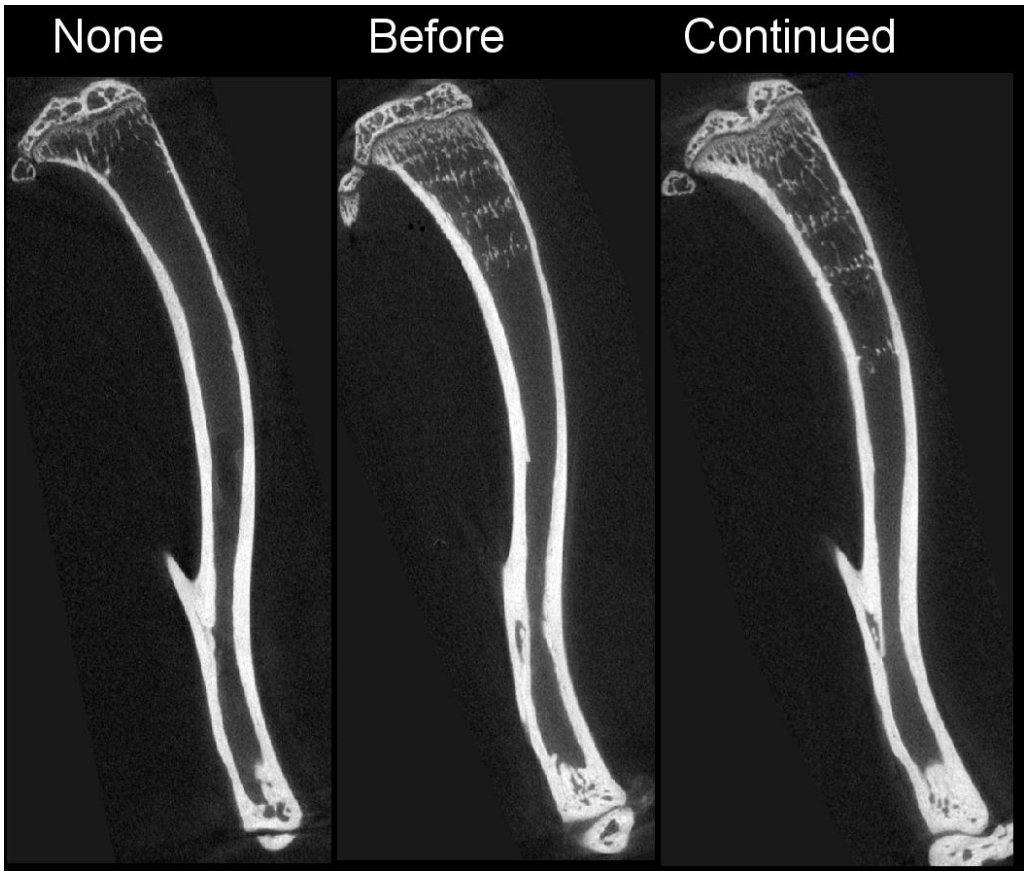

Figure 29: Representative µCT sections from intact tibiae of mice which healed for 1w.

Table 6: Fracture complexity incidence in the closed tibial fracture model.

Fracture Type	WT (n=150)	Brtl (n=135)	Total
Simple	61.3%	73.3%	67.0%
Wedge	12.7%	11.1%	11.9%
Complex	22.7%	12.6%	17.9%
Unknown	3.3%	3.0%	3.2%

Table 7: Statistical ANCOVA models used to analyze μCT and biomechanical data.

Assay	Variable	Limb/Tissue	Adj R^2	Model
Torsion Testing	Stiffness	Fx	0.617	Tx + Time + Genotype + Xray + Gage + Weight + Genotype * Xray + Time * Genotype + Tx * Genotype + Time * Xray + Xray * Weight + Tx * Time + Tx * Time * Genotype
		Intact	0.259	Tx + Time + Genotype + Weight + Gage + Time * Genotype
	Torque	Fx	0.731	Tx + Time + Genotype + Xray + Gage + Weight + Genotype * Xray + Time * Genotype + Tx * Genotype + Genotype * Weight + Time * Xray + Tx * Xray + Xray * Weight + Tx * Time + Time * Weight
		Intact	0.456	Tx + Time + Genotype + Weight + Tx * Time
	Angular Disp.	Fx	0.354	Tx + Time + Genotype + Xray + Weight + Gage + Tx * Genotype + Genotype * Weight + Tx * Xray + Tx * Time + Time * Weight + Tx * Weight + Tx * Time * Weight
		Intact	0.173	Tx + Time + Genotype + Weight + Gage
	Energy	Fx	0.502	Tx + Time + Genotype + Xray + Weight + Gage + Time * Genotype + Tx * Genotype + Time * Xray + Tx * Time + Tx * Weight + Time * Weight + Xray * Weight + Tx * Xray
		Intact	0.274	Tx + Time + Genotype + Weight + Gage + Tx * Time
μCT	BVF	Callus	0.525	Tx + Time + Genotype + Xray + Weight + Time * Xray + Tx * Time
	Volume	Callus	0.225	Tx + Time + Genotype + Xray + Weight + Time * Genotype + Genotype * Weight + Tx * Time
	TMD	Callus	0.633	Tx + Time + Genotype + Xray + Weight + Genotype * Xray + Time * Xray
		Fx Cortical	0.075	Tx + Time + Genotype + Xray + Weight + Genotype * Weight + Time * Xray + Tx * Genotype + Tx * Xray

Table 8: Means and standard deviations for the μCT results.

			Alendronate Treatment											
			None				Before				Continued			
			n	(mean)	±	(sd)	n	(mean)	±	(sd)	n	(mean)	±	(sd)
2w	WT	Cortical TMD (mg/cc)	13	1110.7	±	28.7	13	1135.8	±	42.9	18	1115.3	±	51.2
		Callus TMD (mg/cc)	13	503.8	±	28.8	13	515.5	±	35.3	18	500.8	±	27.7
		Callus BMD (mg/cc)	13	312.5	±	30.3	13	309.6	±	42.4	18	309.9	±	43.0
		Callus Vol. (mm^3)	13	37.31	±	7.24	13	27.48	±	11.97	18	33.36	±	8.78
		Callus BVF	13	0.400	±	0.057	13	0.394	±	0.084	18	0.414	±	0.091
		Vol. of Bone (mm^3)	13	14.66	±	2.62	13	10.75	±	4.71	18	13.87	±	5.33
	Brtl/+	Cortical TMD (mg/cc)	12	1133.0	±	45.0	9	1098.5	±	28.8	12	1124.8	±	19.4
		Callus TMD (mg/cc)	12	511.8	±	31.6	9	478.3	±	72.9	12	513.7	±	18.1
		Callus BMD (mg/cc)	12	345.7	±	53.1	9	307.8	±	66.3	12	302.0	±	48.1
		Callus Vol. (mm^3)	12	23.42	±	9.11	9	25.19	±	8.50	12	32.59	±	10.60
		Callus BVF	12	0.468	±	0.101	9	0.437	±	0.097	12	0.387	±	0.108
		Vol. of Bone (mm^3)	12	10.92	±	4.05	9	11.43	±	5.96	12	12.22	±	4.30
3w	WT	Cortical TMD (mg/cc)	12	1091.8	±	26.0	17	1127.8	±	51.7	13	1106.1	±	29.5
		Callus TMD (mg/cc)	13	597.5	±	70.1	18	620.6	±	124.3	13	578.6	±	55.7
		Callus BMD (mg/cc)	13	433.5	±	79.1	18	489.8	±	164.8	13	460.5	±	66.9
		Callus Vol. (mm^3)	13	33.85	±	16.93	18	25.94	±	7.97	13	26.88	±	8.72
		Callus BVF	13	0.591	±	0.099	18	0.657	±	0.135	13	0.675	±	0.094
		Vol. of Bone (mm^3)	13	19.21	±	8.92	18	16.53	±	4.89	13	17.75	±	4.79
	Brtl/+	Cortical TMD (mg/cc)	14	1110.5	±	45.5	14	1136.8	±	26.1	14	1121.9	±	42.6
		Callus TMD (mg/cc)	14	596.8	±	43.8	14	597.0	±	35.7	14	581.6	±	40.3
		Callus BMD (mg/cc)	14	406.4	±	55.3	14	411.1	±	69.9	14	452.8	±	69.8
		Callus Vol. (mm^3)	14	25.60	±	8.88	14	29.20	±	8.69	14	28.47	±	10.46
		Callus BVF	14	0.538	±	0.082	14	0.540	±	0.122	14	0.656	±	0.128
		Vol. of Bone (mm^3)	14	13.69	±	5.07	14	15.30	±	4.89	14	17.87	±	5.70
5w	WT	Cortical TMD (mg/cc)	14	1136.4	±	43.1	14	1144.3	±	36.0	16	1131.1	±	52.2
		Callus TMD (mg/cc)	15	721.0	±	144.2	14	712.7	±	42.4	16	685.1	±	53.8
		Callus BMD (mg/cc)	15	505.6	±	197.5	14	500.7	±	56.1	16	564.3	±	84.8
		Callus Vol. (mm^3)	15	18.50	±	9.68	14	21.59	±	7.81	16	28.96	±	10.38
		Callus BVF	15	0.580	±	0.166	14	0.593	±	0.075	16	0.734	±	0.099
		Vol. of Bone (mm^3)	15	9.76	±	3.96	14	12.58	±	4.25	16	20.77	±	6.45
	Brtl/+	Cortical TMD (mg/cc)	12	1130.3	±	41.5	13	1148.7	±	36.3	14	1139.0	±	45.0
		Callus TMD (mg/cc)	12	709.9	±	59.1	13	703.4	±	41.7	14	697.3	±	51.8
		Callus BMD (mg/cc)	12	439.8	±	72.8	13	491.7	±	57.7	14	566.5	±	73.4
		Callus Vol. (mm^3)	12	25.05	±	11.50	13	19.83	±	6.98	14	27.23	±	6.89
		Callus BVF	12	0.504	±	0.069	13	0.588	±	0.077	14	0.723	±	0.082
		Vol. of Bone (mm^3)	12	12.03	±	4.15	13	11.46	±	3.75	14	19.40	±	4.48

Table 9: Biomechanical Data For the Fracture Callus.

				Alendronate Treatment					
				None		Before		Continued	
				n	(mean) ± (sd)	n	(mean) ± (sd)	n	(mean) ± (sd)
Fracture Callus	2	WT	Stiffness	5	0.099 ± 0.095	5	0.060 ± 0.052	8	0.168 ± 0.168
			Angular Disp.	5	52.6 ± 17.3	5	42.9 ± 18.1	8	30.0 ± 17.5
			Torque at Failure	5	2.9 ± 2.0	5	1.9 ± 0.9	8	3.8 ± 3.3
			Energy to Failure	5	82.9 ± 22.9	5	50.0 ± 41.0	8	68.6 ± 55.0
		Brtl/+	K	8	0.108 ± 0.059	7	0.159 ± 0.133	6	0.153 ± 0.121
			Angular Disp.	8	29.8 ± 19.7	7	40.4 ± 25.7	6	29.1 ± 11.3
			Torque at Failure	8	2.6 ± 1.7	7	2.7 ± 1.8	6	3.5 ± 2.9
			Energy to Failure	8	57.9 ± 51.9	7	79.3 ± 84.7	6	63.8 ± 62.6
	3	WT	Stiffness	7	1.564 ± 0.649	9	1.338 ± 0.630	4	0.842 ± 0.298
			Angular Disp.	7	18.1 ± 11.0	9	17.4 ± 7.1	4	34.7 ± 16.1
			Torque at Failure	7	18.8 ± 6.3	9	16.3 ± 5.6	4	17.1 ± 7.9
			Energy to Failure	7	227.0 ± 182.8	9	180.6 ± 85.6	4	320.1 ± 161.3
		Brtl/+	Stiffness	10	0.729 ± 0.338	6	0.731 ± 0.184	8	0.828 ± 0.277
			Angular Disp.	10	20.4 ± 6.6	6	24.4 ± 13.2	8	18.9 ± 5.7
			Torque at Failure	10	11.2 ± 3.9	6	13.3 ± 4.0	8	12.8 ± 4.3
			Energy to Failure	10	136.3 ± 58.7	6	183.3 ± 89.4	8	136.0 ± 53.9
	5	WT	Stiffness	9	0.899 ± 0.347	8	1.012 ± 0.706	12	1.698 ± 0.699
			Angular Disp.	9	29.6 ± 18.9	8	22.3 ± 11.6	12	25.3 ± 17.3
			Torque at Failure	9	17.9 ± 3.2	8	15.2 ± 8.7	12	25.1 ± 7.4
			Energy to Failure	9	303.5 ± 223.7	8	200.6 ± 125.0	12	342.3 ± 191.9
		Brtl/+	Stiffness	7	1.198 ± 0.451	10	1.255 ± 0.526	7	1.358 ± 0.652
			Angular Disp.	7	20.9 ± 6.1	10	18.7 ± 7.3	7	25.3 ± 9.0
			Torque at Failure	7	20.2 ± 6.9	10	18.0 ± 5.6	7	23.9 ± 7.7
			Energy to Failure	7	263.3 ± 128.1	10	193.6 ± 84.7	7	355.0 ± 169.7

Table 10: Biomechanical Data for the Intact Tibia.

				Alendronate Treatment					
				None		Before		Continued	
				n	(mean) ± (sd)	n	(mean) ± (sd)	n	(mean) ± (sd)
Intact Tibia	2	WT	Stiffness	9	0.851 ± 0.325	12	1.078 ± 0.428	12	1.064 ± 0.336
			Angular Disp.	9	22.6 ± 5.2	12	23.6 ± 10.2	12	23.8 ± 9.1
			Torque at Failure	9	16.6 ± 4.5	12	18.7 ± 3.4	12	18.8 ± 3.7
			Energy to Failure	9	216.8 ± 84.8	12	256.6 ± 111.8	12	275.2 ± 136.5
		Brtl/+	Stiffness	9	0.848 ± 0.238	6	0.906 ± 0.227	7	1.073 ± 0.594
			Angular Disp.	9	20.7 ± 7.3	6	21.3 ± 7.7	7	19.4 ± 12.2
			Torque at Failure	9	15.4 ± 3.4	6	16.2 ± 4.9	7	15.0 ± 4.3
			Energy to Failure	9	179.3 ± 81.4	6	205.6 ± 118.1	7	156.1 ± 94.3
	3	WT	Stiffness		1.245 ± 0.252	12	1.081 ± 0.312	7	1.352 ± 0.296
			Angular Disp.		17.0 ± 4.4	12	22.9 ± 7.7	7	17.7 ± 5.0
			Torque at Failure		19.8 ± 5.0	12	19.6 ± 3.6	7	18.8 ± 3.4
			Energy to Failure		203.8 ± 104.2	12	262.9 ± 87.3	7	215.1 ± 78.3
		Brtl/+	Stiffness	10	0.718 ± 0.271	6	1.079 ± 0.308	9	0.985 ± 0.140
			Angular Disp.	10	19.0 ± 7.7	6	17.9 ± 11.0	9	16.0 ± 3.8
			Torque at Failure	10	12.1 ± 3.4	6	15.7 ± 4.2	9	15.2 ± 1.3
			Energy to Failure	10	130.1 ± 64.3	6	180.9 ± 144.5	9	138.9 ± 36.3
	5	WT	Stiffness	8	0.875 ± 0.195	9	1.054 ± 0.405	14	1.150 ± 0.302
			Angular Disp.	8	23.7 ± 7.4	9	22.6 ± 6.1	14	23.7 ± 8.3
			Torque at Failure	8	16.8 ± 2.9	9	19.8 ± 4.7	14	21.5 ± 3.2
			Energy to Failure	8	242.9 ± 109.1	9	241.8 ± 83.1	14	286.5 ± 112.3
		Brtl/+	Stiffness	9	0.914 ± 0.436	10	1.254 ± 0.493	9	1.395 ± 0.717
			Angular Disp.	9	16.4 ± 6.9	10	14.2 ± 7.2	9	19.3 ± 7.7
			Torque at Failure	9	11.9 ± 4.6	10	14.3 ± 1.9	9	20.4 ± 3.6
			Energy to Failure	9	116.8 ± 73.0	10	116.8 ± 58.8	9	205.7 ± 74.6

Table 11: Table of Intraclass Correlation Coefficients for Raman Microspectroscopy

Metric	***Intraclass Correlation Coefficient***	
	Intact Tibia	Fracture Callus
Mineral To Matrix Ratio (Method 1)	*0.759*	*0.654*
Mineral To Matrix Ratio (Method 2)	*0.515*	*0.631*
Mineral To Matrix Ratio (Method 3)	*0.748*	*0.657*
Crystallinity	*0.514*	*0.608*
Cross-Linking Ratio	*0.313*	*0.294*
Carbonate to Phosphate Ratio	*0.595*	*0.709*

CHAPTER 4: Healing of undemineralized and demineralized structural bone allografts with an ECM alteration in a critical sized murine segmental defect

Introduction

Bone healing and regeneration is a substantial clinical problem. Most closed fractures are treated with reduction and immobilization and heal naturally. Many fractures, though, still become problematic. These fractures at risk may be open, infected, comminuted, inadequately immobilized, large, have a lack of soft tissue coverage, or have poor vascularity.[1,2] These fractures also have an increased risk of delayed healing and/or subsequent non-union leading to significant clinical problems. Non-unions require surgical intervention to try to promote healing, although bone morphogenetic proteins (BMPs) have recently shown success in treating these conditions.[3,4] However, clinical studies indicate that the success rate is variable,[5] and BMPs cannot overcome the significant segmental bone loss that occurs in cases of trauma or tumor resection. These situations require bone substitutes to facilitate the healing process.

A large number of synthetic and natural biomaterials have been investigated to fill this need for bone substitutes in these clinical situations and to promote regeneration in fusion procedures. The materials can be based on polymers, ceramics, or naturally occurring matrices and serve as structural substitutes or as carriers for osteogenic factors and/or cells. Many different substitutes may ultimately be needed for the wide array of potential clinical applications. Therefore, previous studies have investigated design variables such as material composition, surface chemistry, porosity, mechanical properties and scaffold structure in a search for materials which are osteopromoting and functional. A few options are now available and are appealing due to their reproducibility, lack of immunogenicity and potential for large supply. Despite this, the largest source of materials used to fill defects and promote healing is bone grafts. Autografts, often extracted from the iliac crest, are considered to be the gold standard. However, allografts are frequently obtained from local bone banks or from commercial vendors, particularly for use in large defects.

The most significant problem that can arise with the use of allografts is a failure to revitalize through remodeling and replacement by normal bone. This often leads to long term mechanical failure. These failures can be related to an increase in microcrack density over time that causes a decrease in graft strength.[6] As a result, many studies have investigated methods to improve graft healing using primate, ovine, caprine, canine, rabbit and rodent models. The large animal models are well suited to advanced pre-clinical studies, although

rodent models are particularly appealing due to their low cost and the availability of transgenic animals.

Murine models of segmental defects have been developed that use locking nails, pin-clip devices, intramedullary screws, locking plates, compliant locking plates, intramedullary nails and external fixators.[9,10] The only model available to study murine structural allografts uses an intramedullary pin to stabilize a femoral graft.[11] This model has been used extensively to investigate allografts, autografts and isografts.[12-17] Those results indicate that live grafts (either autografts or isografts) inherently heal better than devitalized allografts. This may be related to the vascular nature of live grafts that results in peripheral callus formation similar to a reduced fracture. Efforts to improve healing of devitalized structural allografts have included coating the grafts with bone marrow stromal cells (BMSCs) with BMP2 to simulate the periosteum and recombinant adeno-associated virus (rAAV) containing RANKL, VEGF, or constitutively active activin receptor like kinase-2 (caALK2).[12,13,18] All of these may be effective. BMP2 coating induced more bone formation and vasculature,[17] and engrafting BMP2 producing MSCs onto allografts increase the amount of bone and ultimate torque.[16] When rAAV-caALK2 was used to induce similar signals, the grafts revascularized and had osteoclast activity early.[13] Resorption and revascularization are coupled processes, [19] and both rAAV-RANKL combined with rAAV-VEGF induced resorption and revascularization of the graft although neither was sufficient alone.[12]

This resorption is a critical part of the healing process and is essential for long term healing. Resorption may vary with different substitute designs, although the mechanism may depend on how the specific resorption processes are affected. Resorption occurs when an osteoclast binds to the bone matrix, forms a sealing zone, and creates a low pH environment with proteases to remove both the organic and inorganic components of bone. Binding of chicken osteoclasts to bone is related to interactions between the αvβ3 integrin and ostepontin (OPN),[20] a non-collagenous protein present in the extracellular matrix between collagen fibrils.[21] Osteopontin deficient mice have a decreased ruffled border volume,[22] as well as larger calluses late in the remodeling phase of fracture healing.[23] Taken together, these data imply that alterations in an ECM protein can have a significant impact on matrix resorption.

It is critical to consider the osteoclast interactions with bone substitute materials, particularly as biomimetic scaffolds attempt to recapitulate the bone matrix ultrastructure.[24] The purpose of this study was to investigate the resorption of structural allografts with an altered collagenous extracellular matrix in a critical sized murine defect. As will be described, grafts from the Brtl/+ animal model of osteogenesis imperfecta (OI) were utilized. Brtl/+ mice have a single point mutation in the gene encoding type I collagen that results in a cortical bone phenotype with an increased mineral to matrix ratio, decreased structural biomechanical properties,[25] an increase in osteoclast surface per bone surface,[26], a change in collagen fibril size and intrafibrillar spacing,[27,28] and a possible decrease in collagen organization (see previous chapter). Because

this bone phenotype has both organic and inorganic alterations, some grafts were demineralized to decouple this effect and directly investigate the matrix. Demineralized bone grafts must be implanted into a biomechanically stable environment, so the first goal of this study was to develop a unique internal fixation system of biomechanically stable critical size defect in a mouse femur. The second goal of the study was to evaluate the influence of graft ECM organization and composition on allograft healing to test the hypothesis that the ECM alterations in a Brtl/+ graft would result in increased matrix resorption. Bone from OI patients would not be used as a structural allograft in a clinical scenario, but these results may provide insight into mechanisms that govern matrix resorption and functional healing.

Methods

Study Design

Structural femoral allografts were harvested from female Brtl/+ mice and their WT counterparts as close as possible to 4 months of age. These grafts were processed, sterilized, and frozen. On the day of surgery, grafts were thawed and reimplanted into male WT mice at approximately 4 months of age. The animals were allowed to heal for 10 weeks. Based on previously published data using an intramedullary nail data showing functional biomechanical healing at 9 weeks,[14] and initial radiographs, this was estimated to be long enough for union of the host and graft. To understand intra- versus inter-animal variation, and to minimize the number of host animals needed for the study, some mice

received bilateral grafts and some mice received unilateral grafts. A total of 96 mice were enrolled in the study. An exclusive donor-host pairing was used as frequently as possible. Three mice did not receive a graft to verify that non-unions would occur, and two mice which received demineralized grafts were allowed to heal for 150 days as a pilot study to determine how much better the demineralized grafts would heal with more time. All experiments were performed under approval of the University of Michigan IACUC.

Graft harvest and prep

Immediately after euthanization, the hind limbs of donor animals were shaved and cleaned with chlorhexadine solution. The femurs were harvested and stripped of soft tissue under aseptic conditions. The proximal end of the femur was removed and the marrow was flushed. Using a custom dremel tool with two circular saw blades separated by a 1.5 mm spacer, a notch was cut in the femoral mid diaphysis. Each cut was finished with a single circular saw blade using fine hand control. The graft was then placed in a clean 1.5 mL vial in sterile PBS until further processing.

To obtain an initial image of the grafts and ensure that no damage was done during processing, the grafts were then placed in a custom holder in PBS and scanned using a commercially available μCT system (eXplore Locus SP, GE Healthcare preclinical imaging). Seven grafts, stacked two rows high, were scanned simultaneously to improve throughput. While the x-ray beam was attenuated by two grafts in this setup, previous work indicated that this did not

bias accuracy.[29] The scan protocol utilized 720 views over 360° to ensure that all grafts received an equal exposure. A 0.5 mm Al filter was used to remove the lowest energy photons and an exposure of 144 mA*s was used to get adequate photon statistics at the detector when using 2x2 binning. The images were reconstructed using an isotropic voxel size of 15 μm.

The grafts that were randomly assigned for demineralization were placed in EDTA. Undemineralized grafts were left in sterile PBS. After 24 hours, the demineralization was verified by performing another μCT scan using 200 views over 200° of rotation. An exposure of 52.8 mA*s was adequate to obtain a good exposure with 4x4 detector binning. All of the grafts were sterilized in 70% ethanol for a minimum of 2 hours. In a sterile environment, the grafts were then rinsed and placed in vials with sterile PBS. These vials were frozen at -20 °C and left until needed for implantation.

Surgical Model

A custom titanium internal fixator was designed for this study (Figure 30). The fixator design included four counter-bored holes for screws, pads on the bottom to facilitate firm positioning on the femur while providing space for healing under the plate, a slot on the superior surface for a custom clamp used intraoperatively for fixator stabilization, and a necked down center portion to provide a region for viewing the femur during subsequent defect creation. Mice were anesthetized using isofluorane, shaved, and sterilized with chlorhexadine to prepare for surgery (Figure 31A). In a sterile procedure, an anterolateral

approach was used to expose the anterior surface of the femur. The periosteum was cut and elevated and the internal fixation plate was positioned on the anterior portion of the femur (Figure 31B). Bi-cortical flat fillister head stainless steel self tapping 000 x 5/32” screws (JI Morris) were inserted after pre-drilling using a high speed micro-drill (18000-17, Fine Science tools) and #74 drill bit. The defect was then created in the femoral mid-diaphysis using a 1.0 mm dental burr to match the graft size (Figure 31C). The defect was flushed with sterile saline as needed and the graft was placed in the gap (Figure 31D). After a brief period of coagulation, the muscle and fascial layers were closed using a 6-0 suture and the skin was closed using tissue glue. Mice recovered under a heat lamp and were given access to moist chow after recovery. Intraoperative pain was managed using 0.05 mg/kg buprenorphine after application of anesthesia. Post-op pain was treated with one subcutaneous injection of 5 mg/kg of carprofen, another injection of buprenorphine 8 hours later, followed by carprofen injections as needed.

Radiographic Assessment

Mice were followed radiographically during healing and an ordinal scoring system was developed to assess this healing. The radiographic appearance of healing with a demineralized graft is quite different than an undemineralized graft, so separate scoring systems were needed. Undemineralized grafts heal by bridging between the host and graft cortical bone, so the amount of bridging was estimated. Demineralized grafts healed in a radiographically diffuse fashion so a

previously reporting scoring scheme was adapted.[30] This scoring system is represented schematically in Figure 32 and descriptions of each score are in Table 12.

μCT

The subtleties of healing were difficult to assess on planar radiographs so every bone was scanned using a commercially available μCT system (eXplore Locus SP, GE Healthcare). It would be preferable to remove the titanium fixator and stainless steel screws to avoid image artifacts, but this was not done to avoid damage to the regenerating tissue. Instead, each leg was scanned in a vertical position with the fixator intact and a 0.025 mm Al / 0.025 mm Cu filter was used to minimize beam hardening artifacts. 720 views were used over 360° of sample rotation, the source voltage was kept at 80 kVp, and 126 mA*s were used with 4x4 detector binning to obtain adequate photon statistics at the detector.

Images of the femurs after healing were reformatted to align the long axis of the bone with the longitudinal axis of the image. To analyze the amount of new bone formation in limbs which received demineralized grafts, the only mineralized tissue in the gap was new bone formation. Therefore, a 1.5x1.5x1.5 mm region of interest was placed in the center of the gap. A global threshold was applied and the amount of new bone formation was estimated. To analyze images of the femurs which received undemineralized grafts, an image registration approach was used to delineate new bone formation from voxels that were present in the original graft. Using a minimum of 4 sets of control points, the image of the graft

after harvest was registered with the image of the femur after healing using 6 degrees of freedom to account for changes in translation and rotation. This allowed a direct measurement of the number of remaining bone voxels in the space originally containing the bone graft and an estimate of the new bone formation.

Torsion testing

Torsion testing was used to assess the biomechanical properties of the healing tissue. A subset of limbs was potted with the fixator still intact using low melting temperature alloy. The potted bones were placed in a custom miniature torsion tester,[31] and a mill was used to remove the middle portion of the fixator. The bones were wetted with lactated ringer's solution (LRS) and tested in torsion until failure or, in the cases where no apparent loading occurred, until the test was stopped.

Histology

A subset of graft limbs were analyzed histologically. The femurs were fixed in 10% NBF for a period of 24 hours, demineralized and embedded in paraffin. The fixators were removed and 7 μm sections were obtained. Slides were stained with hematoxylin and eosin to look at the basic nature of the tissue, Masson's trichrome to highlight the soft tissue, or Safranin-O with fast green and hematoxylin counterstains to assess cartilage. A subset of slides was also stained with TRAP (KT-008, Kamiya Biomedical Company, Seattle, WA) to

assess osteoclast activity. To categorize the type of tissue formation, these slides were viewed under standard light microscopy. A minimum of two slides, representing two different locations within the healing area, were assessed for each bone. When no bone bridging occurred, the tissue was categorized as fibrous, cartilage, or marrow.

Results

Model results & complication rate

An internal fixator was successfully designed and a procedure was developed for implantation on the anterior mouse femur. A total of 96 mice were enrolled into the study. 16 mice were euthanized intraoperatively because of femoral fractures during insertion of the screws. 11 mice were euthanized very early during healing because of stress and/or radiographic signs of failure. Of the remaining 69 mice, 2 with demineralized grafts from WT hosts (one unilateral, one bilateral) were allowed to heal for 150 days as a pilot study to determine the potential for healing and regeneration after a long healing interval. The remaining 64 mice were euthanized between 69 and 77 days of healing. The breakdown of these mice by study group is reported in Table 13. There were no noticeable instances of fixator failure or signs of infection at harvest. To verify that the gap size used in this study was a critical sized defect, three animals did not receive any grafts; the resulting gaps had not evidence of bony healing and only contained fibrous tissue (Figure 33).

Planar radiography

Two independent reviewers scored the planar radiographs based on a schematic scoring system. The results indicated a substantial variability in the amount of healing between animals. There was also a substantial difference between the reviewers due to the difficulty in assessing healing between the fixator and underlying bone (Figure 34). For the animals which did not heal, there was evidence of possible resorption of the host cortices that was similar to the non-union cases. Very few animals healed enough to show restoration of the cortical bone structure, but some animals still had three or four cortices integrated (Figure 34). In these cases, there was diffuse mineral formation in the demineralized graft groups and bridging of the host cortical bone to the graft in the gaps filled with undemineralized grafts.

Torsion results & success rate

A subset of the bones with good radiographic healing was scanned with a μCT system prior to torsion testing. This ensured that the radiographic readings were not biased by aspects of the three-dimensional morphologic structure. Some of the bones with visible healing on the μCT images were potted and tested in torsion. Only 7 of the 18 bones tested had meaningful load displacement curves. This low success rate precluded the ability to statistically compare the functional healing between the tissues so the remaining bones initially assigned for torsion testing were reassigned for histological analysis.

μCT

In light of the radiographic variability and lack of biomechanical function, μCT images were analyzed to gain more insight into the model itself. In the first analysis, the amount of new bone formation in animals which received demineralized grafts bilaterally was measured. A paired analysis of the two limbs indicated that, for the 7 animals which received demineralized grafts bilaterally, the median difference in bone volume fraction was 4.51% with a range spanning between 1.74% and 19.16% (Figure 35A). A similar analysis was performed for mice with bilateral undemineralized grafts. In these cases, image registration was used to assess the amount of bone loss in the grafts. This analysis showed the variability between the limbs, and indicated regions of graft resorption (Figure 36). However, in animals which received undemineralized grafts bilaterally, the results were not consistent between the two limbs. The median difference within an animal was 4.05% with a range spanning between 1.28% and 18.26% (Figure 35B).

Histological assessment

To investigate the variability in healing within a limb, a subset of samples were assessed histologically. As expected, lacunae in the bone grafts were completely acellular. Due to the 2-dimensional limitations of histologic sectioning, several slides per sample were examined. In contrast to μCT imaging, both demineralized and undemineralized grafts could be visualized so the integration between the cortices of the host and graft bone at the proximal medial, proximal

lateral, distal medial and distal lateral quadrants were examined. If more than half of the sections examined had a direct bone bridge in each quadrant, the graft was assumed to be healed at that location. The results indicated that there was a large distribution in the number of cortices that healed within a graft limb (Figure 37). Most of the unhealed interfaces contained fibrous tissue (Figure 38, Table 14). Some sections appeared to have marrow at the interface but had not formed a bony junction. A small number of sections had hypertrophic chondrocytes that contained proteoglycans when stained with Safranin-O.

Several sections stained with Masson's trichrome appeared to have viable tissue within the graft. Many of the undemineralized grafts contained colorations consistent with revitalization irresepective of a bony union. Similar coloration and revitalization was also seen in the demineralized grafts. Visualizing these revitalized demineralized sections in conjunction with μCT images indicated that these areas of revitalization contained bone mineral and were actively healing (Figure 38, Table 15). In some cases, this biologically active area was directly juxtaposed to areas of the graft which appear to be acellular.

Discussion

The first goal of this study was to develop a biomechanically stable critical defect model in the mouse femur. This system, based on a unique internal fixator, provided a stable environment for healing of a critical sized defect that resulted in a non-union when no graft was implanted. The main hypothesis of this study was that undemineralized and demineralized grafts from Brtl/+ mice would

have an increased rate of resorption and decreased structural biomechanical properties after incorporation. While the study design allowed this question to be addressed, the sources of variability in the model system in conjunction with the challenging healing environment precluded the ability to directly test this hypothesis. Undemineralized grafts that healed showed radiographic bridging between the host bone and graft when healed. For demineralized grafts, the healing looks relatively diffuse on planar radiographs when it occurs. However, many grafts did not heal and had fibrous tissue at the host-graft interfaces, similar to previously reported graft failures.[32,33] The presence of soft tissue tissue at the sites of poor integration is consistent with the lack of mineral at these locations on the corresponding μCT images. Furthermore, even the grafts that appeared to be bridged did not have meaningful torque-displacement relationships, reinforcing the difficulty in restoring function.

The general lack of healing in this model is similar to the slow and/or poor healing rates seen with structural bone allografts as a clinical therapeutic. One possible cause is host rejection due to mismatches in the major histocompatability complex,[34,35] although this is difficult to assess in clinical settings.[36] However, this seems unlikely here because the inbred mouse strain should minimize immune incompatibilities. Furthermore, the grafts were all devitalized and frozen, and this should minimize the risks of immune rejection. Interestingly, many grafts had healing at some interfaces but not at others. This also suggests that the lack of healing is unrelated to rejection.

Failures at the host-graft interface may be due to inadequate reduction, misalignment, or mechanical instability at the interface.[32,36] All of these could be possible in this model. Graft alignment and positioning is a challenge due to the small size, especially for undemineralized grafts that are press-fit into the gap. Demineralized grafts, on the other hand, were compliant and could be squeezed into the gap. However, fibrous tissue formed around many of the interfaces in demineralized grafts so it seems plausible that the local mechanical environment may be a more prevalent factor in this model.

The local mechanical environment is critical for healing. In the presence of good vasculature,high levels of compression are more conducive to cartilage formation, high levels of tension and/or shear are more conducive to fibrous tissue formation and lower dilatational and/or shear strains are ideal for bone formation.[37] Many investigators have studied this both experimentally and computationally during healing.[38-44]. Notably, in murine internal fixation, flexible fixators resulted in a much larger callus with more woven bone and cartilage in comparison to rigid fixators.[9] The fixator used in this study was rigid enough to maintain a stable gap in the presence of a non-union, and there was direct intramembranous bone formation, indicating that the local strains in the healing environment may be relatively small. The few instances of cartilage formation may be linked to local instability because cartilage forms in unstable rodent healing models of healing where the fracture is treated with an intramedullary pin and non-rigid fixation.[13,31]

This inherent stability may also explain the response at different locations within the same graft. Bone has the ability to structurally adapt to biomechanical loads in relation to the strain history,[37] and the initial mechanical stability of a fracture gap may have functional implications later in healing.[42] This biological adaptation is a cell based response and, even though the grafts themselves are initially acellular, it is possible that cells recruited from the host during healing are able to exert this effect. Once stable areas form intramembranously and provide some stability to the graft structure as a whole, there may be less biomechanical incentive for healing at every portion of the host graft interface. Some of the μCT images show healing at one interface and extensive resorption at other areas, providing support for this concept. The rigidity of the internal fixator may also explain the evidence of cortical thinning that was seen in the cortical regions between the screws (Figure 36). Stiff fixators stabilize the gap but, as a result, may also result in some stress shielding and result in thinner cortical bone.[45]

In addition to the local mechanical environment, other factors may lead to the variability in healing. Many studies implicate the periosteum as a source of cells that aid healing. This is true in structural allografts and is a reason why live isografts heal better than devitalized allografts.[16,18] This advantageous response may be due to the osteogenic capability of these heterogeneous cell populations and their ability to promote vascularity. Structural allografts require revascularization to facilitate the healing process, and this can depend on the graft itself. Implantation of live bone grafts from COX2-/- mice into WT mice increases new vessel volume and bone formation in comparison to COX2-/-

hosts, but the response was more robust in WT mice which received WT grafts.[15] The devitalized grafts used in this study did not contain a live periosteum. Any periosteal progenitor cells would come from the host. Size limitations make it difficult to lift and replace the mouse periosteum after graft healing, possibly contributing to some of the variability in healing.

There are also other limitations in these experiments. The first limitation is that a new model was developed to address a scientific hypothesis but, as a result of this being the first experience with the model, it was challenging to get data supporting or contradicting the hypothesis. Devitalized structural allografts heal slowly, so it is possible that waiting for a longer healing time would have resulted in better functional integration. However, the temporal aspects of functional restoration are difficult to assess. One study indicates a large increase in ultimate torque between 6 weeks and 9 weeks,[14] although another study from the same group indicates that this increase occurs between 9 and 14 weeks. In this study, even when limbs with demineralized grafts were left for 150 days they still did not all heal (data not shown).

Another limitation is that graft revascularization was not directly assessed. It may be possible that the grafts that did not heal were not revascularized. However, vessel formation is coupled with resorption and the μCT images of undemineralized grafts indicate significant resorption. The last limitation is that the titanium fixator precludes μCT based bone mineral density measurements. It was possible to visualize the healing morphology even with this fixator, and the bones were aligned during so that images could still be interpreted, but there

were still significant beam hardening artifacts even in the graft region. Other studies have circumvented this by using radiolucent polymer fixators,[46] but this may be somewhat difficult to implement at this small scale.

The real value of this model system and study is the translational relevance. Many tissue engineered bone substitutes rely on a graft substitute that initially has low mechanical integrity. This system provides adequate biomechanical stability so that new substitutes based on this design principle can be studied. While it was difficult to test the basic science question of interest in this study, more experience with the model and other substitutes which can be custom molded to fit the gap better may provide insight in future experiments. Perhaps more importantly, this study demonstrated poor allograft incorporation in a murine critical defect model; a phenomena seen often in human patients with large allografts. As a result, it is a challenging healing model in a small animal.

In conclusion, this study represents an initial effort to develop a murine internal fixator system to understand how the extracellular matrix impacts structural graft healing. Use of the fixator in conjunction with a critical sized gap indicates that the gap is stable. Some portions of the graft integrate and form a bony union, whereas other portions of the graft resorb, and some form a fibrous non-union. All of these are consistent with clinical reports of graft healing and failure. Taken together, these results indicate that this model system can provide a challenging environment for healing constructs in an inexpensive animal model. As a result, it can also provide a more robust test of new technology than typical small animal models. Future experiments using other bone substitute materials,

improvements of the graft harvest techniques and implantation techniques, and studies which wait longer during healing, may provide valuable information to guide the design of tissue engineered bone substitutes.

References

1. Moucha, C.S.E., T.A. 2005. Bone Morphogenetic Proteins and Other Growth Factors to Enhance Fracture Healing and Treatment of Nonunions. In *Bone regeneration and repair: biology and clinical applications*. J.R. Lieberman, and G.E. Friedlaender, editors. Totowa, NJ: Humana Press. 169-194.
2. Taitsman, L.A., Lynch, J.R., Agel, J., Barei, D.P., and Nork, S.E. 2009. Risk Factors for Femoral Nonunion After Femoral Shaft Fracture. *J Trauma*.
3. White, A.P., Vaccaro, A.R., Hall, J.A., Whang, P.G., Friel, B.C., and McKee, M.D. 2007. Clinical applications of BMP-7/OP-1 in fractures, nonunions and spinal fusion. *Int Orthop* 31:735-741.
4. Jones, A.L., Bucholz, R.W., Bosse, M.J., Mirza, S.K., Lyon, T.R., Webb, L.X., Pollak, A.N., Golden, J.D., Valentin-Opran, A., and Group, B.M.P.E.i.S.f.T.T.-A.S. 2006. Recombinant human BMP-2 and allograft compared with autogenous bone graft for reconstruction of diaphyseal tibial fractures with cortical defects. A randomized, controlled trial. *J Bone Joint Surg Am* 88:1431-1441.
5. Starr, A.J. 2008. Fracture repair: successful advances, persistent problems, and the psychological burden of trauma. *J Bone Joint Surg Am* 90 Suppl 1:132-137.
6. Wheeler, D.L., and Enneking, W.F. 2005. Allograft bone decreases in strength in vivo over time. *Clin Orthop Relat Res*:36-42.
7. Manigrasso, M.B., and O'Connor, J.P. 2004. Characterization of a closed femur fracture model in mice. *J Orthop Trauma* 18:687-695.
8. Oetgen, M.E., Merrell, G.A., Troiano, N.W., Horowitz, M.C., and Kacena, M.A. 2008. Development of a femoral non-union model in the mouse. *Injury* 39:1119-1126.
9. Grongroft, I., Heil, P., Matthys, R., Lezuo, P., Tami, A., Perren, S., Montavon, P., and Ito, K. 2009. Fixation compliance in a mouse osteotomy model induces two different processes of bone healing but does not lead to delayed union. *J Biomech*.
10. Histing, T., Holstein, J.H., Garcia, P., Matthys, R., Kristen, A., Claes, L., Menger, M.D., and Pohlemann, T. 2009. Ex vivo analysis of rotational stiffness of different osteosynthesis techniques in mouse femur fracture. *J Orthop Res* 27:1152-1156.

11. Tiyapatanaputi, P., Rubery, P.T., Carmouche, J., Schwarz, E.M., O'Keefe R, J., and Zhang, X. 2004. A novel murine segmental femoral graft model. *J Orthop Res* 22:1254-1260.
12. Ito, H., Koefoed, M., Tiyapatanaputi, P., Gromov, K., Goater, J.J., Carmouche, J., Zhang, X., Rubery, P.T., Rabinowitz, J., Samulski, R.J., et al. 2005. Remodeling of cortical bone allografts mediated by adherent rAAV-RANKL and VEGF gene therapy. *Nat Med* 11:291-297.
13. Koefoed, M., Ito, H., Gromov, K., Reynolds, D.G., Awad, H.A., Rubery, P.T., Ulrich-Vinther, M., Soballe, K., Guldberg, R.E., Lin, A.S., et al. 2005. Biological effects of rAAV-caAlk2 coating on structural allograft healing. *Mol Ther* 12:212-218.
14. Reynolds, D.G., Hock, C., Shaikh, S., Jacobson, J., Zhang, X., Rubery, P.T., Beck, C.A., O'Keefe R, J., Lerner, A.L., Schwarz, E.M., et al. 2007. Micro-computed tomography prediction of biomechanical strength in murine structural bone grafts. *J Biomech* 40:3178-3186.
15. Xie, C., Ming, X., Wang, Q., Schwarz, E.M., Guldberg, R.E., O'Keefe, R.J., and Zhang, X. 2008. COX-2 from the injury milieu is critical for the initiation of periosteal progenitor cell mediated bone healing. *Bone* 43:1075-1083.
16. Xie, C., Reynolds, D., Awad, H., Rubery, P.T., Pelled, G., Gazit, D., Guldberg, R.E., Schwarz, E.M., O'Keefe, R.J., and Zhang, X. 2007. Structural bone allograft combined with genetically engineered mesenchymal stem cells as a novel platform for bone tissue engineering. *Tissue Eng* 13:435-445.
17. Zhang, X., Naik, A., Xie, C., Reynolds, D., Palmer, J., Lin, A., Awad, H., Guldberg, R., Schwarz, E., and O'Keefe, R. 2005. Periosteal stem cells are essential for bone revitalization and repair. *J Musculoskelet Neuronal Interact* 5:360-362.
18. Zhang, X., Xie, C., Lin, A.S., Ito, H., Awad, H., Lieberman, J.R., Rubery, P.T., Schwarz, E.M., O'Keefe, R.J., and Guldberg, R.E. 2005. Periosteal progenitor cell fate in segmental cortical bone graft transplantations: implications for functional tissue engineering. *J Bone Miner Res* 20:2124-2137.
19. Davy, D.T. 1999. Biomechanical issues in bone transplantation. *Orthop Clin North Am* 30:553-563.
20. Ross, F.P., Chappel, J., Alvarez, J.I., Sander, D., Butler, W.T., Farach-Carson, M.C., Mintz, K.A., Robey, P.G., Teitelbaum, S.L., and Cheresh, D.A. 1993. Interactions between the bone matrix proteins osteopontin and bone sialoprotein and the osteoclast integrin alpha v beta 3 potentiate bone resorption. *J Biol Chem* 268:9901-9907.
21. Nanci, A. 1999. Content and distribution of noncollagenous matrix proteins in bone and cementum: relationship to speed of formation and collagen packing density. *J Struct Biol* 126:256-269.
22. Franzen, A., Hultenby, K., Reinholt, F.P., Onnerfjord, P., and Heinegard, D. 2008. Altered osteoclast development and function in osteopontin deficient mice. *J Orthop Res* 26:721-728.

23. Duvall, C.L., Taylor, W.R., Weiss, D., Wojtowicz, A.M., and Guldberg, R.E. 2007. Impaired angiogenesis, early callus formation, and late stage remodeling in fracture healing of osteopontin-deficient mice. *Journal of Bone and Mineral Research* 22:286-297.
24. Sanchez, C., Arribart, H., and Guille, M.M. 2005. Biomimetism and bioinspiration as tools for the design of innovative materials and systems. *Nat Mater* 4:277-288.
25. Kozloff, K.M., Carden, A., Bergwitz, C., Forlino, A., Uveges, T.E., Morris, M.D., Marini, J.C., and Goldstein, S.A. 2004. Brittle IV mouse model for osteogenesis imperfecta IV demonstrates postpubertal adaptations to improve whole bone strength. *J Bone Miner Res* 19:614-622.
26. Uveges, T.E., Kozloff, K.M., Ty, J.M., Ledgard, F., Raggio, C.L., Gronowicz, G., Goldstein, S.A., and Marini, J.C. 2009. Alendronate treatment of the brtl osteogenesis imperfecta mouse improves femoral geometry and load response before fracture but decreases predicted material properties and has detrimental effects on osteoblasts and bone formation. *J Bone Miner Res* 24:849-859.
27. Uveges, T.E. 2007.
28. Wallace, J.M. 2009.
29. Meganck, J.A., Kozloff, K.M., Thornton, M.M., Broski, S.M., and Goldstein, S.A. 2009. Beam Hardening Artifacts in Micro-Computed Tomography Scanning can be Reduced by X-ray Beam Filtration and the Resulting Images can be used to Accurately Measure BMD. *Bone*.
30. Sciadini, M.F., Dawson, J.M., and Johnson, K.D. 1997. Bovine-derived bone protein as a bone graft substitute in a canine segmental defect model. *J Orthop Trauma* 11:496-508.
31. Taylor, D.K., Meganck, J.A., Terkhorn, S., Rajani, R., Naik, A., O'Keefe, R.J., Goldstein, S.A., and Hankenson, K.D. 2009. Thrombospondin-2 Influences the Proportion of Cartilage and Bone During Fracture Healing. *J Bone Miner Res*.
32. Enneking, W.F., and Campanacci, D.A. 2001. Retrieved human allografts : a clinicopathological study. *J Bone Joint Surg Am* 83-A:971-986.
33. Stevenson, S., Cunningham, N., Toth, J., Davy, D., and Reddi, A.H. 1994. The effect of osteogenin (a bone morphogenetic protein) on the formation of bone in orthotopic segmental defects in rats. *J Bone Joint Surg Am* 76:1676-1687.
34. Reikeras, O., Shegarfi, H., Naper, C., Reinholt, F.P., and Rolstad, B. 2008. Impact of MHC mismatch and freezing on bone graft incorporation: an experimental study in rats. *J Orthop Res* 26:925-931.
35. Stevenson, S., Li, X.Q., Davy, D.T., Klein, L., and Goldberg, V.M. 1997. Critical biological determinants of incorporation of non-vascularized cortical bone grafts. Quantification of a complex process and structure. *J Bone Joint Surg Am* 79:1-16.
36. Stevenson, S. 1999. Biology of bone grafts. *Orthop Clin North Am* 30:543-552.

37. Carter, D.R., and Beaupré, G.S. 2001. *Skeletal function and form : mechanobiology of skeletal development, aging, and regeneration*. Cambridge, UK ; New York, NY: Cambridge University Press. xii, 318 p. pp.
38. Cullinane, D.M., Salisbury, K.T., Alkhiary, Y., Eisenberg, S., Gerstenfeld, L., and Einhorn, T.A. 2003. Effects of the local mechanical environment on vertebrate tissue differentiation during repair: does repair recapitulate development? *J Exp Biol* 206:2459-2471.
39. Gardner, T.N., Stoll, T., Marks, L., Mishra, S., and Knothe Tate, M. 2000. The influence of mechanical stimulus on the pattern of tissue differentiation in a long bone fracture--an FEM study. *J Biomech* 33:415-425.
40. Isaksson, H., Wilson, W., van Donkelaar, C.C., Huiskes, R., and Ito, K. 2006. Comparison of biophysical stimuli for mechano-regulation of tissue differentiation during fracture healing. *J Biomech* 39:1507-1516.
41. Smith-Adaline, E.A., Volkman, S.K., Ignelzi, M.A., Jr., Slade, J., Platte, S., and Goldstein, S.A. 2004. Mechanical environment alters tissue formation patterns during fracture repair. *J Orthop Res* 22:1079-1085.
42. Klein, P., Schell, H., Streitparth, F., Heller, M., Kassi, J.P., Kandziora, F., Bragulla, H., Haas, N.P., and Duda, G.N. 2003. The initial phase of fracture healing is specifically sensitive to mechanical conditions. *J Orthop Res* 21:662-669.
43. Morgan, E.F., Longaker, M.T., and Carter, D.R. 2006. Relationships between tissue dilatation and differentiation in distraction osteogenesis. *Matrix Biol* 25:94-103.
44. Lacroix, D., Prendergast, P.J., Li, G., and Marsh, D. 2002. Biomechanical model to simulate tissue differentiation and bone regeneration: application to fracture healing. *Med Biol Eng Comput* 40:14-21.
45. Woo, S.L., Lothringer, K.S., Akeson, W.H., Coutts, R.D., Woo, Y.K., Simon, B.R., and Gomez, M.A. 1984. Less rigid internal fixation plates: historical perspectives and new concepts. *J Orthop Res* 1:431-449.
46. Guldberg, R.E., Oest, M., Lin, A.S., Ito, H., Chao, X., Gromov, K., Goater, J.J., Koefoed, M., Schwarz, E.M., O'Keefe, R.J., et al. 2004. Functional integration of tissue-engineered bone constructs. *J Musculoskelet Neuronal Interact* 4:399-400.

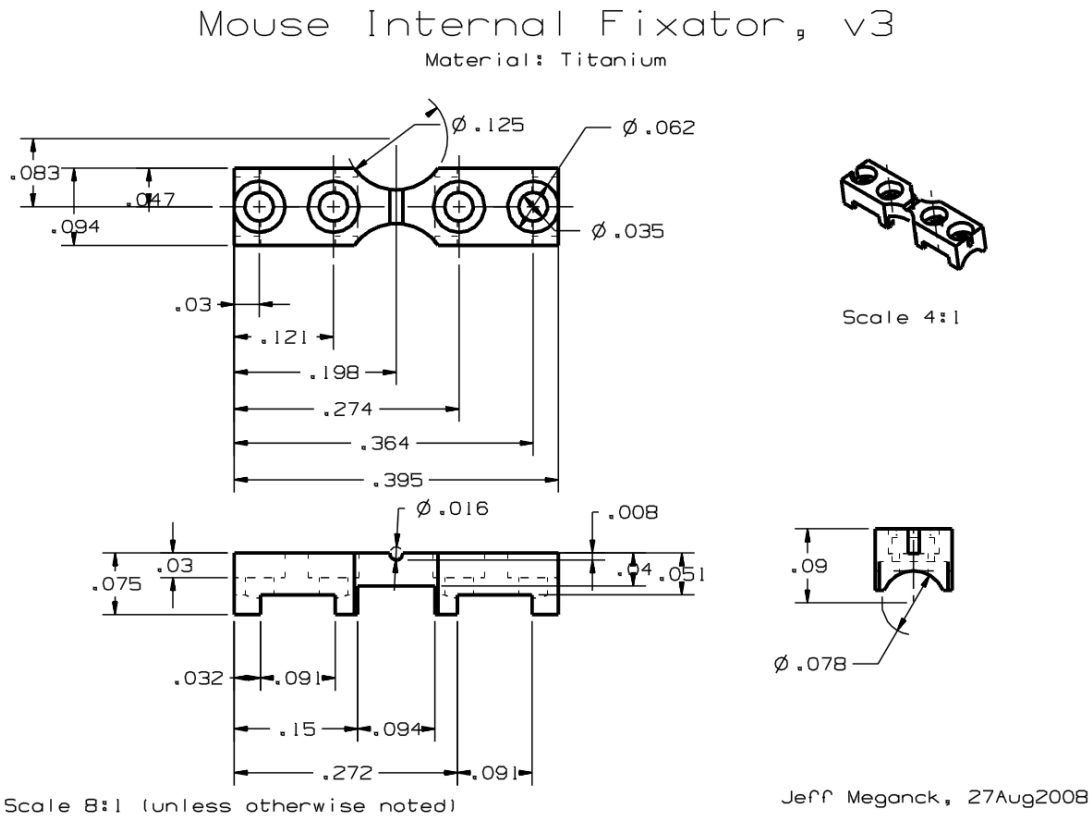

Figure 30: CAD drawing of the mouse internal fixation plate.

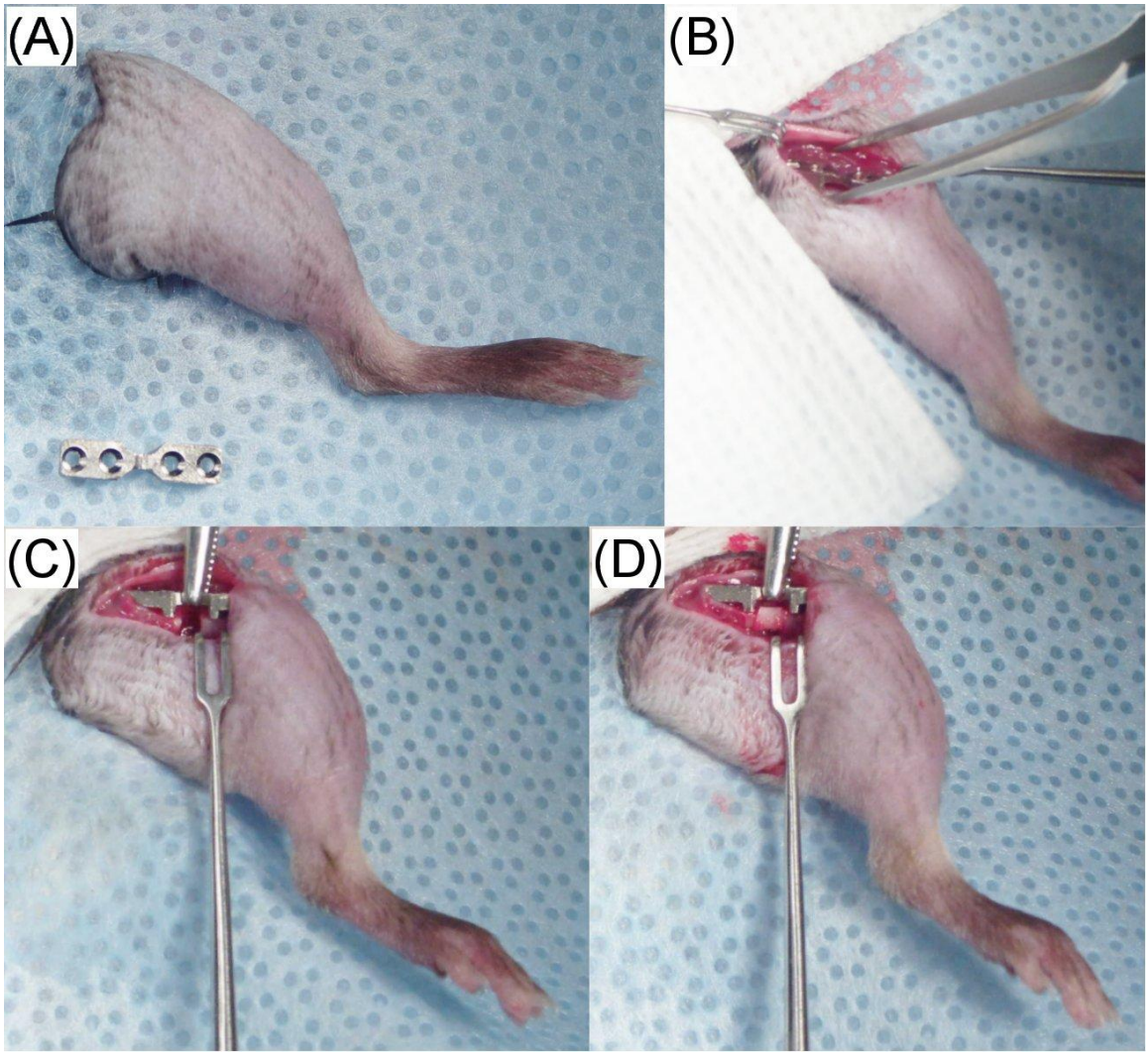

Figure 31: Images of the surgical procedure for internal plate fixation and graft insertion. In (A), the mouse leg is stabilized and the fixator is introduced into the sterile field. After an anterolateral incision, the fixator is positioned on the anterior femur (B). A defect is then created (C) and a graft is inserted (D).

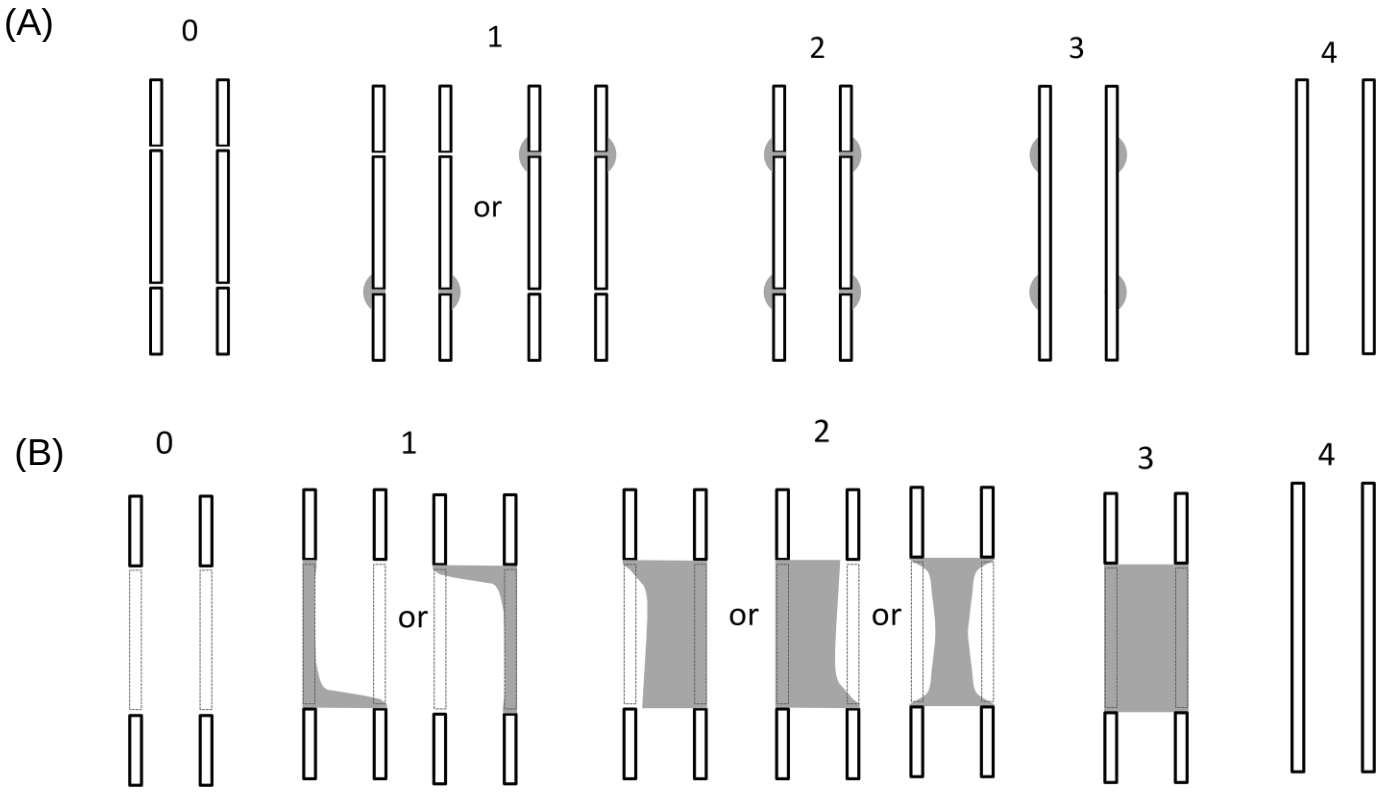

Figure 32: Schematics of the scoring system use to assess radiographic healing of (A) undemineralized and (B) demineralized grafts.

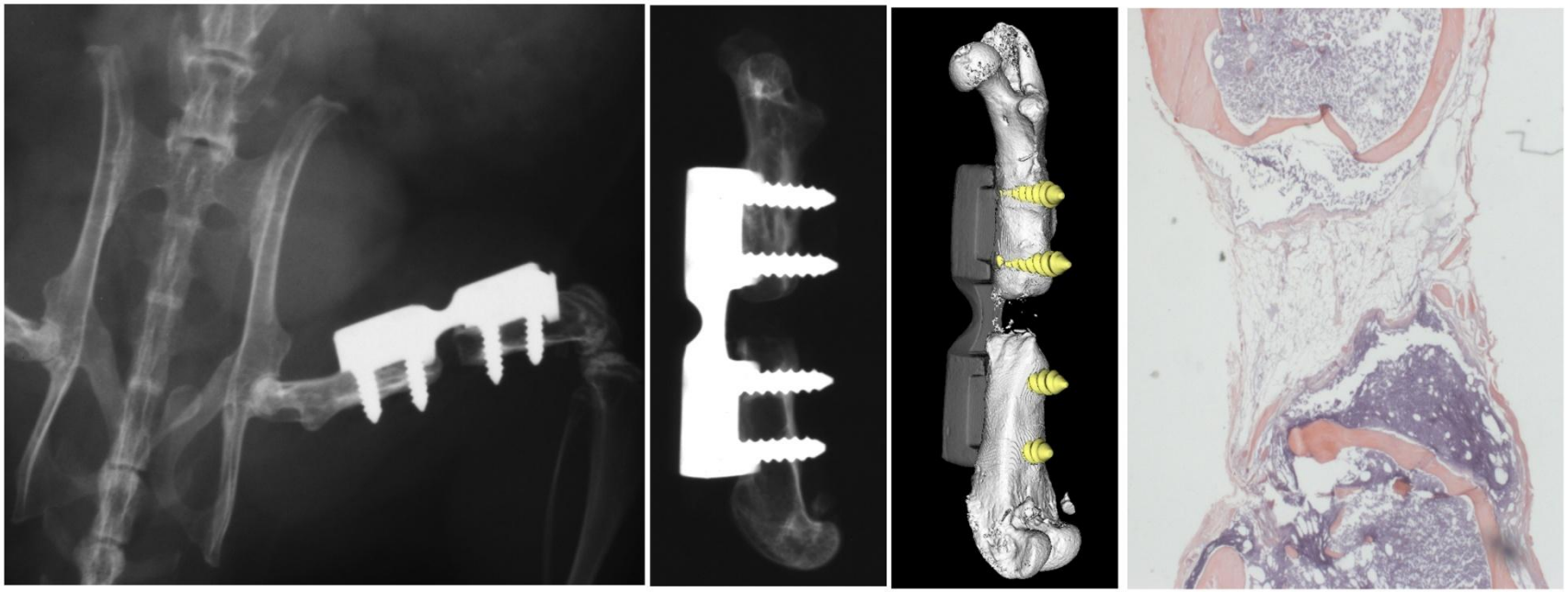

Figure 33: Panel demonstrating the non-union that occurs without a graft.

A radiographic non-union can be seen in vivo after 10 weeks (left) and more clearly after harvest (second from left). A subsequent μCT scan and 3D rendering shows similar findings (third from left) that are verified by the histological presence of fibrous tissue in an H&E stained section (right).

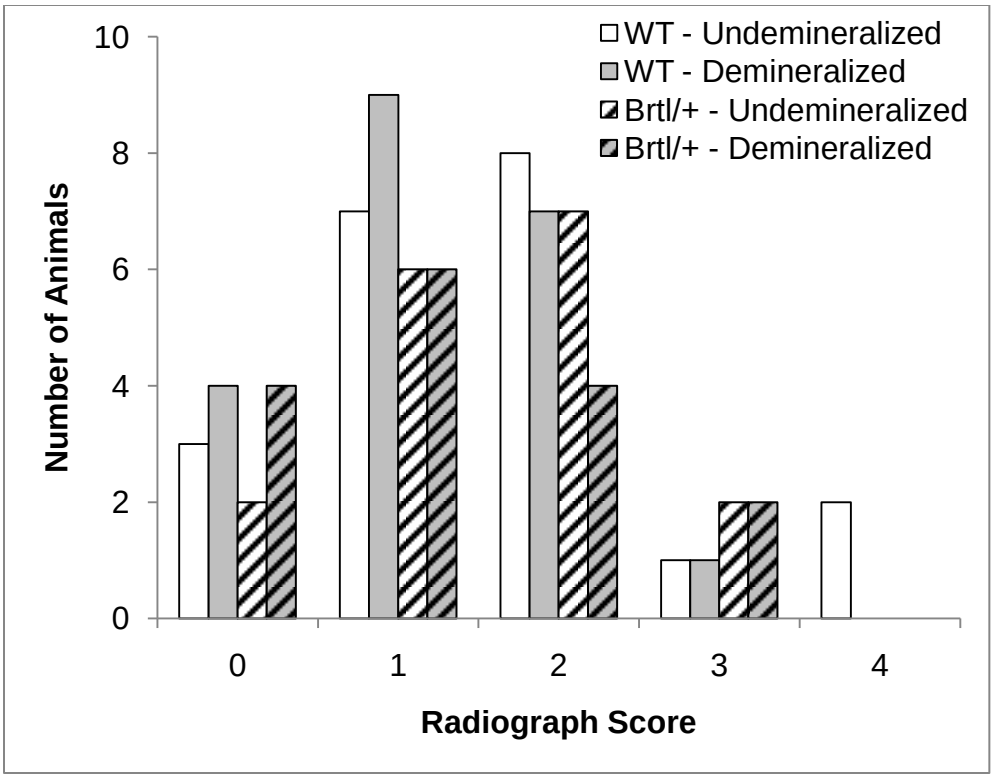

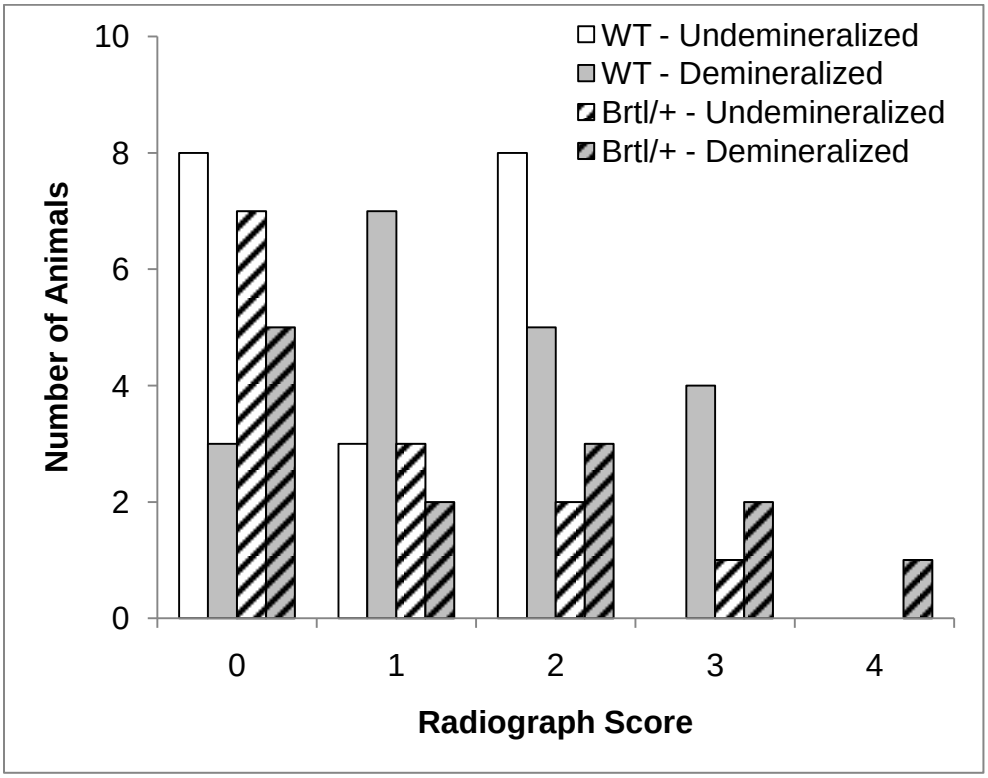

Figure 34: Histograms of the radiographic healing assessments of two separate reviewers.

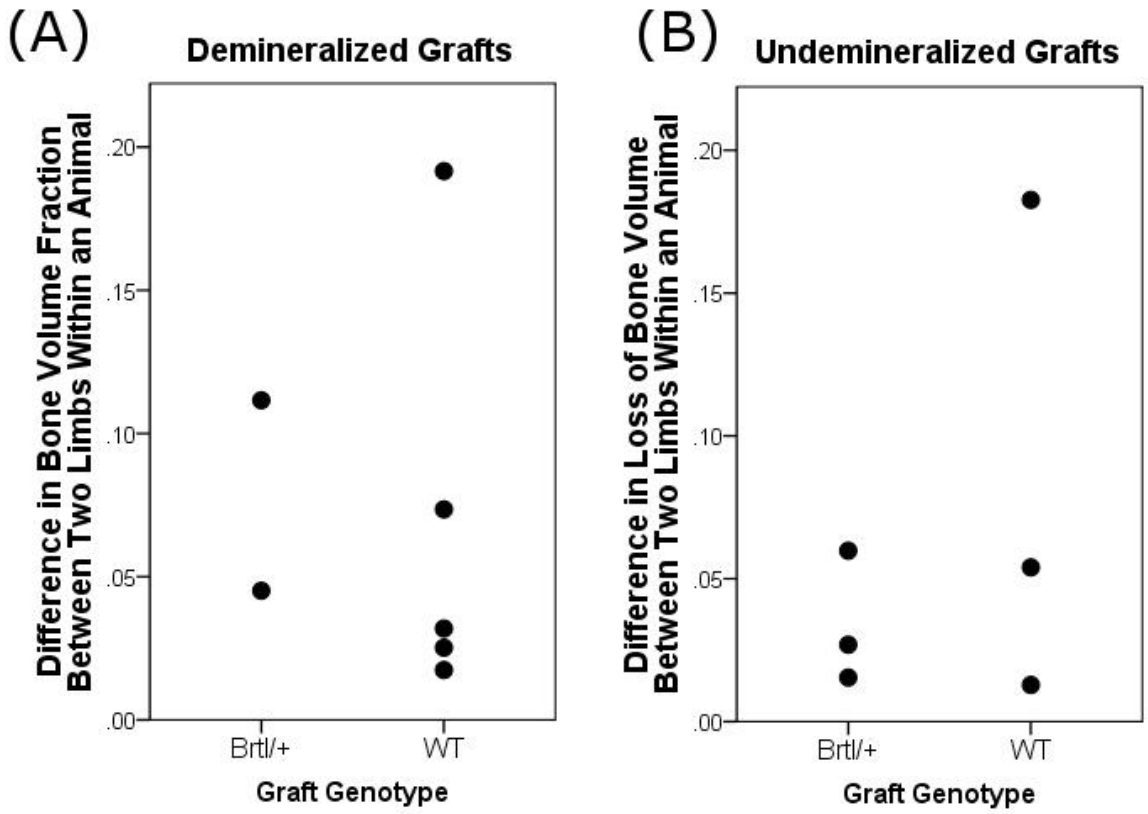

Figure 35: Comparison of μCT data for bilateral cases.

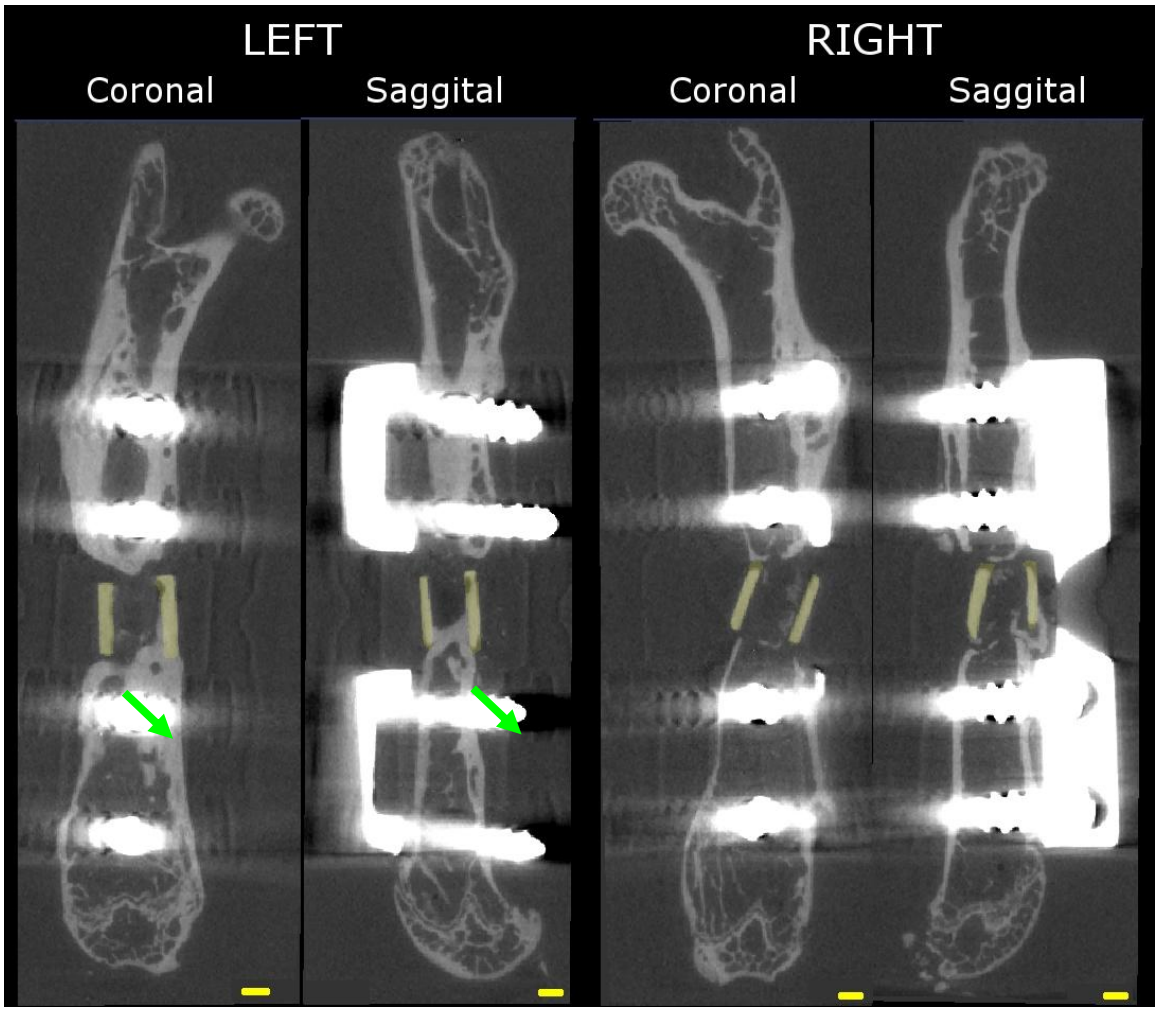

Figure 36: Sample μCT image showing the difference in healing between the two limbs of one animal which received undemineralized bilateral grafts.

Notice difference between the two limbs. There is good integration in the left leg, but very little in the right. There are also resorption pits in the left leg and some graft resorption in the right leg. Both legs received grants from the same donor.

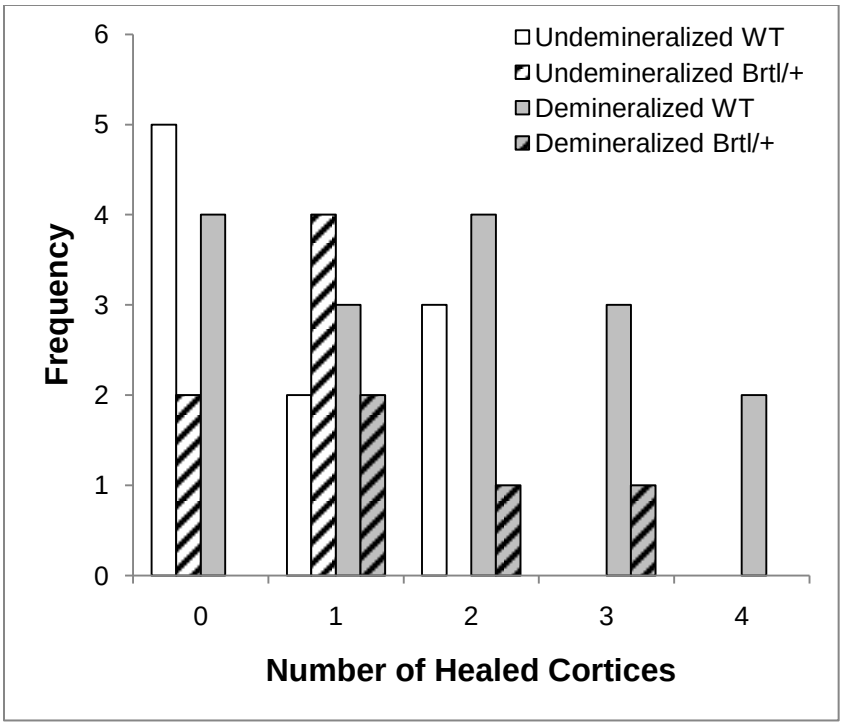

Figure 37: Histogram showing the number cortices with integration of the host and graft cortical bone based on histological assessment.

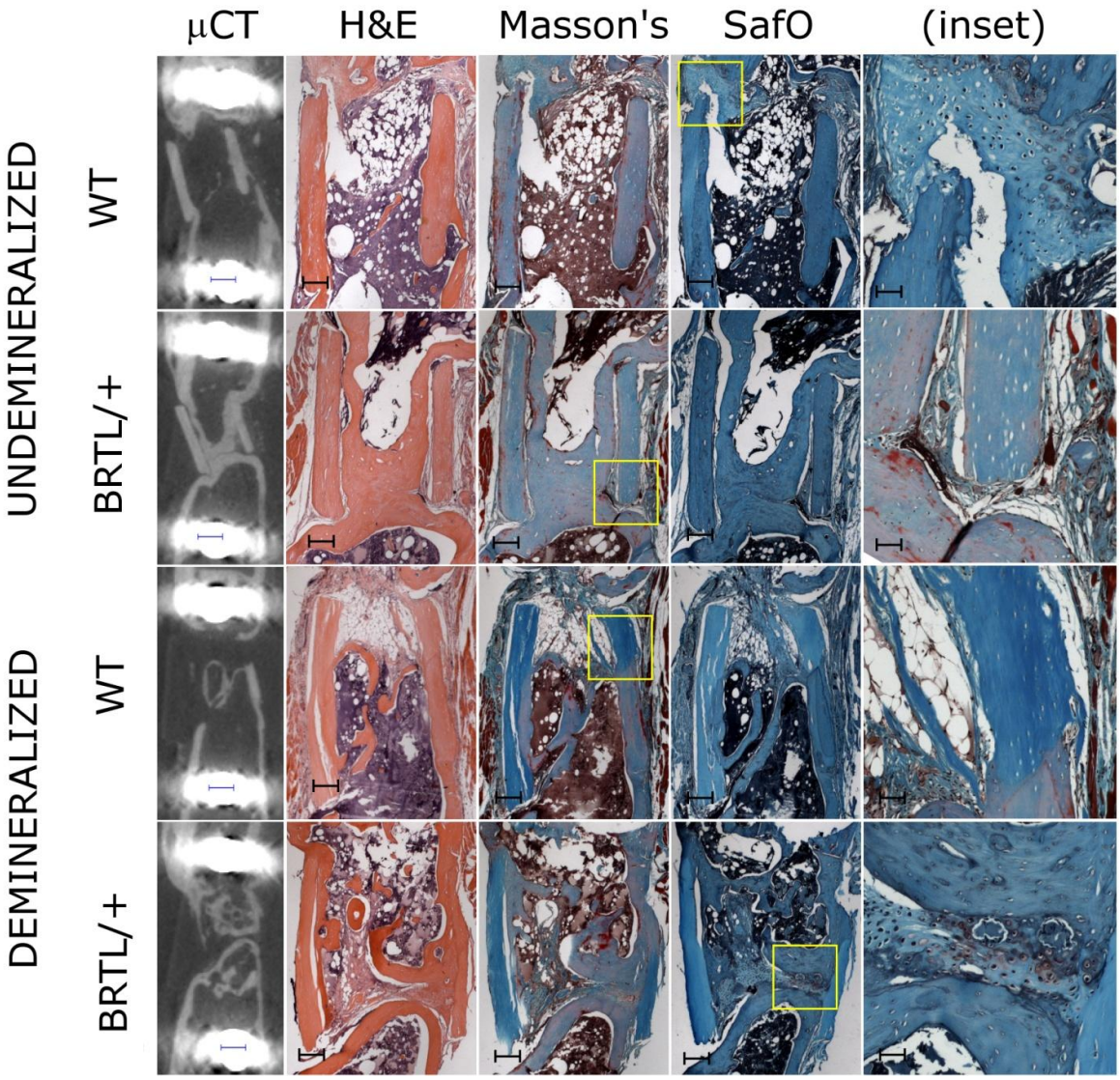

Figure 38: Panel showing the histological results in comparison with µCT slices from comparable locations.

Table 12: Description of the scoring system used to judge radiographs.

Score	Undemineralized	Demineralized
0	No Healing	No bridging
1	Host-graft union on one side (two cortices)	<50% bridged
2	Host-graft union on two sides	>50% bridged
3	No apparent host-graft boundary	Fully bridged
4	Normal cortical morphology	Normal cortical morphology

Table 13: Distribution of the number of animals utilized in this study.

Graft Genotype	Graft Type	Bilateral	Unilateral - Left	Unilateral - Right	***Total***
WT	Demineralized	5	5	6	***16***
	Undemineralized	4	7	6	***17***
Brtl/+	Demineralized	5	4	6	***15***
	Undemineralized	4	6	6	***16***
	Total	***18***	***22***	***24***	***64***

Table 14: Tissue types for nonunions at the host-graft interfaces that did not heal.

Graft Type	Graft Genotype	Fibrous	Marrow	Cartilage
Undemineralized	WT	91%	5%	3%
	Brtl/+	93%	2%	5%
Demineralized	WT	84%	16%	1%
	Brtl/+	81%	11%	7%

Table 15: Presence of revitalized tissue in Masson's trichrome stained sections.

Graft Type	Graft Genotype	Healed		Not Healed	
		Osteoid	No Osteoid	Osteoid	No Osteoid
Undemineralized	WT	100%	0%	80%	20%
	Brtl/+	91%	9%	86%	14%
Demineralized	WT	82%	18%	20%	80%
	Brtl/+	80%	20%	0%	100%

Chapter 5: Conclusion

This work brought together results from three disparate, yet related studies supporting or advancing knowledge of approaches to bone repair and regeneration. The first goal was to evaluate methods to improve the ability of commercially available μCT systems for accurate bone densitometry as it might relate to quantifying bone repair and regeneration. The first hypothesis, that filtration can be used in a μCT system to avoid beam hardening artifacts and the resulting images can be used for accurate densitometry, is strongly supported. This is important for understanding bone structure-function relationships and bone healing. This experiment was predominantly related to instrumentation and was relatively straightforward. The studies utilizing *in vivo* models, on the other hand, were significantly more complicated.

The second study presented in this dissertation, relating to fracture healing with alendronate treatment in the Brtl/+ mouse model of OI, represents a sizeable effort to address the broad hypotheses that inhibiting resorption using alendronate, as well as the matrix alterations inherent in the Brtl/+ mouse, would impact the healing process. In one sense, the data in this dissertation support

these ideas. There were many other studies already in the literature investigating bisphosphonates in fracture healing, so it is not a surprise that alendronate injections result in larger calluses with more bone and structural biomechanical changes. Given this strong effect, it was surprising that the fracture healing process was barely altered in the mice which only received alendronate before the bone was fractured. With the exception of a few minor subtleties, the healing process in these mice was essentially normal. This may imply that the level of bisphosphonate in this callus was quite low. Future studies may address this directly using labeled bisphosphonates that can be spatially tracked. It may also be interesting to see if the same phenomena were present in metaphyseal fractures, since there is more surface available for bisphosphonate binding in trabecular compartments.

Experiments like this, however, wouldn't necessarily be able to directly address questions about matrix organization and their impact on remodeling. Using the polarized light analysis presented in chapter 3, the data indicated a trend toward disorganization. This is surprising given the low inherent power in that analysis and should likely be confirmed in the future by performing a similar analysis on sections of normal bones, using polarization in Raman microspectroscopy, looking directly at collagen fibrils with atomic force microscopy, or some other technique that has not yet been developed.

Regardless of this, there is still information to learn about the hypothesis that matrix organization impacts biomechanical function. The initial idea was that collagen in both the intact tibias and in the fracture callus would be disorganized

due to a fundamental mechanism related to the disease. This only seems partially true. Collagen in the fracture callus is definitely disorganized, but this seems to be related to the nature of bone formation during fracture healing instead of a fundamental phenotypic alteration. It appears like the fracture callus in the Brtl/+ mice essentially has normal biomechanical properties during healing. Future experiments which look later in healing would be intriguing to understand when this transitions back to the biomechanical deficiencies inherent in OI bone.

These inherent deficiencies led to the third major study presented in this dissertation. The matrix alterations in a graft scenario are critical to understand because they provide the initial conditions for the subsequent healing process. This study required development of a new model. In the end, even though a sizeable number of animals were used in the experiments, sources of variability in the model may have masked the ability to test the hypothesis that an alteration in the initial conditions impacts remodeling and biomechanical function. There are hints of remodeling from the μCT images, but very few of the grafts which appeared to be radiographically healed had any meaningful biomechanical function. This may actually imply that subtleties in the graft material are far less important than therapies which improve the healing process. On the other hand, it may imply that the model isn't ideal for these questions. Models which implant altered ECMs ectopically, use them in *in vitro* culture systems which allow cleaner experiments due to their more reductionist nature, or implant them into stable gaps (such as a drill hole defect), or some other system may be needed to address these questions in the future. Perhaps, however, future developments

and/or improvements to the fixator itself, experimental techniques, or biologically based therapies to help jump start healing may still make experiments like this feasible. Other experiments using an intramedullary pin to stabilize bone transplants from a transgenic mouse into a normal mouse have already been reported and were insightful, so future developments may be interesting to pursue. On the other hand, it is vital to purse these developments in a translationally relevant, inexpensive, challenging healing model like the mouse fixator developed in these experiments.

In conclusion, the three studies in this dissertation embody an effort to study bone healing and regeneration in a translationally relevant fashion. Accurate use of non-destructive imaging tools, as demonstrated in the first experiment, is essential for this type of work. Once these tools are understood, they can be applied using preclinical models of bone fracture healing and graft healing. When these healing models are used in conjunction with transgenic animals, healing and treatment approaches can be studied in musculoskeletal diseases. The temporal dynamics of healing depend on the injury and treatment approach, and applying these imaging tools in conjunction with unique animal models can also be insightful. The application of the tools and model systems, however, is not the full story. Translational impact comes from investigating basic science questions. Within this dissertation, surprisingly, fundamental collagen alterations may not have any direct negative implication in early to mid stage fracture healing nor on graft healing. This type of insight that can potentially impact future clinical treatment approaches.